PROCESSING AND ANALYSIS OF ULTRASOUND IMAGES FOR TISSUE CHARACTERIZATION

A thesis

submitted in fulfillment of the requirement of

Doctorate of Philosophy

Submitted by

MANDEEP SINGH
Roll No. 90704501

ELECTRICAL & INSTRUMENTATION ENGINEERING DEPARTMENT

THAPAR UNIVERSITY, PATIALA

PUNJAB – 147004, INDIA

2014

ਆਪੇ ਪਟੀ ਕਲਮ ਆਪਿ ਉਪਰਿ ਲੇਖੁ ਭਿ ਤੂੰ ॥
ਏਕੋ ਕਹੀਐ ਨਾਨਕਾ ਦੂਜਾ ਕਾਹੇ ਕੂ ॥੨॥

ਮਲਾਰ ਕੀ ਵਾਰ: (ਮਹਲਾ ੧) ਅੰਗ ੧੨੯੧

You Yourself are the writing tablet, and You Yourself are the pen. You are also what is written on it.

Speak of the One Lord, O Nanak; how could there be any other? ||2||

Raag Malaar (Guru Nanak Dev JI)

Dedicated to my family,

who missed many happy moments
due to this research work.

THAPAR UNIVERSITY, PATIALA

CANDIDATE'S DECLARATION

I hereby certify that the work which is being presented in the thesis entitled "**PROCESSING AND ANALYSIS OF ULTRASOUND IMAGES FOR TISSUE CHARACTERIZATION**" in partial fulfillment of the requirement for the award of the Degree of Doctor of Philosophy (Ph. D.) and submitted in the Department of Electrical & Instrumentation Engineering of Thapar University, Patiala is an authentic record of my own work carried out under the supervision of **Dr. Sukhwinder Singh**, Professor, UIET, Panjab University Chandigarh and **Dr. Savita Gupta**, Professor, UIET, Panjab University Chandigarh.

The matter presented in this thesis has not been submitted by me for the award of any other degree of this or any other Institute/University.

(MANDEEP SINGH)

This is to certify that the above statement made by the candidate is correct to the best of our knowledge.

Date: 22nd APRIL 2014

22/4/14.
(Dr. Sukhwinder Singh)

(Dr. Savita Gupta)

S. Ghosh
(Dr. S. Ghosh)
Head EIED

(Dr. P.K. Bajpai)
Dean R&SP

Signature of Examiner

CONTENTS

List of Figures

List of Tables

List of Abbreviations used

ASM	Angular Second Moment
CAD	Computer Aided Diagnosis
CNT	Contrast
CNTG	Contrast from GLDS texture model
CNTS	Contrast from SFM texture model
CoC	Correlation Coefficient
COV	Coefficient of Variance
CRC	Correlation coefficient
CRSS	Coarseness
DENT	Difference of Entropy
DFT	The Discrete Fourier Transform
DVAR	Difference of Variance
DWT	Discrete Wavelet Transform
ENGG	Energy from GLDS texture model
ENL	Equivalent Number of Looks
ENT	Entropy
ENTG	Entropy from GLDS texture model
EPI	Edge Preserving Index+D25
Eq.	Equation
FF	Fractal Feature
FOS	First Order Statistics
fpde	Fourth order Partial Differential Equation based filter
FPS	Fourier Power Spectrum
GLDS	Grey Level Difference Statistics
GLRM	Grey Level Run-length Matrices
H1	Hurst coefficient at resolution k=1
H2	Hurst coefficient at resolution k=2
HOMG	Homogeniety
IDM	Inverse Difference Moment
IMC1	Information Measure of Correlation 1
IMC2	Information Measure of Correlation 2
KRTF	Kurtosis from FOS texture model
LDA	Linear Discriminant Analysis
MENF	Mean from FOS texture model
MOS	Mean Opinion Score
PCA	Principal Component Analysis
PER	Periodicity
pm22	Perona-Malik anisotropic diffusion based filter
RF	Radio Frequency
RGH	Roughness
ROI	Region of Interest
S_MSE	Signal to Mean Square Error ratio
SAR	Synthetic Aperture Radar
SAVG	Sum of average
SENT	Sum of Entropy
SFM	Statistical Feature Matrix
SGLCM	Spatial Grey Level Co-occurrence Matrix

SKWF	Skewness
SNR	Signal – to – Noise ratio
SRAD	Speckle Reduction Anisotropic Diffusion
SSI	Structure Similarity Index
SVAR	Sum of Variance
SVM	Support Vector Machine
TEM	Law's Texture Energy Measure
TGC	Time Gain Compensation
UTC	Ultrasound Tissue Characterization
VAR	Variance

ACKNOWLEDGMENTS

First praise to GOD, for being kind enough to provide me the patience, knowledge and 'will' to complete this research work. During this period, I have gone through many successes and failures, but recovering from the failure and taking it as a lesson was due to the Almighty.

I devote this space to acknowledge all those, who have made this degree a reality, however, these few words cannot convey the proper gratitude to all my dear ones.

My foremost thanks go to my worthy supervisor Dr. Sukhwinder Singh, Professor, University Institute of Engineering and Technology, Chandigarh for all his guidance, motivation and direction during my Ph.D. I am very grateful to him for carefully correcting countless typos in my dissertation. As a chairman of many committees, he is probably the busiest man, yet I have always felt his support in good or bad times. I admire him, for the challenges, he has made me to face, and for the guidance, which gave me the courage to lead every race. He has always been present to support and encourage me in my professional life when times were tough. The regular discussions with them has helped me to understand not only independent research but also polished my professional career.

I also appreciate the support and affection from Sir's family members during the discussions at his home. The never ending hospitality by Sir's wife is unforgettable.

I am equally grateful to my second supervisor Dr. Savita Gupta, Professor, University Institute of Engineering and Technology, Chandigarh for her guidance and support. She brings her keen insight to bear on the many problems, I presented before her. She has really contributed a lot during my research work and revising my thesis. It is pleasure to thank her for her guidance, instruction, advice. Her constant support and advice in the theoretical aspects of research make possible for me to bring this dissertation within reach. It has been both a privilege and a pleasure to have been associated with both of my supervisors.

I offer special thanks to Prof. Smarajit Ghosh, Head, Electrical and Instrumentation Engineering Department, Thapar University, Patiala, for providing all the necessary facilities in the department. He was always there to support me even in my difficult times and encourages me to do my work. I wish to express thankfulness to all the faculty and staff of the Electrical and Instrumentation Engineering Department for their kind support. I am thankful to Prof. P. Gopalan Director, and Prof. K.K. Raina, Deputy Director Thapar University, Patiala, for their encouragement and constant moral support to accomplish this task.

I acknowledge the useful suggestions given by the members of my doctoral committee Dr. Mandeep Singh and Dr. Kulvir Singh. Thanks to Dr. P. K. Bajpai, Dean, research and sponsored projects for providing the possible research facilities here at Thapar University campus. Special thanks to Dr. Maneek Kumar for providing me useful and valuable tips during my research and Dr. Mandeep Singh for providing many important comments and inputs to the thesis. He really supported me like a mentor and a friend.

Of course, none of this could have happened without the blessings of my parents S. Hakam Singh and Mrs. Charanjit Kaur and my brother Harpreet Singh who have been my backbone during this period. Special thanks are due to my in-laws S. Balwinder Singh and Mrs. Paramjit Kaur, my brother in-law Er. Tejinder Singh for their unconditional love and support. The smiling faces and tantrums of kids Simar, Kunwar, Gurnoor and Ekjot have always made me refreshing.

I often feel guilty for depriving my sons Jap Kunwar Singh and Simar Rajan Singh, the joy and pleasure moments of their life, which they would have enjoyed with me, but had to sacrifice during my Ph.D. time.

Many thanks to my fellow colleagues, and Dr. Maninder Singh, Dr. Deepak Garg, Dr. S.K. Singla, Dr. Ajay at Thapar University for sharing their experiences and also for spending their valuable time in constructive discussions.

I extend special thanks to Mr. Vipul Sharma my fellow researcher at UIET Chandigarh, who have always been helpful and insightful while working in the lab. He and Tejinder Singh were the major resource of all my logistics at Chandigarh. My heartiest thanks are also extended to my other fellow researchers, Dr. Jagroop Singh and Jaskirat Singh at UIET Chandigarh who always helped me to be cheerful and delighted.

Last but not the least, I thank to my wife **Dr. Varinderjit Kaur,** who support me unconditionally during the Ph.D. work. She was always my third and fourth hand while editing work. I have no words for the great support and the deep understanding with which my wife Dr. Varinderjit Kaur looked after our family at home and stood firmly with me at every moment when I wish her to be and kept me free from all the responsibilities of home, during my work. Her welcome smile is always a source of inspiration for me.

(Mandeep Singh)

ABSTRACT

Medical imaging is a non-invasive process of visualizing the inner body tissues, organs and bones for diagnosis purpose. It is the fast growing branch of biomedical engineering. These days many imaging modalities are available for different applications. Ultrasound imaging is the most popular because it is non-ionizing, low cost, portable and real time imaging. The main applications of ultrasound imaging are visualizing the fetus development, diagnosis of prostrate and abdominal organs like kidneys, gallbladder and liver. Liver is one of the most important organs in the human body, because it controls many important metabolisms. Fatty liver disease (*steatosis)* is highly prevailing disease among all the liver diseases in India. The visual examination of ultrasound images, for diagnosis of fatty liver is subjective and less accurate in marginal cases. Fatty liver is a condition that occurs when the fat content of the '*hepatocytes*' increases, resulting in variation of the texture of liver surface. Therefore, quantitative texture analysis may give crucial information which is otherwise difficult to extract by visual interpretation of ultrasound images. In this research work, a Computer Aided Diagnostic (CAD) method is proposed for the liver tissue characterization using texture analysis.

The ultrasound imaging has one limitation, and that is *speckle*, which degrades the visual quality of ultrasound images and masks some fine details of tissue under observation. Therefore it is important to suppress this speckle before any computer aided image processing or analysis, while keeping the diagnostic information intact. To accomplish this task, a modified fourth order partial differential equation (*fpde*) based filter is proposed, which is adaptive to local 'coefficient of variance' in the 3x3 spatial window. To further increase the efficacy of the filter,

‘edge-map’ technique is used, which enhances the edges and fine details in the ultrasound image. The performance of this proposed image enhancement method is evaluated on synthetic and ultrasound images through visual analysis by the expert radiologists as well as through quantitative metrics. It has been found that proposed ultrasound image enhancement method outperformed other existing methods.

Liver is very large tissue and to extract the features for quantitative analysis, a Region of Interest (ROI) is selected. The ROI is a sub part of the image and is used to avoid unwanted blood vessels, bile duct, and cyst in the analysis, Moreover, the use of ROI will reduce the computational time. Thus, the selection of an appropriate ROI is very crucial in CAD systems. In this work, experiments were conducted to find the appropriate ‘shape, size and location’ of ROI. After the analytical study and discussions with radiologists, it has been observed that a square shaped ROI having size of 30x30 pixels size is optimal, and it should be taken along (or near) the centre line of the image. To increase the reliability of CAD, multiple ROIs are selected from a single image and subsequently, the average value of each feature from multiple ROIs is computed and used for further analysis.

A lot of research has been done for liver characterization through ultrasound imaging. Although there are number of quantitative techniques for liver characterization such as radio frequency (RF) signal back-scattered and attenuation analysis, elastography etc., but texture analysis is the most reliable technique. Many texture models like Spatial Grey Level Co-occurrence Matrix (SGLCM), Grey Level Difference Statistics (GLDS), First Order Statistics (FOS), Law’s Texture Energy Measure (TEM), Fourier Power Spectrum (FPS), Statistical Feature Matrix (SFM), Fractal Feature (FF), Grey Level Run Length Matrices (GLRM) have been used for Ultrasound Tissue Characterization (UTC). These texture models are used with different classification methods and, each method has its own advantages and disadvantages. The more accurate methods are computationally expensive, while the easier to compute methods are not so accurate. Thus, keeping in view of the above discussion, there is a need to go for a computer aided, quantitative, improved method that give fairly high accuracy with lesser computational load. In this research work, an *information fusion* based method is proposed to help the radiologists in characterizing the fatty liver more accurately and fast. This novel method uses highly discriminating texture features in a linear combination to give a discriminative index (D_I) to differentiate the fatty liver and normal liver. The highest discriminative feature has the highest weightage to find D_I. The threshold value of D_I is selected in such a way that it gives 100% sensitivity, which means, that none of the fatty liver is miss-classified as normal liver. The overall accuracy of the proposed method is 95% with 100% sensitivity, which is better than other existing methods.

Another limitation of most of the existing quantitative methods is that they are able to characterize the liver into normal liver or fatty liver only. However, for a physician it is more important to know the level of fat accumulation in the liver (fatty liver grading), to suggest a better treatment. Fatty liver is further characterized as mild fatty, moderate fatty and severe fatty, depending upon the fat deposition in the *hepatocytes*. Moreover, highly discriminative texture features are very sensitive to the grey level in the image. While acquiring the ultrasound image, usually the radiologist varies the Time Gain Compensation (TGC) settings for better visual analysis. This variation in machine settings causes change in average gray level among different ultrasound images. Therefore the classification methods which are using 'grey level' based texture features, are prone to errors. To overcome this drawback, the grey level based features are used after taking the ratio of their values from liver and kidney. A limited number of researchers like Webb *et al*., Soder et al., Minhas et al. have used the ratio of grey-level based features for liver tissue characterization, and termed it as hepato-renal index or ratio. They have used ratio of only two of grey-level based features (mean grey level intensity and contrast). These researchers have not considered any frequency or fractal based feature. However in the present study, five highly discriminative grey level based features are used after taking their hepato-renal ratio. Moreover, frequency and wavelet based features are also combined and a feature vector is formed of highly discriminative features. Finally a multiclass Support Vector Machine (SVM) based classification method is presented to characterize the normal and fatty liver and then, the further grading of fatty liver into mild, moderate and severe fatty liver. In the proposed method polynomial kernel of SVM is selected in such a way that it gives 100% sensitivity, which means, that none of the fatty liver is miss-classified as normal liver. The overall classification accuracy of the proposed method is 98.3% with 100% sensitivity.

The present work is likely to contribute significantly in the area of computer aided medical image analysis and diagnosis. An experimental study has also been done to find optimal size of ROI for liver tissue characterization. A novel classification method, based on information fusion is proposed in this thesis, which gives a discriminative index D_I to classify the normal and fatty liver. However the concept is universal and applicable to any other binary classification problem. The SVM based fatty liver characterization method can be useful in timely diagnosis of mortal liver disease.

Finally, some suggestions based on observations and experiments, are presented to carry out further research work in this area.

CHAPTER-1

INTRODUCTION

1.1 OVERVIEW

Biomedical imaging is a technique to generate a visual representation of physiological structures visible or hidden inside the body. These images are further evaluated by the physician or radiologist for the diagnosis. These days, many imaging modalities such as Single Photon Emission Computed Tomography (SPECT), Electrical Impedance Tomography (EIT) and functional Magnetic Resonance Imaging (fMRI) are being used; however ultrasound imaging is still widely used because it is non-invasive, economical and portable. Some of the common applications of ultrasound imaging are monitoring the growth of fetus, to diagnose problems in abdomen, and to analyze the diseases in tissues like kidney and liver. In the case of liver, ultrasound imaging is mainly used for the diagnosis of fatty liver (*Steatosis*). The prevalence of fatty liver amongst adults in India is 24% [1]. *Steatosis* is a condition, that occurs when the fat content of the '*hepatocytes*' increases to more than 5% of the weight of the '*hepatocytes*'. This metabolism results in the change of the texture of liver surface. The visual analysis of this variation in texture of liver surface is generally subjective as it depends on the capability of the radiologist to examine the variation in gray level and in textural characteristics of the liver tissue in an image. Therefore, quantitative texture analysis of liver images may give crucial information which is otherwise difficult to extract by visual examination of ultrasound images. Further, the diagnostic accuracy through visual interpretation is approximately 72% in marginal cases due to speckle noise [2]. Speckle is a form of locally correlated multiplicative noise with granular appearance. Speckle tends to mask small details, reduce image contrast and detail resolution. Therefore, in ultrasound images, speckle reduction is a useful pre-processing step for automatic segmentation, feature extraction and image analysis. Goal of the proposed research work is two-fold; firstly, a speckle reduction method is proposed to enhance the quality of ultrasound images and secondly, a computer-aided method is proposed for liver tissue characterization using texture analysis.

1.2 LITERATURE REVIEW

A comprehensive study of available literature is carried out, to review the research work already done in the related area. Various speckle suppression filters have been studied to identify the best image-enhancement method for ultrasound images. Different texture domain models have also been studied and analyzed to find the optimal set of features for tissue characterization. To utilize the optimal features for liver tissue characterization, an analysis of existing liver classification methods is carried out.

1.2.1 Image Enhancement

The research on speckle reduction from ultrasound images is broadly classified into four categories. The first one is based on local statistics in a window, second category is based on homogeneity of pixels' intensity, third is partial differential equation or an-isotropic diffusion based filters, and the fourth is wavelet based or other multi-resolution based filters. The early methods of speckle suppression from ultrasound images were implemented by averaging the uncorrelated images of the same tissue acquired under different spatial positions [3, 4]. Although these methods are effective for speckle suppression, but they need multiple images of the same object to be obtained [5]. A Partial Differential Equation (PDE) based '*anisotropic diffusion*' filter is used to remove noise from ultrasound images [6, 7]. Yu and Acton proposed Speckle Reduction Anisotropic Diffusion (SRAD) in which diffusion constant is replaced with “instantaneous coefficient of variation” as a function of local gradient magnitude and Laplacian of image [8]. However in this method, a reference homogenous area has to be selected manually and this makes this technique a non-persistent and highly user dependent. You and Kaveh proposed a class of fourth-order partial differential equations (*fpde*) to remove the speckle noise [9]. This technique can suppress the speckle, but it is not able to preserve edges and some fine details in the image. Recently, a modified version of SRAD is also proposed by Mittal *et al.* which further enhances the visual quality of ultrasound images [10]. Many researchers have carried out a significant image enhancement work using wavelet transform to refine the ultrasound images [11, 12]. Gupta *et al*. proposed a new speckle reduction filter called ‘*Homo-Genthresh’*, which is adaptive and versatile [13, 14]. The method utilizes *Homomorphic* wavelet thresholding technique by modeling speckle as Generalized Nakagami distribution rather than Gaussian one. Dantas and Costa proposed a collection of wide-band 2D directive filters based on modified Gabor function, in which, each filter works in a specific direction to refine the image with reduced speckle while preserving the resolution [15].

Most of the above said filters perform well in homogenous areas but they lack near the edges either by leaving the speckle near the edges or they blur the edges while filtering. In this way, speckle suppression is not directional but parallel to the edges. These issues are considered as a motivation for the proposed image enhancement work. Therefore, spatial domain filters have been studied and analyzed to propose a new method for speckle suppression while preserving fine details and edges in ultrasound images.

1.2.2 Texture Analysis and Tissue Characterization

Wagner *et al.* have established that the transducer characteristics are primarily accountable for the speckle in ultrasound images [16]. Therefore, it is better to use texture analysis methods that can significantly reduce this dependence. In the recent years, the classification of the liver (normal and abnormal) tissue in an ultrasonic image has been done by extracting many features. However, the Fourier Power Spectrum (FPS) proposed by Lendaris [17], the Spatial Gray-Level Co-occurrence Matrices (SGLCM) by Haralick [18], and the Texture Energy Measures (TEM) suggested by Laws [19] are the most commonly used texture models that have been applied successfully to liver ultrasound images. Thijssen also reported that texture based analysis is very useful in ultrasound tissue characterization [20]. Lu and Shen proposed a novel method called texture similarity map for the analysis of ultrasound images describing texture by spectral measures based on Fourier spectrum [21].

The Statistical Feature Matrix (SFM) texture model has also been used to describe surface textures [22]. Grey Level Difference Statistics (GLDS) as proposed by Weszka and Dyer for terrain classification in SAR images is useful for texture analysis [23]. Wu *et al.* proposed a new concept based on the multi-resolution fractal dimensions also called Fractal Features (FF) for liver characterization [24]. Different classification methods were explored by Kadah *et al.* to characterize diffuse liver diseases [25]. Badavi *et al.* described a fuzzy logic based liver classification method using texture analysis [26]. Lee *et al.* used Artificial Neural Network (ANN) technique on fractal geometry for liver classification [27]. Fractal analysis was explored with the *'k-mean'* clustering for liver classification by Balasubramanian [28]. A Support Vector Machine (SVM) based classification method for fatty liver and normal liver was proposed by Li *et al.* [29]. Riberio and Sanches reported a Bayesian classifier for the same [30]. A *'heptorenel index'* was proposed by Webb *et al.*, to classify the normal and fatty liver [31]. This method utilizes the ratio of mean grey level of liver and kidney. Recently, Acharya *et al.* proposed a framework for liver classification using data-mining technique [32]. Another recent technique, the '*grey relational analysis*' has been proposed to grade the fatty liver, which is better than many previous techniques [33].

Although a lot of work has been done in the area of liver tissue characterization, but still it is the subject of great importance and relevance due to increasing prevalence of fatty liver across the globe. Therefore, a computer aided quantitative method with better accuracy is still need of the hour in biomedical imaging to assist the radiologists for better diagnosis.

1.3 PROBLEM FORMULATION

Ultrasound images have a specific granular pattern called speckle. The speckle diminishes the visual quality of the ultrasound images and, the fine detail of a tissue is not visible. Further, it reduces the efficiency of image processing operations like automatic segmentation and image analysis. Therefore, the first objective of the proposed work is to enhance the image quality, so that subsequent image processing and analysis is reliable and effective.

Most of the existing classification methods are computationally complex and none of the researchers have analyzed the features collectively to choose the most discriminative features. Therefore, in this proposed work, a novel classification method is presented using fusion of the optimal features from different domains like: *structural, statistical, frequency* and *fractal* texture models. The optimal features are selected on the basis of their ability to differentiate liver images into normal and fatty. Subsequently, the best features have been combined in such a way that a single quantitative metric is obtained to classify the liver.

Most of the available studies on liver tissue characterization are based on texture analysis, which highly depend upon the control settings of ultrasound machine. Radiologists usually vary the time gain compensation, ultrasound frequency of probe and amplifier gain to get better display and information from the area of interest. These settings and changes are very subjective in nature, which makes ultrasound tissue characterization, observer and machine dependent [34]. To address this issue a novel method for liver characterization is proposed, which is independent of grey level of image and hence independent of ultrasound machine settings. The proposed method is able to characterize the liver tissue into normal, mild fatty, moderate fatty and severe fatty. Finally, the proposed method has been validated on real dataset of liver ultrasound images in references to other existing methods. In brief, the objectives of the research work are listed below.

1. Identification of an improved image enhancement method for tissue characterization in ultrasound images.
2. Feature extraction from Region of Interest.
3. Selection of features for specific tissue characterization.
4. Validation of the method developed.

1.4 PROPOSED METHODOLOGY

To accomplish the aforesaid research objectives, a brief description of the methodology is presented below:

1.4.1 Image Acquisition

For liver characterization, no standard database is available and therefore a specific database has been created for this research work. A collaboration for this purpose has been done with Post Graduate Institute of Medical Education & Research (PGIMER) Chandigarh and Delta

Diagnostic Centre, Patiala. The present study is conducted on 240 ultrasound liver images (one image per patient). All the patients were within the age group of 25 – 60 years and consisting of 148 men and 92 women. The consent of the patients has been taken for the study and all the guidelines have been followed as per the approved procedure of University ethical committee.

1.4.2 Image Enhancement

Most of the spatial domain speckle suppression filters are unable to enhance the diffused edges in ultrasound images, because these filters inhibit smoothing near the edges in order to preserve the image details. This limits the use of standard spatial domain filters for medical ultrasound images, where thin diffuse edges are present. The performance of standard spatial domain filters has been improved by devising a modified speckle suppression technique. The proposed method utilizes the local statistics in a moving window, based on weighted-mean and standard deviation. The coefficient of variance is also incorporated in algorithm for better adaptation of the filter. Subsequently, an 'Edge map' is used to enhance the edges in the image. The effectiveness of the proposed filter has been evaluated quantitatively and qualitatively in terms of various quality metrics. The results indicate that the proposed technique enhances the efficiency of well known spatial domain filters for processing ultrasound images both in terms of speckle suppression and edge enhancement. To quantitatively evaluate the image refinement technique, the performance indices require noise free images or 'ground truth' images. This evaluation has been conducted on some well known test images, downloaded from [35] which include synthetic and real ultrasound images.

1.4.3 Liver Classification using Information Fusion

After speckle reduction, texture features are extracted from a Region of Interest (ROI). Since liver is very large tissue, therefore, experiments were conducted to find the appropriate ‘size and location’ of ROI. It has been observed from the study, that a size of 30x30 pixels is optimal, and it should be taken along (or near) the centre line of the image [36]. Moreover, the radiologists suggested that ‘small and multiple ROIs’ are better than ‘a single big’ ROI for feature extraction. Therefore, three ROIs have been selected from liver image near the centre and 35 features (from different texture models like SGLCM, GLDS, FOS, TEM, FPS, SFM and Fractal Features) are extracted from each ROI. The feature set is reduced to the optimal number of features using Fisher’s Discriminative Ratio (FDR). FDR is based on Linear Discriminate Analysis (LDA) and is used to evaluate the ability of a feature to separate the two classes. High FDR means more ability of a feature to distinguish between two classes (normal and fatty in this case). Subsequently, Box-plot analysis and Pearson’s Correlation Coefficient (PCC) techniques have also been used for selecting the best 7 features with highest discriminative power. These selected 7 features are then fused using a linear classifier, in which their FDR weights and ‘weighted z-score values’ are used to compute *discriminative index* (D_I) for liver classification. Using training set, an optimal value of threshold for D_I is computed for 100% sensitivity (no malignant tissue is reported as benign). The numerical value of D_I is the final metric to classify liver, if D_I is greater than or equal to the threshold, then liver is ‘fatty’ otherwise it is ‘normal’ liver. The comparison of the proposed method with well-known existing classifiers has been done on testing set images. The results show that the proposed method performs better than Fuzzy kNN, Back propagation NN classifiers [36].

1.4.4 SVM based Liver Tissue Characterization

The extent of fat accumulated in the liver is more important than presence of fat in the liver because it helps the physician to decide the dose of medicine and treatment. Therefore, another classifier based on Support Vector Machine (SVM) approach is proposed to further characterize the fatty liver as *mild, moderate* and *severe* fatty. This method utilizes the ratio of some gray level based texture features of liver to the features of the kidney. For this purpose three ROIs were selected from liver and one from the right kidney. The optimal 7 texture features and two more features Short Run-length Emphasis (SRE) taken from Grey Level Run-length Matrices (GLRM) and 'DM1sym4' from Discrete Wavelet Transform (DWT) recently proposed by Acharya *et al.* [32] were extracted from each ROI. Then average of each feature from three ROIs is computed for further analysis. Novelty of this method is that, grey level based features of liver are compared with same features of the right kidney (renal cortex) in the given image and thus, quality of the image does not affect the final classification. This makes the proposed method independent of machine settings. Then optimal set of features is used with multiclass SVM classifier for characterization of fatty liver. This method has 98.3% overall accuracy to characterize the fatty liver into its sub classes, which is found to be better than the other recent methods [31-33, 37, 38].

1.5 SIGNIFICANCE OF THE RESEARCH WORK

The present research work proposes a computer aided method for liver tissue characterization. The research illustrates the following points. First, an edge preserving speckle suppression technique is proposed, which may be used as a preprocessing tool in image analysis and other automatic operations on ultrasound images. Second, an optimal set of texture features is identified for liver tissue characterization. Third, using information fusion, a new classification method is proposed, which is a linear combination of features, weighted with their class separation ability. Subsequently, a new index 'D_I' is proposed which is useful for the radiologists to classify the liver. Finally, a SVM based method is proposed for further characterization of fatty liver as 'mild', 'moderate' and 'severe'. Novelty of this method is that the ratio of grey level features of liver and kidney is used. Since 'hepato-renal ratio' based features are used for characterization, therefore, this method is independent of machine settings.

The outcome of this research study will be useful for radiologists to evaluate the ultrasound images for characterization of liver. However another contribution of the research is the formulation of a classification method based on *'information fusion'*, which is useful to any binary classification problem. In future, the work can be extended to hardware implementation of the proposed SVM based characterization method on ultrasound machines, and the radiologists can be assisted in early diagnosis of *Steatosis* .

1.6 ORGANIZATION OF THE THESIS

The thesis is organized in seven chapters. The Chapter 1 gives the introduction of the research work and discusses the motivation behind the present research work. A brief literature review of the related work has been presented and subsequently the research gaps are defined. In the end of this chapter, objectives of the research work are presented followed by the work done and organization of the thesis.

Chapter 2 explains the basic physics behind ultrasound imaging, the instrumentation involved in it and types of the ultrasound imaging. A brief introduction of human liver, its anatomy and interaction of liver tissue with ultrasound waves is presented in this chapter. The procedure for image acquisition, ultrasound machine settings and generation of image database is also presented here. In the end of this chapter, various indices related to evaluation of image quality and classification accuracy are described with their mathematical background.

Ultrasound images are affected with inherent speckle noise, which makes the visual presentation of image poor quality. In Chapter 3, various speckle reduction techniques are discussed through their comparative analysis. To address the demerits of existing spatial domain filters, the proposed speckle suppression method based on local statistics and edge map is presented.

Chapter 4 investigates the need and importance of the Region of Interest (ROI). Since liver is very large tissue therefore a specific area or ROI is selected. The *'size and location'* of the ROI is very crucial. For reliable texture features, location and the optimal size of the ROI is discussed in this chapter.

Chapter 5 explains significance and background of the various features taken from different texture models. Using Linear Discriminative Analysis and statistical analysis, seven best features are selected for liver tissue classification. Finally, the selected features are combined in a linear equation along with their normalized weight to form a new classification method to classify normal and fatty liver.

In Chapter 6, liver tissue characterization method is presented which is able to further characterize the fatty liver as 'mild fatty', 'moderate fatty' and 'severe fatty' from the ultrasound images. The second proposed method utilizes the ratio of the 'grey level based' features of liver and kidney.

Chapter 7 concludes the research contributions and highlights the important findings based on the experimental analysis and observations. Scope for the future work and possible extensions to this work are also discussed for the new researchers in this area.

CHAPTER-2

DIAGNOSTIC ULTRASOUND IMAGING

2.1 INTRODUCTION

Medical ultrasound is a widely used imaging modality for many clinical applications like abdominal imaging, fetus analysis, liver diagnosis, echocardiography etc. Since ultrasound is real-time imaging modality that does not use any ionizing radiation, hence, it is generally preferred over other imaging modalities. Moreover, the equipment used for ultrasound imaging is small and inexpensive relative to other modalities such as CT and MRI therefore, it is widely used in small clinics and in rural areas. Even the flagship program of World Health Organization (WHO), the *Door to Door Healthcare* (D2DH) in underdeveloped countries, includes ultrasound imaging as primarily diagnostic tool due its portability and other aforesaid advantages. In this chapter, the basic physics of ultrasound imaging, a brief description of the instrumentation involved in ultrasound imaging and the types of medical ultrasound imaging is presented. An overview of liver anatomy and liver tissue interaction with ultrasound is also given as a prerequisite to this research work. Performance indices used for evaluation of image enhancement and classification accuracy are presented in the end of this chapter.

2.2 MEDICAL ULTRASOUND

Ultrasounds are the sound waves with high frequency from 20 kHz to 10 GHz and travel in a medium as pressure waves. In medical applications, ultrasound ranges from 1MHz to 30MHz. The ultrasound echoes from pressure waves are used to obtain information about tissue within the body for medical investigation. An ultrasound image is obtained by placing the ultrasound probe (piezoelectric transducer) against the skin of a patient near the region of interest. The piezoelectric transducer converts the electrical signal into an ultrasound pulse or wave that penetrates into the body. As the pulse propagates through the tissue, structures in the tissue produce reflections that travel back to the transducer. The strength of a reflected signal contains information about the reflecting structure, and the delay between sending a signal and receiving an echo indicates the distance between the structure and the transducer. These mechanical echoes are converted back to electrical signals by the transducer. Then, these electrical signals are amplified, demodulated and finally converted into real images in an ultrasound imaging system. The general schematic organization of an ultrasound imaging system is shown in Figure 2.1. As the frequency of the ultrasound wave increases, it undergoes stronger attenuation in the body and thus wave penetration is reduced. Therefore, frequencies between 3MHz to 5 MHz are used to image the large body parts such as liver and kidneys at a depth of 15 to 20 cm from the skin [39, 40].

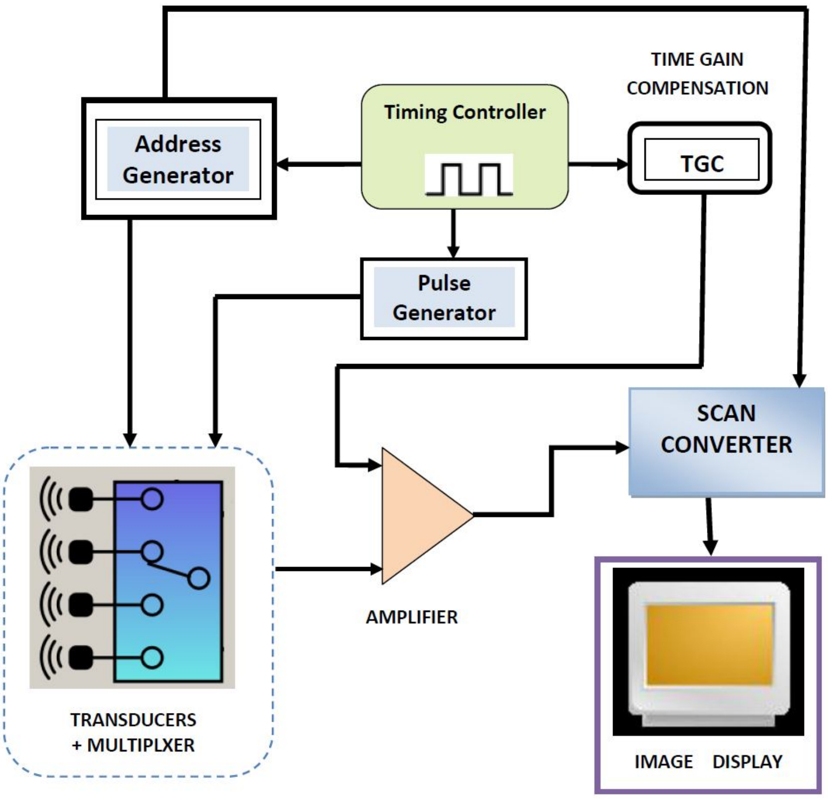

Figure 2.1 Block Diagram of Ultrasound Imaging Process [41]

2.3 PHYSICS OF THE ULTRASOUND IMAGING

The speed of propagation of ultrasound waves '*s*' is defined in terms of the frequency '*f*', and wavelength 'λ', by

$$s = f\lambda \tag{2.1}$$

The speed of propagation varies depending on the density 'ρ', and compressibility of the medium. Speed of sound in air is 330 m/s, whereas in the bones, it is 3500 m/s. In most of the human tissues, speed of the sound '*s*' is approximately 1540 m/s, and this value is typically used by the scanning equipment for various calculations [39].

The incident pulse is reflected when it encounters an interface between two materials with different density. The reflectivity coefficient, '*R*' relates the amplitude of the reflected signal to the amplitude of the incident signal as

$$R = \frac{Z_1 - Z_2}{Z_1 + Z_2} \tag{2.2}$$

Where, '*Z*' is the acoustic impedance of the medium and is given by

$$Z = \rho \cdot s \tag{2.3}$$

There is a significant impedance discontinuity at the interface of two tissues due to which, a strong reflection is produced, resulting to a bright spot in the image. Ultrasound radiologists are experienced enough to identify a physiological feature using this intensity variation. The reflection from an interface that is large with respect to the wavelength is called '*specular reflection*' and it is the main reason that produces a feature in an ultrasound image. On the other hand, if the texture of the reflecting interface is small with respect to the wavelength, the result is scattered reflection. The strength of scattered reflection received at the transducer is much lower than that of specular reflection, and this produces a distinctive grainy texture in the image known as '*speckle*'. The signal is also attenuated as it propagates through the tissue. This attenuation is caused by absorption in the media, reflection and refraction at media interfaces, and scattering from tissue structure. The attenuation varies depending on the material and increases approximately linearly with frequency and depth. Higher frequencies suffer greater attenuation, however it produces image with better resolution. The compensation for the attenuation in the tissue is achieved by increasing the gain for more distant echoes and, is known as Time Gain Compensation (TGC), which is controlled by the machine user or set automatically by the scanning equipment.

Further, the frequency of the transducer selected for a particular clinical test depends upon the location of the organ being examined. High frequency transducers provide more detailed images and are used to examine the organs close to the skin surface, such as the thyroid. Hence, image resolution is constrained by the location of an organ with respect to the surface of the body. The attenuation mechanism in ultrasound imaging is directly related to the tissue being imaged and to the propagating wave frequency. The wave amplitude in soft tissues is proportional to the attenuation coefficient (α) under the assumption that homogeneous tissues exhibit a simple exponential loss of pressure amplitude as the wave propagates [42].

2.4 INSTRUMENTATION INVOLVED IN ULTRASOUND IMAGING

The quality and accuracy of the final image depends upon the instrumentation used in the equipment. Starting from transducers to signal conditioning circuits, signal processing and display systems, all the components have their own importance. This section explains the essential components/instrumentation involved in ultrasound imaging system are explained in this section.

2.4.1 Ultrasound Transducer and Probe

The transducer used to capture an image has a substantial role in the formation of ultrasound image because it affects the appearance of features and the shape of the scanned area. Piezoelectric crystal or piezoelectric transducer (PZT) is most popular transducer for ultrasound generation and receiver. It works on the principal of piezoelectric effect, according to which, “*if an electric potential is applied across a piezoelectric material, it tends to contract or expand (and vice versa)”,* i.e., an alternating electric field causes the frequent expansion and contraction and therefore, vibration are produced in the piezoelectric crystal [42]. The maximum amplitude of vibration is achieved, when the electric field stimulates a natural frequency of the crystal. There are several piezoelectric materials being used as transducers. This includes some natural crystals like quartz, Rochelle salt etc., but the most commonly used substance is a synthetic material (Lead Zirconate Titanate). The crystal is cut into a specific shape to ensure that most of the energy is emitted at the fundamental frequency. The basic structure of an ultrasound probe is shown in Figure 2.2.

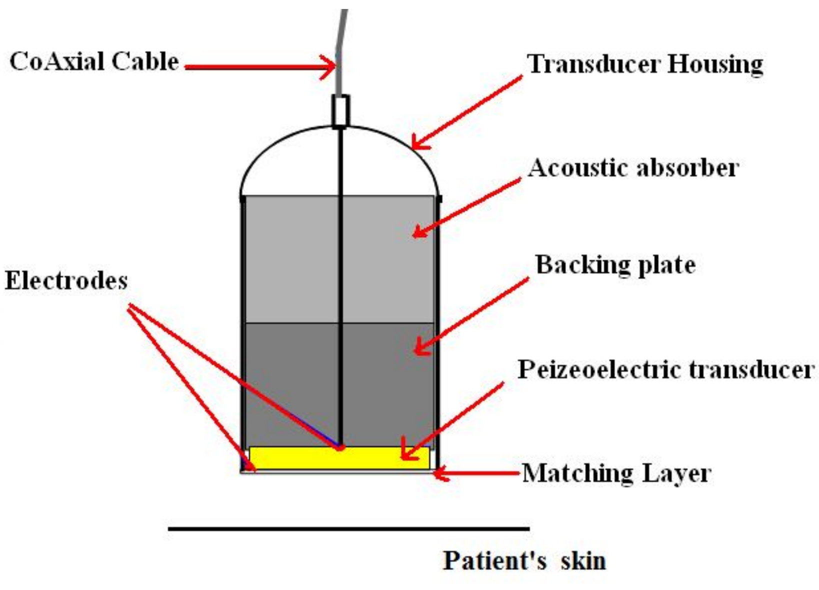

Figure 2.2 Components of an Ultrasound Probe [41]

A probe contains a matching layer, electrodes, PZT, a backing plate and an acoustics absorber. All these components are housed in an aesthetically designed plastic cover, called *probe*, and is connected to the ultrasound machine through a coaxial cable. First of all, the matching layer comes into contact with patients' skin through a conductive jelly. The jelly is used for acoustic impedance matching and less attenuation of ultrasound waves to get a better quality image. The backing plate, such as epoxy, loads the back side of the array elements. The faceplate protects the transducer assembly and also may act as an acoustic lens. The transducer bandwidth and sensitivity depends upon the backing and matching layers. A matched backing improves bandwidth, as well as it dissipates acoustic energy also, that could otherwise be transmitted into the tissue medium. Therefore, a low-impedance acoustic backing is preferred because it reflects the acoustic pulses toward the front side of the transducer [43].

There are many types of probes available with different sizes and shapes such as mechanically rotated single crystal transducer, linear-array transducer, and phased-array transducer. In the basic model, a single PZT element is mechanically steered through an arc to generate a sector. In this case the transducer is either a single mechanically rotated crystal as shown in Figure 2.3(a), or a multi-element transducer. The multi-element transducers can steer the ultrasound beam electronically. A linear sequenced array is composed of a large number of elements arranged side by side along their length and acoustically isolated from each other. The number of elements normally varies between 128 and 256. The size of each individual element depends on the frequency of operation, and is smaller for higher frequencies. A typical individual element for 3.5 MHz operation is 1 mm wide and 10 mm long. The beam is controlled by activating group of elements in a sequence.

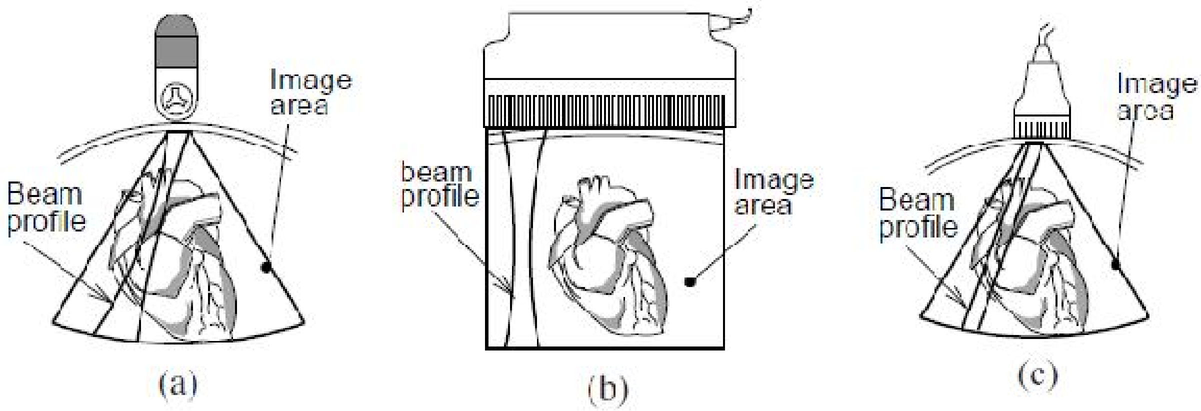

Figure 2.3 Types of Ultrasound Probes [44]

The linear array probe with a flat face perform a linear scan and orthogonal to the beam direction. This probe produces a rectangular image with low distortion, good transverse resolution and high frame rate. This probe scans the tissue by activating groups of elements directly above the tissue as shown in Figure 2.3(b). However, these probes are large in size having width ranging from 5 to 20 cm, which makes it difficult to maintain good contact between the patient and the transducer for different orientations.

A linear phased array is even more compact and produces a wedge shaped scan. A phased array consists of multiple PZT elements, generally arranged parallel to each other. In this case, the beam is steered through an arc by phasing of elements instead of sequencing of elements. Similarly, the beam is electronically focused by activating elements at the periphery of the array differentially to those in the center of the array. The phased array uses all of its elements and steers the beam in different directions as shown in Figure 2.3(c). The phased array or curved array transducers are used for the imaging of abdominal organs such as the liver, kidneys and pancreas.

2.4.2 Time Gain Compensation

In order to compensate for the effects of absorption and focusing, imaging systems have a method called Time Gain Compensation (TGC) built in as a set of controls. The depth of the image is divided into horizontal (linear format) or radial (sector format or curved linear array format) strips, each of which is connected to a separate amplifier stage with a variable gain. These gain controls can be adjusted manually to increase the gain independently in each strip zone. In order to balance the effects of absorption, TGC provides a means to increase gain with depth in a stepwise manner. The adjustments in TGC are made to approximate a uniform background level throughout the field of view. When a Radio Frequency (RF) signal received from TGC, it is amplified using specialized amplifier. Then scan converter converts the RF signal to an image according to the information given by the address generator in reference to X-Y coordinates of the probe movements.

2.5 TYPES OF ULTRASOUND IMAGING

The type of ultrasound imaging depends upon the method of displaying the electrical signals obtained from the ultrasound echoes. The simplest display method is Amplitude mode (also known as ***A-mode***) in which, the echo is displayed against the time in one direction. This display mode is a one-dimensional display showing echoes along the ultrasonic beam as vertical spikes on a horizontal time axis indicating the depth of the reflectors [40]. Thus, it is just like a signal trace on an oscilloscope, as shown in Figure 2.4. The amplitudes of the spikes are directly proportional to the echo strengths and the horizontal position of the spikes is determined by the time difference between the transmission of the ultrasound pulse and the arrival of the echo at the transducer [45]. This mode is obsolete in medical imaging however, it is still being used in applications like crack detection, distance measurement etc.

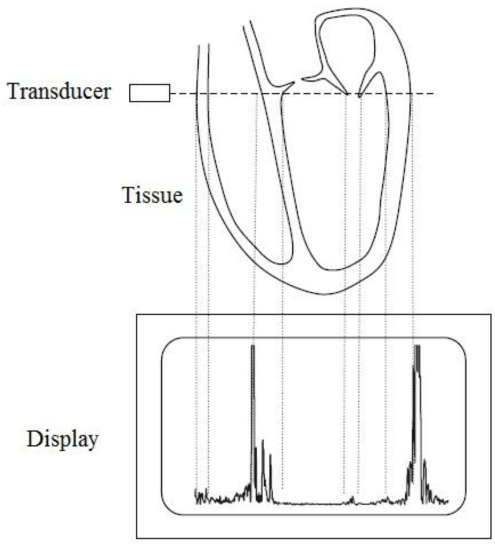

Figure 2.4 *A-Mode* Ultrasound Imaging Display [42]

The second type of display is the ***B-mode*** imaging (brightness mode imaging), which displays a two-dimensional grayscale image. The multiple scans at regular intervals are taken and the strength of an echo at a location is displayed as the brightness of a spot. Small bright dots on the screen are produced whenever the sound wave encounters a nearly perpendicular boundary. Therefore, an ultrasound image of a tissue surface is made up of the bright dots on each scanning line traveled by each ultrasound pulse as shown in Figure 2.5. This mode is the most commonly used in medical imaging and therefore, the present work focuses on the ***B-mode*** ultrasound imaging. The ***B-mode*** is formed by coding the ***A-mode*** line as brightness along one line of sight and then by linearly scanning the transducer at a uniform velocity. The ***B-mode*** needs some kind of mechanical or electronic technique to radially sweep the ultrasound beam into the tissue. A sector sweep is achieved using the phased array method, where a phase difference is introduced between adjacent transducers to flex the plane wave front, without having to mechanically move the transducer [40].

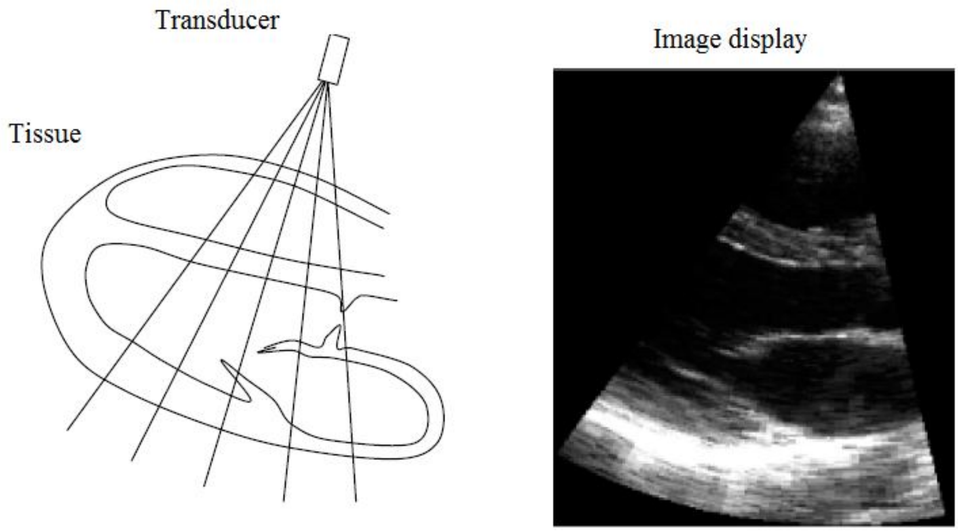

Figure 2.5 *B-mode* Ultrasound Imaging Display

Since ***B-mode*** is made of many different beams, it has a much lower imaging rate than the ***A- mode***. Another mode is ***M-mode*** (motion mode imaging), which displays the motion of the tissue. In this mode, the scanning rate of transducers is very fast. The echoes generated by a stationary transducer are recorded continuously over time. This allows real time images to be generated, displaying the motion over time as well as structure. This mode is used to analyze moving structures, such as heart valves [40].

2.6 LIVER ANATOMY AND TISSUE CHARACTERIZATION

The liver is the largest organ, present inside the body just below the right lung and the diaphragm. The liver lies close to the colon, the intestines and the right kidney. The human liver weighs from 1400 gm to 1600 gm for a normal adult, and is deep red in color due to a rich blood supply. It is shaped like a wedge and has two lobes; the right and the left as shown in Figure 2.6. The liver performs several important functions such as, controlling the metabolic process and subsequently in the absorption of nutrients. It secretes a substance called *bile*, necessary for breakdown of bigger fat molecules into smaller forms. The bile reaches the small intestine through the bile duct, during the digestive process. It also stores various nutrients such as fat, carbohydrate, proteins and vitamins [39]. There are several liver related diseases like viral hepatitis, cirrhosis, lesion etc., however, fatty liver is the most common disease in general.

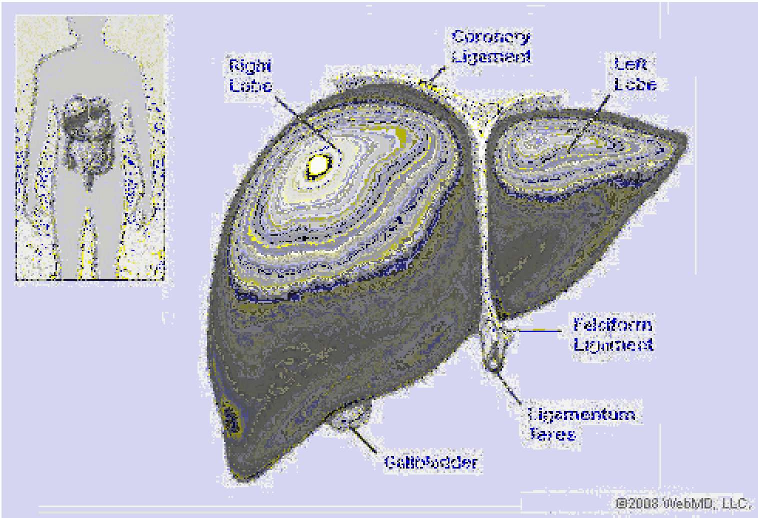

Figure 2.6 Anatomy of the Liver [46]

2.6.1 Fatty Liver

Fatty liver or *steatosis* is not dangerous for the liver, but it is a condition that can be lead to some other perilous diseases like fibrosis, cirrhosis or even further to liver cancer. Fat accumulates in the liver usually in connection with heavy use of alcohol, obesity or diabetes. Fatty liver may also occur with poor diet and certain illnesses, such as tuberculosis, intestinal bypass surgery for obesity, and certain drugs like corticosteroids [39]. A patient has fatty liver when the fat increases the weight of the liver by 5%. The possible reasons for fatty liver include the transfer of fat from other parts of the body, or an increase in the extraction of fat presented to the liver from the intestine. This is caused by increased accumulation of triglycerides within the hepatocytes. This change in metabolism is due to numerous hepato-cellular disorders including alcoholic liver disease, obesity, diabetes mellitus, starvation, gastrointestinal bypass surgery, endogenous and exogenous steroids, drug-induced liver disease, nutrition, severe hepatitis and cystic fibrosis [47, 48].

The fatty liver is usually detected during routine blood screening in which a mild elevation of liver blood tests is reported. For preliminary investigations, ultrasound or CT scan of abdominal is used to detect the presence of a fatty liver. In the ultrasound test, a fatty liver produces a bright image in a ripple pattern. Fatty liver is easily curable in its early stage. Therefore, the timely detection and treatment is crucial for control of the further deterioration of liver. In marginal cases, CT scan of the liver is analyzed to diagnose the fatty liver. To ensure, whether a patient has fatty liver or not, a sample of liver tissue is obtained for biopsy. Clinical diagnosis using B-mode ultrasound images relies on the image quality and experience of technicians and doctors to a large extent. Using the subjective judgment and non-quantitative description, doctors determine the incidence and the severity of fatty liver. However, the poor image quality, speckle noise, and the use of different types of ultrasound imaging system, and various physical conditions of patients obstruct a unified diagnostic standard. Therefore, a computer-aided quantitative analysis of liver ultrasound image is necessary to contribute in establishing an objective diagnostic method for fatty liver. This quantitative diagnostic method may improve the clinical diagnostic accuracy and decrease inter-observer variability.

2.6.2 Grading of Fatty Liver

Liver grading is being done to assist the physician for treatment and further investigations. Clinically, physicians or radiologists perform visual grading of fatty liver on the basis of liver surface texture (brightness and grey level variation), echo penetration and visibility of diaphragm with respect to liver. The clinical features of fatty liver includes (i) diffusely increased parenchyma echogenicity, often associated with unusually fine liver texture; (ii) increased attenuation of the ultrasound beam causing poor visualization of the posterior portions of the liver; and (iii) decreased visualization of the portal and hepatic veins, probably secondary to compression by the surrounding fat-laden parenchyma as well as increased attenuation of sound and decreased contrast between echogenic fat and the walls of the vessels.

The fatty liver is further categorized as Mild fatty liver or grade 1, Moderate fatty liver or grade 2 and Severe fatty liver or grade 3. In ***grade 1***, echogenicity is slightly increased, with normal visualization of the diaphragm and the intra-hepatic vessel borders. Figure 2.7a demonstrates the mild fatty infiltration. The sagittal view shows slightly increased echogenicity. Visualization of the vessel borders (white arrow) and the diaphragm is normal. In ***grade 2***, echogenicity is moderately increased, with slightly impaired visualization of the diaphragm or intra-hepatic vessels. Figure 2.7b demonstrates moderate fatty infiltration. The sagittal view shows moderately increased echogenicity. Visualization of the vessel borders (arrow) is slightly impaired. In ***grade 3***, echogenicity is significantly increased, with poor or no visualization of the diaphragm, the intra-hepatic vessels, and posterior portion of the right lobe. Figure 2.7c shows severe fatty infiltration. The sagittal view shows considerably increased echogenicity. Parts of the diaphragm (shown by white arrows) are poorly visualized, and visualization of the vessel borders (black arrow) is impaired [49].

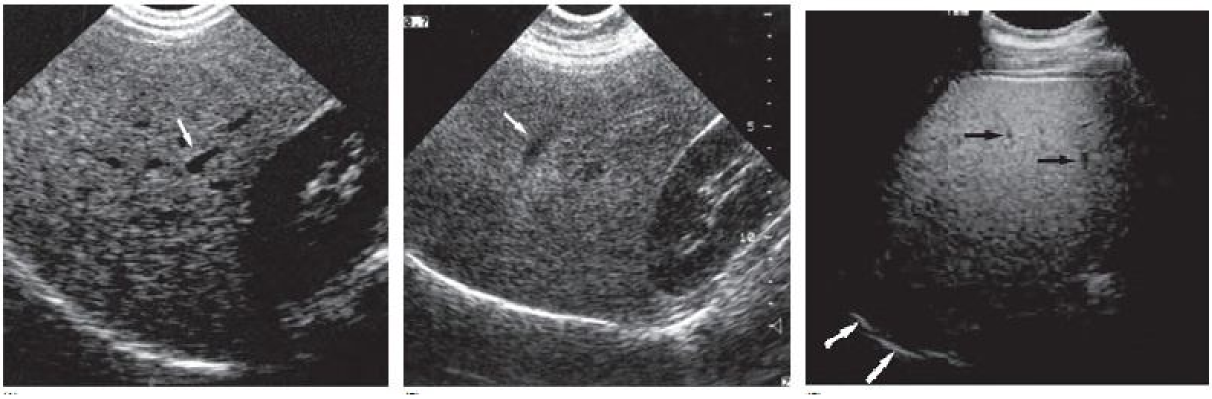

(a) (b) (c)

Figure 2.7 Fatty liver characterization. (a) Mild fatty (b) Moderate fatty (c) Severe fatty liver

The researchers have understood that as compared to CT and liver biopsy, the overall accuracy of ultrasound in detecting fatty infiltration is 85% to 89%, and the specificity is 56% to 93% [49, 50]. Quantitative methods for measuring liver echogenicity and attenuation and frequency-modulated ultrasound is used in experimental settings for the diagnosis of diffuse parenchymal diseases of the liver. However, most of these methods are computationally time consuming and are not used in clinical ultrasound practice [47, 51]. Therefore, in the present work the emphasis is made upon a computer-aided objective method for liver tissue characterization to help the radiologists in a better way.

2.7 ULTRASOUND IMAGE ACQUISITION AND DATABASE

The dataset or database of the information is a crucial part of any research. In this research work, two databases were used; one for image enhancement and other for liver tissue characterization. For the analysis of speckle suppression and quality of image enhancement method, noise free images or “ground truth” test images were used. These test images include synthetic images, natural images and real ultrasound images. These images are obtained from the home page of Aleksandra Pizurica [52]. More test images were created by simulating speckle on these standard noise free images using Aleksandra Pizurica’s algorithm in

MATLAB ver. R09a. In this process, nine images were generated from each “ground truth” test image by adding speckle noise with different values of standard deviation (σ=0.50, 0.55, 0.60, 0.65, 0.70, 0.75 0.80, 0.85, and 0.90), and these images were used for evaluation of various speckle suppression methods. Some of the noise free test images and the noisy test images are shown in Figure 2.8.

The second database was required for liver tissue characterization. Since there was no standard database of liver ultrasound images available in the public domain, therefore to carry out the research work, liver ultrasound images were obtained by the experienced radiologists from PGIMER Chandigarh, and Delta Diagnostic Centre Patiala. The sample images used for analysis were acquired with Voluscan730 PRO (General Electric Medicare) ultrasound machine with 68 mm curved array probe at 3.6 MHz frequency. The TGC setting was done in such a way that the background grey level was almost the same throughout the depth. The patients had eight hours fast before the ultrasound scan to avoid the effects of changing the liver glycogen and water storage on ultrasound imaging [53]. Experienced radiologists were requested to acquire the images and to label them as per the standard procedure.

The present study is conducted on 240 ultrasound liver images (one image per patient), out of which 140 images are used for training (50 normal and 90 fatty liver images) and the remaining 100 images (30 normal and 70 fatty liver images) are used for testing. All the patients were within the age group of 25 – 60 years. The study is conducted on 148 men and 92 women (total 240) patients. In each image, the Region of Interest (ROI) is selected along the center line of the image to avoid any distorting effect. Depth of the ROI is selected in such a way that blood vessels are avoided in ROI. Therefore, the ROI is selected by the experienced radiologists. Multiple ROIs have been selected from a single image to increase the size of dataset and for reliable statistical analysis.

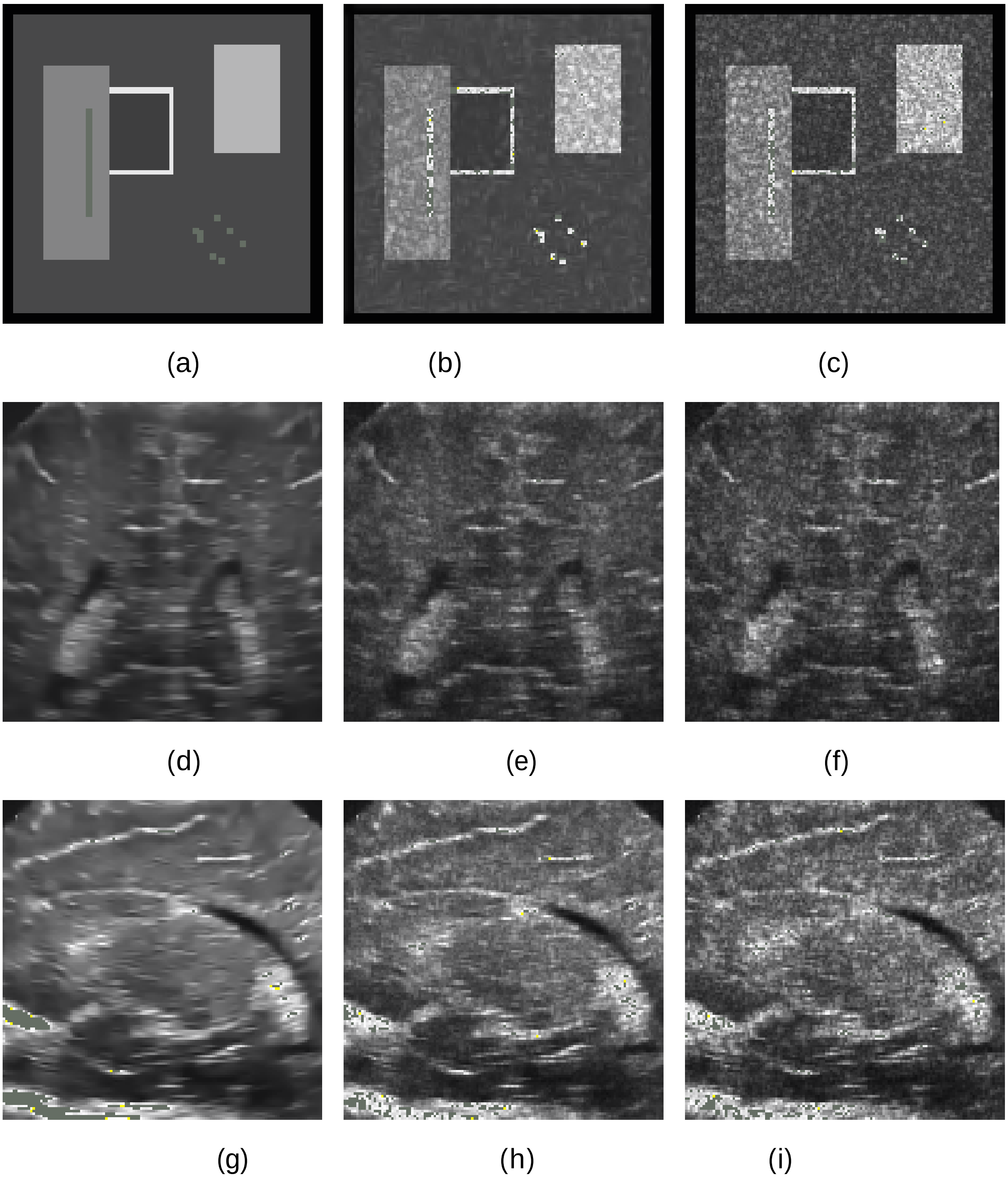

Figure 2.8 (a) Noise free image IM1 (b) noisy image IM1_7 with speckle noise of σ = 0.7 (c) noisy image IM1_85 with speckle noise of σ = 0.85 (d) Noise free image IM2 (e) noisy image IM2_7 with speckle noise of σ = 0.7 (f) noisy image IM2_85 with speckle noise of σ = 0.85 (g) Noise free image IM3 (h) noisy image IM3_7 with speckle noise of σ = 0.7 (i) noisy image IM3_85 with speckle noise of σ = 0.85

As suggested by the radiologists, three ROIs are selected from liver image near the centre. A 30x30 square sized ROI (900 pixels) provides a suitable sample size for reliable statistics [25]. Some of the acquired images, used for testing and training datasets are shown in Figure 2.9.

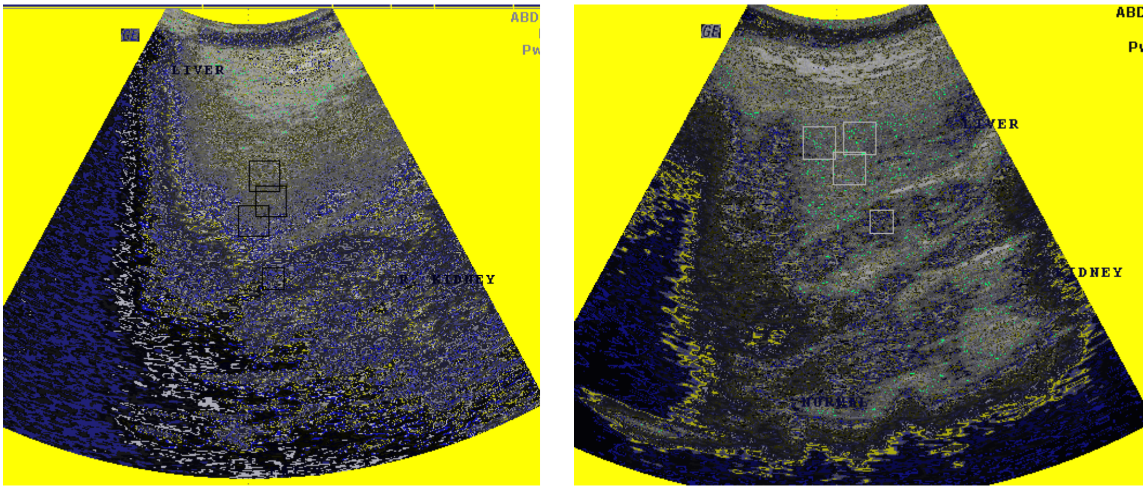

Figure 2.9 Real Ultrasound Images used in Database

2.8 PERFORMANCE QUALITY METRICS

2.8.1 Image Quality Metrics

The performance of each filter has been evaluated quantitatively through well-established image quality metrics like: Signal-to-Noise Ratio (SNR), Correlation Coefficient (CoC), Structure Similarity Index (SSI), Signal to Mean Square Error ratio (S_MSE) and Edge Preserving Index (EPI). The computation of image quality metrics requires "ground truth" image, noisy image *I* and a filtered image *F*. The noisy images are taken as input image to different filters, and the filtered images are compared on the basis of these image quality metrics. Their formulations are as follows:

(a) Signal-to-Noise Ratio (SNR): The signal-to-noise ratio is ratio of variance of noise free image to the variance of error between noise free image and processed image. This is calculated as

$$SNR = 10 \cdot \log_{10}\left(\frac{\sigma_g^2}{\sigma_e^2}\right) \tag{2.4}$$

where, σ^2_g is the variance of the noise-free reference image and σ^2_e is the variance of error (between the original image *I* and denoised image *F*). The larger SNR values correspond to a good quality image [52].

(b) Edge Preserving Index (EPI) : The filter's edge preservation ability is computed by

$$EPI = \frac{\sum(\Delta I - \overline{\Delta I})(\Delta F - \overline{\Delta F})}{\sqrt{\sum(\Delta I - \overline{\Delta I})^2 \sum (\Delta F - \overline{\Delta F})^2}} \tag{2.5}$$

where, ΔI and ΔF are the high-pass filtered versions of images *I* and *F,* obtained with a 3×3 pixel standard approximation of the Laplacian operator. The larger value of EPI means more ability to preserve edges.

(c) Correlation Coefficient (CoC): This is also known as Pearson's correlation coefficient. It is a measure of similarity between two images. It is calculated by

$$CoC = \frac{\sum (I - \bar{I})(F - \bar{F})}{\sqrt{\sum (I - \bar{I})^2 \sum (F - \bar{F})^2}} \tag{2.6}$$

where, $\bar{I}$ and $\bar{F}$ are the mean of original and denoised image, respectively. The CoC is the key measure of similarity between the ground truth image and despeckled image. Its value varies from 0 to 1. A value closer to 1 indicates a good quality processed image.

(d) The Structural Similarity Index (SSI): The SSI between two images is computed as

$$SSI = \frac{(2 \cdot \bar{I} \cdot \bar{F} + 2.55)(2\sigma_{IF} + 7.65)}{(\bar{I}^2 + \bar{F}^2 + 2.55)(\sigma_I^2 + \sigma_F^2 + 7.65)} \tag{2.7}$$

This index represents the perceptual image quality of an image with reference to a ground truth image. The value of SSI index lies between -1 and 1, and value 1 is only reachable in the case of two identical sets of data [54]. This index was proposed by Wang *et al.* in 2004 and is widely used in image compression and image enhancement methods.

(e) Signal to Mean Square Error ratio (S_MSE): The S_MSE is the ratio of signal to the mean square error. In case of high variance speckle, the standard SNR is not good indicator of noise suppression. So to evaluate the noise suppression efficiency in coherent imaging modality the better way is to calculate Signal – to MSE ratio i.e. S_MSE [55]. This S_MSE is given by

$$S\_MSE = 10 \cdot \log_{10} \cdot \left(\frac{\sum_{pixels} S_1^2}{\sum_{pixels} (S_1 - S_2)^2} \right) \tag{2.8}$$

where, $\sum_{pixels} S_1^2$ represents variance of filtered image, and denominator

$\sum_{pixels} (S_1 - S_2)^2$ is mean square error in noisy and filtered image.

2.8.2 Sensitivity and Specificity Analysis

The performance of classification methods is evaluated by Receiver Operating Characteristics (ROC) analysis through *Specificity, Sensitivity and Accuracy* [56, 57]. This analysis is based on the number of correct instances in each class out of total instances. The True Positive (TP) is the number of instances when the disease is correctly detected. The False Positive (FP) is the number of instances when the patient does not have the disease but it was detected as disease. False Negative (FN) is the number of instances when the patient has the disease but it was not detected. In medical related classification methods, this number is very critical, because if some method has even a single instance in FN then it means the method may miss the detection of disease, which is not at all desirable in medical imaging. The True Negative (TN) is the number of instances when the disease is not present and the method also recommend the same. All these terms are represented in Table 2.1. On the basis of this formulation, the following terms are used to indicate the performance of classification method.

Table 2.1

Evaluation of Classification Accuracy

		Is the liver *fatty*?	
		Yes	No
Did the test indicate the presence of fatty liver?	Yes	True positive (TP)	False positive (FP)
	No	False negative (FN)	True negative (TN)

Sensitivity, also called True Positive Fraction (TPF) is defined as the ratio of "number of correct positive assessments to the number of truly positive cases".

$$Sensitivity = \frac{TP}{TP + FN} \tag{2.9}$$

Specificity, or True Negative Fraction (TNF) is defined as the ratio of the number of correct negative assessments to the number of truly negative cases.

$$Specificity = \frac{TN}{TN + FP} \tag{2.10}$$

Accuracy is defined as the ratio of "number of correct assessments" to the "total number of cases".

$$Accuracy = \frac{TP + TN}{TP + TN + FP + FN} \tag{2.11}$$

2.9 SUMMARY

In this chapter a foundation has been made for further discussion on ultrasound imaging as a diagnostic tool. An overview is presented about interaction of ultrasound waves with liver tissue and liver anatomy, to understand the physiological significance with texture analysis. A description about the image database collections and generation is also given. The quality metrics used to evaluate the performance of image enhancement methods and the performance of classification methods are also explained.

CHAPTER-3

ULTRASOUND IMAGE ENHANCEMENT

3.1 INTRODUCTION

Ultrasound imaging is a low-cost, non-invasive and portable diagnostic technique; however, it has the drawback of speckle. Speckle is a locally correlated multiplicative noise having granular pattern, and this makes the visual quality of ultrasound image poor. Another disadvantage of speckle is that it makes automatic image-processing and analysis more difficult. Therefore, speckle suppression is an important step before application of any other automatic image processing technique like segmentation or classification. In this chapter various methods to suppress this speckle present in images are discussed. Later on, an improved method of speckle suppression is proposed which performs better than the previous ones.

3.2 LITERATURE REVIEW

Speckle arises from random variations in the strength of the backscattered waves. Speckle may contain some important information, but still it is undesirable because it significantly reduces the visual image quality and increases the difficulty in discriminating fine details in images during diagnostic examinations [58, 59]. Early attempts to suppress speckle noise were implemented by averaging of uncorrelated images of the same tissue recorded under different spatial positions [3, 4]. Although these methods are effective for speckle reduction, however they need multiple images of the same object and therefore making them complex and time consuming [5]. Speckle reduction filters can be categorized into following groups: filters based on local statistics, based on homogeneity, anisotropic diffusion based, fourth order partial differential equation based filters, wavelet based filters and other multi-resolution filters [60]. In local statistics filters' group, Lee [3, 61], Frost [62] and the Kuan [5] are some of the well known filters. In the homogeneity group, the filtering is based on the most homogeneous neighborhood around each image pixel. Anisotropic diffusion [6, 7, 63, 64] filters remove noise from an image by using a Partial Differential Equation (PDE). Depending on the image edges and their directions the smoothing is carried out based on the image gradient. Perona and Malik [6] modified the isotropic diffusion by using an "*edge-stopping*" function $g(|\nabla I|)$, which makes the smoothing a function of "*edges*" in the image. Yu and Acton [8] proposed Speckle Reduction Anisotropic Diffusion (SRAD) in which diffusion constant is replaced with "instantaneous coefficient of variation" as a function of the local gradient magnitude and laplacian of image. However in this method, a reference homogenous area is to be selected manually and this makes this technique a non-persistent and user dependent. You and Kaveh [9] proposed a class of fourth-order partial differential equations (*fpde*) for speckle reduction. This technique can suppress speckle, however it cannot preserve edges and some useful details, because this method blurred the edges. In the wavelet category, filters make use of a realistic distribution of the wavelet coefficients in which only the useful wavelet coefficients are used [11, 65-69]. Gupta *et al.* proposed a versatile technique for filtering noisy ultrasound images, which also enhance the visual outlook of the image [14].

In most of the above filters, speckle is removed in homogeneous areas but near the edges Coefficient of Variance (CoV) is very high in the window, so filters are restricted to operate and thus edges are not enhanced. CoV is the ratio of standard deviation to weighted mean in the given window. In this way, the smoothing of noise is not directional but parallel to the edges. Considering this issue as a motivation to the present work, a new technique is proposed. In this work, a technique is used along with standard spatial domain speckle reducing filters so that the efficiency of the standard filter is increased.

Generally, the spatial domain filters utilize three techniques:

i) Filters based upon local statistics
ii) Based on Homogenous region
iii) Anisotropic diffusion and other Partial differential Equation based filters

Filters from the first category, modify the central pixel on the basis of its neighborhood pixel using statistical parameters like Mean, Median, and Variance etc. Second category is of those filters, which smoothen the most homogenous neighborhood around each pixel and leave the edges. To define homogeneous user has to select some area from the image which is taken as reference. In third category, filters use PDEs to remove speckle. Main advantage of these filters is that they use a '*sigmoidal*' function rather than a step function to remove speckle.

3.2.1 Local Statistics Filters

Lee, Kuan and Frost filters are termed as standard filters for speckle reduction and use local statistics in a moving window [3, 5 ,61, 62]. These filters are popularly used in Synthetic Aperture Radar (SAR) imaging and ultrasound imaging. Later on, Loizou *et al.* proposed another local statistical filter called *local statistics mean and variance based filter* (lsmv) having better results than conventional filters [60]. Most of the local statistic based filters could be obtained by Eq. (3.1) as suggested by Loizou et al. [60].

$$F_{i,j} = \bar{I} + k_{i,j}(I_{i,j} - \bar{I}) \tag{3.1}$$

where, $F_{i,j}$ is the estimated noise-free (filtered) pixel value, $I_{i,j}$ is the noisy pixel value in the moving window, *i* and *j*, are the pixel coordinates and $\bar{I}$ is the local mean value of the window including pixel $I_{i,j}$. All the local statistics based filters differ in terms of the value of $k_{i,j}$, where $k_{i,j}$ is a weighting factor such that $k_{i,j} \in [0\ 1]$. The factor $k_{i,j}$ is a function of the local statistics in a moving window. According to Kuan, the $k_{i,j}$ factor is

$$k_{i,j} = \frac{\sigma_x^2}{\sigma_x^2 + (\bar{I}^2 + \sigma_x^2)/L} \tag{3.2}$$

where L is Equivalent Number of Looks (ENL) [60]. ENL is defined as the ratio of "square of mean to the variance" which is constant in the Gamma distribution and σ_x^2 is the variance of moving window in noisy image. They also mentioned that Lee filter is a special case of the Kuan filter when the term σ_x^2/L is removed from denominator of Eq. (3.2), then the factor $k_{i,j}$ changes to as per Eq. (3.3):

$$k_{i,j} = \frac{\sigma_x^2 L}{L\sigma_x^2 + \bar{I}^2} \tag{3.3}$$

The Frost *et al.* keep a balance between the averaging and the all-pass filters [62]. The Frost filter can be considered as an adaptive weighted-mean filter, as the value of the current pixel is assigned as

$$F_{i,j} = \sum_x \sum_y m(i+x, j+y) I(i+x, j+y) \tag{3.4}$$

The summation of *x* and *y* are done in the moving window. The coefficient *m(i+x,j+y)* is an exponentially decaying function as shown in Eq. (3.5):

$$m(i+x, j+y) = K_0 \alpha \exp(-\alpha t) \tag{3.5}$$

where, $t = \sqrt{i^2 + j^2}$ is the distance between the current pixel *(x, y)* and processed pixel *(i+x, j+y)* in the moving window, *a* is an adaptive coefficient determined by local statistics in the moving window and K_0 is the normalizing constant. It is obvious that if a approaches to 0, the filter acts as a mean filter, and if the value of a is very large, the value of the current pixel remains unchanged as it was in the case of Lee and Kuan filters.

3.2.2 Homogeneous Filters

The homogeneous filter is based on an estimation of the most homogeneous neighborhood around each image pixel [61]. The filter takes into consideration only pixels that belong in the processed neighborhood (3x3, 5x5 or 7x7 pixels) using the given equation (3.6) under the assumption that the observed area is homogeneous. The output image then is given by:

$$F_{i,j} = (c_{i,j} I_{i,j}) / \sum_{i,j} c_{i,j} \tag{3.6}$$

where, $c_{i,j} = 1$ if $(1-2\sigma_x)\bar{I} \le I_{i,j} \le (1+2\sigma_x)\bar{I}$ (3.7)

$c_{i,j} = 0$ otherwise (3.8)

The homogeneous filter does not require any parameters or thresholds to be tuned, thus making the filter suitable for automatic interpretation [4].

3.2.3 PDE based Filters

(a) An-isotropic diffusion filter

These filters remove noise from an image by using a Partial Differential Equation (PDE). Depending on the edges and their directions, the smoothing is carried out. PDE based filters are further sub-divided into two types, (i) anisotropic diffusion and (ii) fourth order partial differential equation (*fpde*). Anisotropic diffusion is an efficient, nonlinear technique for simultaneously performing contrast enhancement and noise reduction. It smoothes homogeneous regions but retains the image edges. A simple isotropic diffusion equation may be given as Eq. (3.9):

$$\frac{\partial I(i,j,t)}{\partial t} = div\,(c\,\nabla I) \tag{3.9}$$

where $I(i,j,t)$ = 0 is an image in the continuous domain, t is an artificial time parameter. When t=0, I is original image, as t increases, image I become more smooth. The 'c' is the diffusion constant, and ∇I is the image gradient. This linear isotropic diffusion equation is equivalent to Gaussian filtering. Perona and Malik [6] modified the classical isotropic diffusion and made it anisotropic equation given below

$$\frac{\partial I(i,j,t)}{\partial t} = div[g(\nabla I)\nabla I] \tag{3.10}$$

where $g(|\nabla I|)$ is an "edge-stopping" function. They replaced the diffusion constant 'c' with $g(|\nabla I|)$, and thus the diffusion constant depends upon the "edges" in the image. This modification makes the filter better to handle the edges. With the finite difference scheme and central differencing in spatial domain, the 2-D anisotropic diffusion equation can be expressed as

$$I_{(i,j,t+1)} = I_{(i,j,t)} + \lambda[C_N \cdot \nabla I_{N(i,j,t)} + C_S \cdot \nabla I_{S(i,j,t)} + C_E \cdot \nabla I_{E(i,j,t)} + C_W \cdot \nabla I_{W(i,j,t)}] \tag{3.11}$$

where, λ controls the rate of diffusion, and varies from 0 to 0.25. The *N*, *E*, *S*, *W* are the subscripts for *North*, *East, South*, *West* [62].

The local image gradients for North are approximated by directional differences as shown in figure 3.1, other values of directional gradients in East, South and West can be written similarly.

$$\nabla I_{N(i,j)} = I_{(i-1,j)} - I_{(i-j)} \tag{3.12}$$

and $$C_N = g(|\nabla I_N|), \tag{3.13}$$

		N		
	i-1, j-1	i-1, j	i-1, j+1	
W	i, j-1	i, j	i, j+1	E
	i+1, j-1	i+1, j	i+1, j+1	
		S		

Figure 3.1 Four Directional Gradients in a 3x3 Window

This function is chosen to satisfy $g(x) \rightarrow 0$ when $x \rightarrow \infty$ so that the diffusion is "stopped" across edges. Perona and Malik suggested two different edge stopping functions $g(x)$ in their anisotropic diffusion Eq. (3.14) and (3.15) [6].

$$g(\nabla I) = \frac{1}{1+\left\{\frac{(|\nabla I|)}{K}\right\}^2} \tag{3.14}$$

$$g(\nabla I) = e^{\left(-\frac{\nabla I}{K}\right)^2} \tag{3.15}$$

The edge stopping function in Eq. (3.14) can remove the noise in the large area efficiently, because its diffusion is in inverse proportion to gradient. On the other hand, this function can't preserve edge information. The exponent edge stopping function in Eq. (3.15) can retain edges. Yu and Acton [8] proposed a novel filtering scheme, Speckle Reduction Anisotropic Diffusion (SRAD) based on the Lee and Frost filter. In SRAD diffusion constant is presented in terms of the "instantaneous coefficient of variation" as a function of the local gradient magnitude and Laplacian operators.

(b) Fourth order PDE filter

You and Kaveh [9] proposed a class of fourth-order partial differential equations (PDEs) to optimize the balance between noise removal and edge preservation. The time evolution of PDEs tends to minimize a cost function which is an increasing function of the absolute value of the Laplacian of the image intensity. A new energy function is defined by

$$E(I) = \int f(\nabla^2 I)dxdy \tag{3.16}$$

where ∇^2 is the Laplacian operation, and $f(\cdot) \geq 0$ is an increasing function with $f'(\cdot) > 0$, so that the smoothness of the image as measured by $|\nabla^2 I|$. Therefore, the minimization of the function is equivalent to smoothing the image.

$$\frac{\partial I}{\partial t} = -\nabla^2\left[f'(|\nabla^2 I|)\frac{\nabla^2 I}{|\nabla^2 I|}\right] = -\nabla^2\left[g(|\nabla^2 I|)\nabla^2 I\right] \tag{3.17}$$

$$\text{where} \quad g(|\nabla^2 I|) = \frac{f'(\nabla^2 I)}{|\nabla^2 I|} \tag{3.18}$$

Usually the PDEs consider an image as a piecewise planar entity and therefore, simple PDE based filters have blocky effects in filtered image. However, as clear from the equations (3.17) and (3.18), PDE of the Image I becomes a fourth order PDE (*fpde*) and the gradient makes it like a ramp type function and thus avoid the blocky effect, which otherwise remain there in the processed images [70].

3.3 PROPOSED METHOD

The experimental study on existing filters (Kuan, Lee, Frost, *fpde*, *pm22* etc.) shows that for most of the synthetic images, *fpde* filter is more efficient than other standard filters like Kuan, Frost, Weiner etc. Whereas in real ultrasound images, Perona-Malik's anisotropic diffusion (*pm22*) works better than all other filters. Although both implementations are based on Non-linear PDEs but their numerical formulations are different and thus their performance is different in different image characteristics. In synthetic images edges are very sharp and clear thus the gradient easily drives the smoothing. In real ultrasound images, there are no sharp edges and thus Perona-Malik's diffusivity function remove speckle in a better way. So in a nutshell it can be concluded that PDE based filters (anisotropic diffusion '*pm22*' and '*fpde'* based filters) are more effective than other local statistics based filters in reducing speckle from ultrasound images. However, different numerical implementations of PDE method work differently under different imaging scenarios.

Thus, there is a need to address this issue of these two filters in such a way, that their edge preserving ability enhances while retaining their capability to suppress the speckle.

3.3.1 Proposed Methodology

Most of the local statistics based filters can be modeled using the Eq. 3.1, however the value of $k_{i,j}$ is different in each filter. In this study, efforts are made to modify this basic equation in such a way that edge enhancement and speckle suppression is achieved simultaneously using local statistics and Coefficient of Variance (CoV) in a moving 3x3 window. CoV is ratio of standard deviation and the weighted mean in the window. Subsequently, it filters out the speckle very near to edges also (those have been left out by most of the standard filters). Even if some low gradient edges are smoothened during this process, they are recovered back after implementing the edge map.

The spatial domain speckle suppression filters, usually perform smoothing in homogenous areas but restrict smoothing near the edges in order to preserve the image details. In the proposed filter, the main emphasis is made to smooth these 'left out' pixels near the edges by further filtering near the edges. During this process, edges may also erode and thus edge map superimposing is done. This has been achieved in two steps. In first step, *'fpde'* filter was used, and edges in the filtered image are found and saved as *edge map*. In the second step, further filtering is done on the smoothened image with more emphasis on the 'left out' pixels near the edges. Then again the saved edges are recovered from edge map. This two step approach is termed as post processing filtration, because it is used after any spatial domain speckle filter to suppress speckle and enhance edges.

Edge map is a binary image, created through edge detectors. Out of various edge detectors, a combination of Canny and Robert edge detector is used to find edge map of the filtered image (I_F). This combination gives best edge map as Robert (0.14 threshold) find straight edges and Canny (0.42 threshold) find curved ones. Threshold values in edge detectors are optimized on the basis of maximum Edge Preserving Index (EPI). After saving the Edge Map (I_{EM}), adaptive local statistics based filter is applied using 3x3 pixels mask. In this adaptive filter, weighted mean (I_{WM}) of 8 pixels depending upon their distance from the central pixel is used. Then standard deviation and CoV are found in this moving window. Since mean and variance may vary from one window to another window quickly, but CoV is always going to lie in a given range for the homogenous region, so it is taken as more robust feature. If this value varies significantly, it means that the edges are there in the window, and then smoothing is not done. So the decision to modify a pixel is based on the local statistics in the window. The new proposed filter can be used as a post processing filter or even as an independent filter, which works on the A4+C4 neighboring pixels in a 3x3 pixels window. Where A4+C4 is the combination of the adjacent four pixels (A4) and corner four pixels (C4) of 3x3 pixels window as shown in Figure 3.2.

$1/\sqrt{2}$	**1**	**$1/\sqrt{2}$**
1	**(i, j)**	**1**
$1/\sqrt{2}$	**1**	**$1/\sqrt{2}$**

Figure 3.2 A4+C4 Weighted Scheme

The A4 pixels are nearest to the central one, and thus have more weightage (1.00) than the corners of 3x3 window. This makes the corner 4 pixels (C4), $1/\sqrt{2}$ times lesser effective than the adjacent 4 pixels. A weighted mean (I_{WM}) value is computed from the 3x3 mask. The proposed filter can be seen as a modification of Eq. (3.1) in the following way:

$$F_{i,j} = I_M + CoV * (I_{i,j} - I_{WM}) \quad \text{if } |\, I_{i,j} - I_{WM} \,| < |\sigma|/2 \tag{3.20}$$

$$F_{i,j} = (I_{i,j}) \quad \text{if } |\, I_{i,j} - I_{WM} \,| \geq |\sigma|/2 \tag{3.21}$$

where $$I_{WM} = \{((I_2 + I_4 + I_6 + I_8)/4) + ((I_1 + I_3 + I_7 + I_9)/4 * \sqrt{2})\}/2 \tag{3.22}$$

I_M is the mean of all 8 pixels around the central one, 'σ' is the standard deviation of the 3x3 pixels window, I_{WM} is the weighted mean and CoV is Coefficient of Variance in the window. In simple words, the Eq. 3.20 can be termed as modification of Eq. 3.1 by two parameters. Firstly '*k*' is taken as CoV so that the filter become adaptive to the noise present in the window and secondly the $\bar{I}$ is replaced with I_{WM}, so that weightage to the nearest four pixels can be increased to do smoothing. The CoV will be more if the pixels in a 3x3 window highly differ from each other. For the present study, this difference is compared with half of the standard deviation in the 3x3 window as shown in Eq. 3.20. However this value The proposed filter checks if the difference of central pixel (the pixel to be manipulated) and the weighted mean value I_{WM} is less than half of the standard deviation of the window then replaces it with the mean value of the 3x3 window *i.e.* filtering is done. If the difference ($I_{i,j} - I_{WM}$) is more than half of the standard deviation then it may be an edge and thus does not filter that pixel as mentioned in Eq. 3.21.

3.3.2 Superimposing the Edge map

The edge map I_{EM} is a binary image, which contains white pixels for edges and black pixels elsewhere. The positions of all white pixels are measured in terms of (x, y) and their location is stored in a separate matrix 'E'. When the new filtered image I_P is achieved by proposed technique, then at all the locations stored in matrix E are taken and the gray values of these locations in I_P are replaced with pixels in image I_F at the same locations. The idea of this step is to preserve the edges because in the previous step some actual edges may also gets smoothened. The complete process of the proposed filter in post processing is represented in a pseudo code given below:

Step 1: Apply Filter to noisy image and Obtain I_F

Step 2: Calculate Edge Map I_{EM} of I_F

- Binary Image I_{EM} ← Canny and Robert Edge Detector
- Matrix E ← Location of all white pixels (edges)
- Edge Map ← (Image I_{EM}) + (Matrix E)

Step 3: In 3x3 window

- Obtain I_P ← Apply Proposed Filter on I_F
- Calculate Weighted Mean and Coefficient of Variance
- Perform filtering ← IF (Coefficient of Variance is low)

Step 4: Obtain Final Image F ← Superimpose I_{EM} on I_P

- Replace I_P by I_{EM} pixels at locations in E

Step 5: Exit

3.4 RESULTS AND DISCUSSION

3.4.1 Comparative Analysis of the Existing Methods

Several existing spatial domain filters have been studied and analyzed to evaluate their performance on synthetic and real images. The filters used in this work were, Perona Malik's anisotropic diffusion based filter '*pm22*' [6], *'fpde'* based filter [70], Kuan filter, Frost filter, Peter Kovesi's anisotropic diffusion (aniso) [71], You and Acton's filter (SRAD) [8] and 2-D Weiner filter. Wiener Filter was evaluated for different options like Weiner at 3x3 and 5x5 window. The "ground truth", images used for this work have been obtained from [35, 72] and speckle is simulated on these images, as explained chapter 2, section 2.7. Some of these images have shown in Figure 3.3. All the existing filters were evaluated on 45 test images; but the performance indices for two random images are reported in the Tables 3.1 to 3.2. It is concluded from the study that filters based on the PDEs '*pm22*' and *'fpde'* performed best for all indices. However, in some cases such as Table 3.1 the EPI of these filters is lower than other filters like '*aniso*' and Weiner filter. Therefore, '*pm22*' and *'fpde'* filters are selected for further enhancement, so that their edge preserving capability can be increased.

Table 3.1 shows evaluation of different filters for image "IMG1_7.tif", which is a noisy image with std. deviation (σ) = 0.7 generated from "IMG1.tif" using algorithm given by [52]. Table 3.2 shows evaluation of different filters for image "**IMG2_8tif**", which is a noisy image with std. deviation (σ) = 0.8 generated from "**IMG2.tif**"; an ultrasound image acquired under special conditions to minimize the speckle [52].

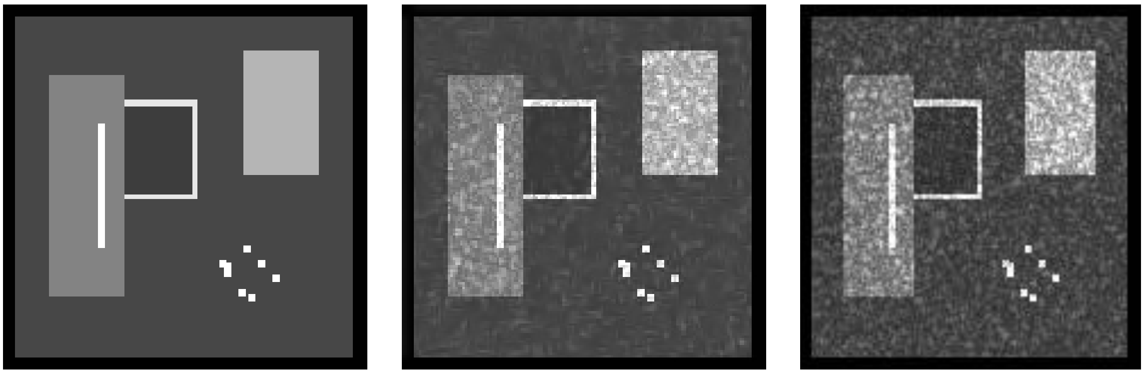

(a) IMG1 **(b) IMG1_7** **(c) IMG1_85**

Figure 3.3 (a) Noise free ground truth image (b) Noisy image after adding the speckle noise of σ= 0.7 (c) Noisy image after adding the speckle noise of σ= 0.85.

Table 3.1
Comparison for IMG1_7.tif

Image quality metrics / Filter	SNR	CoC	EPI	SSI	S_MSE
Noisy Image	17.935	0.975	0.808	0.739	14.390
pm22	21.404	0.988	0.808	0.895	17.992
Fpde	**23.200**	**0.992**	0.950	**0.918**	**19.902**
Kuan	13.866	0.957	0.114	0.779	10.721
Aniso	20.769	0.990	**0.963**	0.917	17.176
Frost	15.681	0.969	0.492	0.796	12.683
SRAD	18.418	0.979	0.831	0.775	14.792
Weiner5x5	19.155	0.986	0.897	0.890	16.583
Weiner3x3	19.994	0.985	0.961	0.844	17.188

Table 3.2
Comparison for IMG2_8.tif

Image quality metrics / Filters	SNR	CoC	EPI	SSI	S_MSE
Noisy image	10.535	0.868	0.597	0.648	8.431
pm22	**12.294**	**0.925**	0.671	**0.811**	**9.037**
Fpde	12.198	0.911	0.663	0.770	9.011
Kuan	7.745	0.849	0.128	0.751	5.235
Aniso	11.226	0.916	0.668	0.798	8.502
Frost	11.683	0.907	0.513	0.762	8.891
SRAD	12.074	0.916	0.679	0.795	9.021
Wiener5x5	11.120	0.912	0.663	0.780	7.927
Wiener3x3	12.088	0.914	**0.692**	0.781	8.914

All the performance indices are higher for pm22 in this case, except the EPI. In fact the Wiener filter (3x3) and SRAD filter has better EPI. Although the quantitative analysis has been done for 45 test images, however, tabular data of only two images is shown here. To represent the overall response of various filters on all 45 images, individual image quality metrics are shown in the Figure 3.4.

On the basis of quantitative analysis of existing filters, it is concluded that the PDEs based filters like '*fpde*' and '*pm22*' perform better than others in suppressing the speckle in ultrasound images. The main drawback of diffusing the actual edges, is addressed in the proposed filter. In subsequent discussion, the analysis has been done in comparison to these filters only.

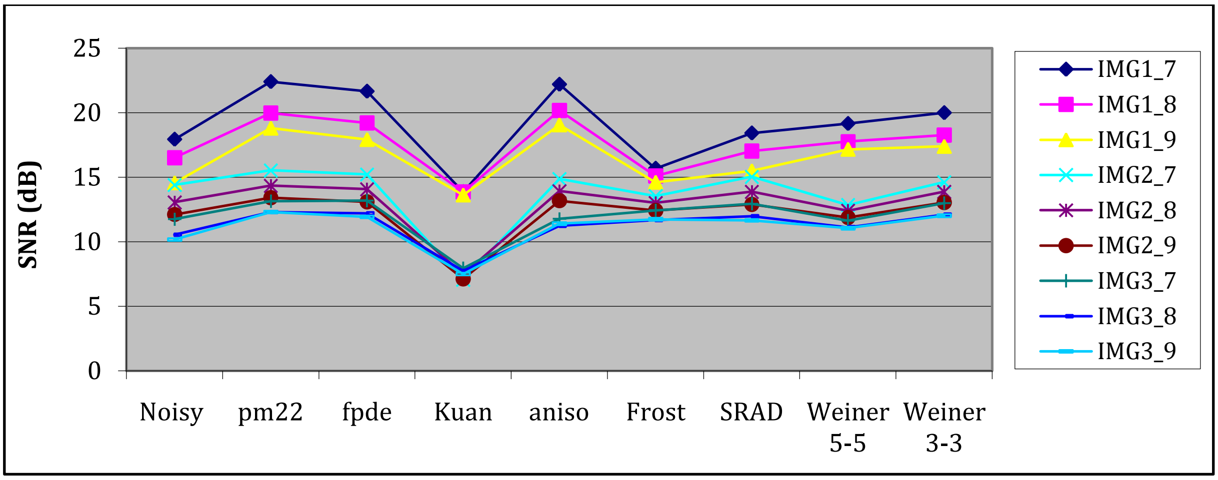

(a)

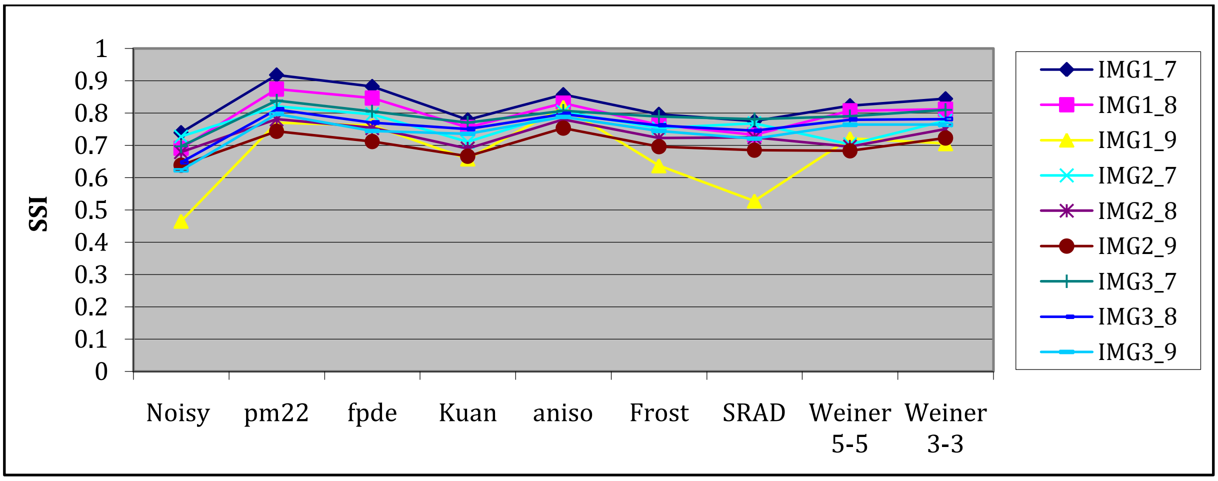

(b)

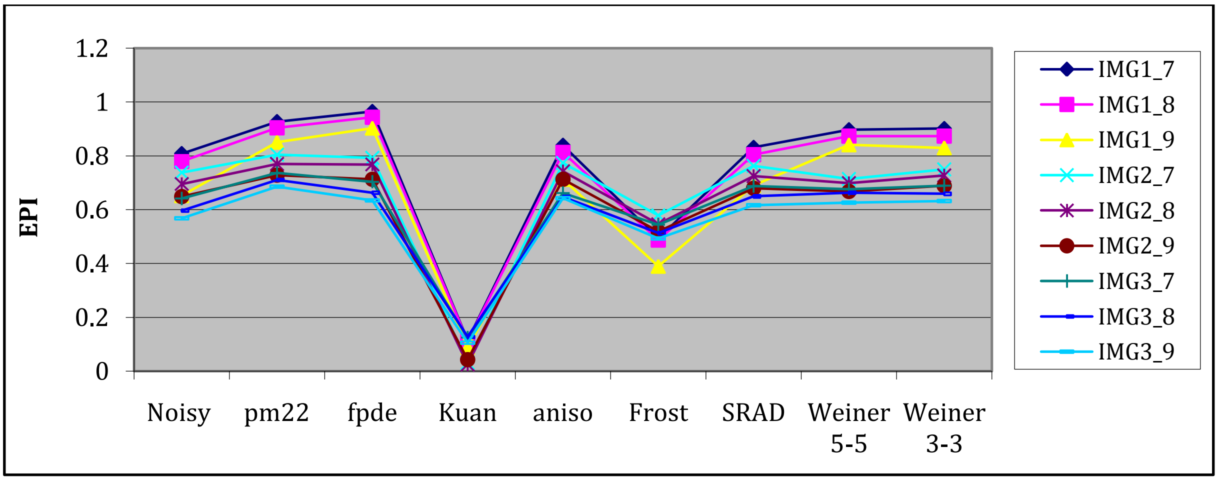

(c)

Figure 3.4 Existing Filters' Performance in Terms of Image Quality Metrics (a) SNR, (b) SSI and (c) EPI for Different Images.

3.4.2 Analysis of the Proposed Method

To analyze the performance of proposed method, different image quality metrics are used. This includes Signal-to-Noise Ratio (SNR), Correlation Coefficient (CoC), Structure Similarity Index (SSI) and Edge Preserving Index (EPI) and Signal to Mean Square Error (S_MSE) ratio. The proposed method is mainly compared with anisotropic diffusion based Perona Malik's concept (*pm22*), fourth order partial differential equation based (*fpde*) filter only. Later on visual analysis has been done by different experts to evaluate the efficacy of filters.

(a) Analysis using Image Quality Metrics

SNR

Signal to Noise Ratio is used to evaluate the ability of the proposed method to suppress the noise and keep the information during filtering process. High SNR value refers to a better filter. Table 3.3 represents the value of SNR for noisy image in first column, then after the '*fpde*' filter in second column and '*fpde*' followed by proposed filter (fpde+) in the third column. In the fourth and fifth column, the values of SNR after pm22 filter and pm22 followed by the proposed filter (pm22+) are shown. It is clear from the Table 3.3 that when proposed filter is used even after the 'fpde' filter, the values of SNR increased and this is also true for pm22 with proposed filter. This analysis shows that the proposed filter increased the efficiency of existing filters also.

S_MSE

Signal to Mean Square Error ratio is similar to SNR. High S_MSE value refers to a better filter. Table 3.4 represents the value of S_MSE for noisy image in first column, then after the '*fpde*' filter in second column and '*fpde*' followed by proposed filter (fpde+) in the third column. In the fourth and fifth column, the values of S_MSE after pm22 filter and pm22 followed by the proposed filter (pm22+) are shown. It is clear from the Table 3.4 that when proposed filter is used after the 'fpde' filter, the image gets enhanced and this is also true for pm22 with proposed filter. As evident from the Table 3.4, that S_MSE increases when proposed method is applied with existing filters.

EPI

The Edge Preserving Index is a measure of the ability of a filter, to keep the edges in an image while performing smoothening. Higher values of EPI means a better filter. Table 3.5 represents the value of EPI for noisy image, after implementing the 'fpde' filter and then 'fpde' and proposed filter, pm22 filter and finally pm22 followed by the proposed filter. It has been observed that EPI values are increased after utilizing the proposed method. This happened due to edge map technique incorporated into it.

CoC

The correlation coefficient (CoC) is a measure of correlation of pixels in filtered image and ground truth image. Higher values of CoC means a better filter. Table 3.6 represents the value of CoC for noisy image, 'fpde' filter and then 'fpde' with proposed filter, pm22 filter and finally pm22 with the proposed filter. It has been observed that CoC values are increased after utilizing the proposed method.

SSI

The Structure Similarity Index measures how of pixels in filtered image and ground truth image are similarly placed. Higher values of SSI refers to a better filter. Table 3.7 represents the values of SSI for noisy image, '*fpde*' filter and then '*fpde'* with proposed filter, *pm22* filter and finally *pm22* with the proposed filter. It has been observed that SSI values are increased after utilizing the proposed method.

Table 3.3
Results of SNR values of various test images using proposed method

IMAGE	Noisy	fpde	fpde+ Proposed	pm22	pm22+ Proposed
IMG1_1	19.104	20.370	21.239	24.686	24.714
IMG1_2	18.108	19.336	20.018	22.933	22.982
IMG1_3	17.300	18.459	19.178	21.845	21.900
IMG1_4	16.752	18.055	18.937	21.105	21.269
IMG1_5	16.121	17.489	18.344	20.248	20.494
IMG1_6	15.498	16.813	17.688	19.094	19.270
IMG1_7	14.979	16.393	17.315	18.637	18.825
IMG1_8	14.472	15.820	16.810	17.773	18.031
IMG1_9	14.028	15.354	16.466	17.195	17.603
IMG2_11	14.641	15.360	15.495	14.297	14.297
IMG2_12	13.949	14.838	14.980	13.995	13.995
IMG2_13	13.001	14.067	14.243	13.455	13.455
IMG2_14	12.537	13.736	13.951	13.403	13.403
IMG2_15	11.774	13.111	13.354	12.826	12.826
IMG2_16	11.280	12.898	13.201	12.934	12.937
IMG2_17	10.693	12.436	12.811	12.537	12.541
IMG2_18	10.039	11.707	12.046	12.004	12.011
IMG2_19	9.758	11.605	12.049	12.122	12.127
IMG3_21	17.457	17.809	18.024	17.811	17.829
IMG3_22	16.407	16.919	17.135	17.011	17.042
IMG3_23	15.783	16.387	16.643	16.483	16.520
IMG3_24	15.059	15.841	16.085	16.026	16.064

Cont.

Table 3.3

IMAGE	Noisy	fpde	fpde+ Proposed	pm22	pm22+ Proposed
IMG3_25	14.546	15.449	15.744	15.810	15.881
IMG3_26	13.675	14.558	14.902	14.821	14.924
IMG3_27	13.104	14.088	14.505	14.444	14.563
IMG3_28	12.818	13.847	14.207	14.133	14.261
IMG3_29	12.302	13.291	13.699	13.615	13.731
IMG4_31	11.652	13.762	14.368	14.594	14.607
IMG4_32	10.887	12.949	13.596	13.942	13.952
IMG4_33	10.007	12.097	12.835	13.192	13.214
IMG4_34	9.450	11.541	12.371	12.746	12.778
IMG4_35	8.719	10.719	11.547	11.889	11.937
IMG4_36	8.156	10.109	11.004	11.314	11.386
IMG4_37	7.532	9.420	10.349	10.537	10.653
IMG4_38	7.052	8.871	9.833	9.954	10.096
IMG4_39	6.549	8.322	9.256	9.303	9.474
IMG5_41	6.594	9.510	10.347	11.414	11.429
IMG5_42	5.696	8.483	9.380	10.683	10.699
IMG5_43	4.933	7.706	8.704	10.079	10.098
IMG5_44	4.228	6.764	7.697	8.919	8.933
IMG5_45	3.644	6.198	7.253	8.517	8.535
IMG5_46	2.917	5.326	6.391	7.471	7.502
IMG5_47	2.421	4.763	5.866	6.831	6.880
IMG5_48	1.942	4.185	5.312	6.158	6.240
IMG5_49	1.484	3.614	4.763	5.458	5.551

Table 3.4
Results of S_MSE values of various test images using proposed method

IMAGE	Noisy	fpde	fpde+ Proposed	pm22	pm22+ Proposed
IMG1_1	8.427	10.237	11.155	13.568	13.598
IMG1_2	7.823	9.676	10.583	12.365	12.421
IMG1_3	7.313	9.295	10.297	11.848	11.907
IMG1_4	6.957	8.911	9.941	11.435	11.544
IMG1_5	6.566	8.368	9.272	10.568	10.667
IMG1_6	6.245	8.032	8.974	9.988	10.089
IMG1_7	5.923	7.609	8.578	9.573	9.687
IMG1_8	5.786	7.346	8.386	9.271	9.403
IMG1_9	5.564	7.024	8.055	8.839	8.973
IMG2_11	10.347	11.861	12.157	11.301	11.302
IMG2_12	9.617	11.334	11.657	11.000	11.001
IMG2_13	8.892	10.849	11.234	10.814	10.815
IMG2_14	8.418	10.440	10.893	10.643	10.644
IMG2_15	7.947	9.956	10.444	10.359	10.360
IMG2_16	7.476	9.505	10.055	10.160	10.168
IMG2_17	7.219	9.202	9.869	9.979	9.986
IMG2_18	6.784	8.693	9.332	9.643	9.658
IMG2_19	6.609	8.553	9.284	9.557	9.569
IMG3_21	7.758	8.840	9.161	8.785	8.805
IMG3_22	7.146	8.267	8.602	8.367	8.377
IMG3_23	6.735	7.906	8.248	8.070	8.089
IMG3_24	6.469	7.603	8.049	7.934	7.958

Cont.

Table 3.4

IMAGE	Noisy	fpde	fpde+ Proposed	pm22	pm22+ Proposed
IMG3_25	6.123	7.264	7.768	7.732	7.761
IMG3_26	5.797	6.842	7.363	7.308	7.336
IMG3_27	5.569	6.543	7.103	7.015	7.065
IMG3_28	5.415	6.334	6.866	6.818	6.860
IMG3_29	5.302	6.167	6.743	6.624	6.683
IMG4_31	6.100	7.739	8.544	8.621	8.641
IMG4_32	5.721	7.155	7.981	8.015	8.035
IMG4_33	5.386	6.603	7.453	7.365	7.402
IMG4_34	5.145	6.256	7.122	6.927	6.984
IMG4_35	4.910	5.869	6.691	6.381	6.452
IMG4_36	4.714	5.549	6.358	5.906	5.996
IMG4_37	4.534	5.259	6.038	5.486	5.608
IMG4_38	4.427	5.083	5.831	5.196	5.332
IMG4_39	4.318	4.917	5.625	4.961	5.109
IMG5_41	6.439	9.048	11.807	11.306	11.328
IMG5_42	5.950	8.155	10.681	10.419	10.443
IMG5_43	5.625	7.498	9.855	9.690	9.718
IMG5_44	5.297	6.861	8.955	8.661	8.685
IMG5_45	5.057	6.420	8.497	7.973	8.004
IMG5_46	4.832	5.937	7.932	7.069	7.123
IMG5_47	4.671	5.662	6.625	6.486	6.552
IMG5_48	4.574	5.467	6.418	6.037	6.147
IMG5_49	4.406	5.159	6.016	5.422	5.528

Table 3.5
Results of EPI values of various test images using proposed method

IMAGE	Noisy	fpde	fpde+ Proposed	pm22	pm22+ Proposed
IMG1_1	0.833	0.890	0.905	0.977	0.977
IMG1_2	0.798	0.861	0.879	0.965	0.965
IMG1_3	0.765	0.826	0.847	0.947	0.948
IMG1_4	0.737	0.803	0.827	0.926	0.939
IMG1_5	0.717	0.782	0.808	0.913	0.928
IMG1_6	0.691	0.756	0.783	0.887	0.901
IMG1_7	0.673	0.738	0.765	0.865	0.881
IMG1_8	0.639	0.701	0.734	0.842	0.860
IMG1_9	0.627	0.686	0.719	0.809	0.830
IMG2_11	0.768	0.809	0.822	0.800	0.809
IMG2_12	0.741	0.752	0.793	0.778	0.787
IMG2_13	0.700	0.723	0.761	0.763	0.772
IMG2_14	0.669	0.699	0.732	0.757	0.765
IMG2_15	0.643	0.677	0.709	0.732	0.741
IMG2_16	0.618	0.670	0.686	0.727	0.734
IMG2_17	0.609	0.635	0.676	0.721	0.728
IMG2_18	0.572	0.625	0.637	0.694	0.704
IMG2_19	0.564	0.610	0.630	0.688	0.695
IMG3_21	0.847	0.840	0.875	0.877	0.880
IMG3_22	0.822	0.819	0.854	0.863	0.878
IMG3_23	0.795	0.805	0.834	0.846	0.857
IMG3_24	0.781	0.809	0.820	0.837	0.856

Cont.

Table 3.5

IMAGE	Noisy	fpde	fpde+ Proposed	pm22	pm22+ Proposed
IMG3_25	0.739	0.768	0.780	0.808	0.812
IMG3_26	0.719	0.752	0.763	0.788	0.790
IMG3_27	0.697	0.729	0.740	0.770	0.771
IMG3_28	0.677	0.710	0.719	0.747	0.751
IMG3_29	0.640	0.68	0.684	0.715	0.724
IMG4_31	0.627	0.598	0.656	0.647	0.657
IMG4_32	0.595	0.573	0.625	0.621	0.629
IMG4_33	0.563	0.540	0.591	0.595	0.604
IMG4_34	0.533	0.515	0.560	0.564	0.573
IMG4_35	0.499	0.482	0.526	0.532	0.54
IMG4_36	0.469	0.46	0.494	0.503	0.509
IMG4_37	0.450	0.438	0.472	0.483	0.486
IMG4_38	0.426	0.417	0.449	0.451	0.456
IMG4_39	0.397	0.387	0.416	0.423	0.426
IMG5_41	0.518	0.646	0.669	0.828	0.837
IMG5_42	0.481	0.602	0.625	0.790	0.800
IMG5_43	0.447	0.558	0.586	0.750	0.760
IMG5_44	0.413	0.512	0.536	0.699	0.710
IMG5_45	0.394	0.485	0.508	0.651	0.661
IMG5_46	0.358	0.439	0.463	0.596	0.608
IMG5_47	0.341	0.415	0.438	0.551	0.565
IMG5_48	0.322	0.390	0.409	0.514	0.529
IMG5_49	0.314	0.375	0.394	0.480	0.495

Table 3.6
Results of CoC values of various test images using proposed method

IMAGE	Noisy	fpde	fpde+ Proposed	pm22	pm22+ Proposed
IMG1_1	0.981	0.988	0.990	0.995	0.995
IMG1_2	0.976	0.985	0.987	0.993	0.993
IMG1_3	0.972	0.982	0.983	0.991	0.991
IMG1_4	0.968	0.979	0.981	0.988	0.989
IMG1_5	0.964	0.976	0.979	0.987	0.987
IMG1_6	0.957	0.971	0.974	0.981	0.982
IMG1_7	0.952	0.968	0.971	0.979	0.979
IMG1_8	0.948	0.965	0.969	0.977	0.977
IMG1_9	0.941	0.959	0.964	0.971	0.972
IMG2_11	0.943	0.959	0.962	0.958	0.958
IMG2_12	0.931	0.951	0.953	0.950	0.951
IMG2_13	0.918	0.942	0.944	0.944	0.945
IMG2_14	0.907	0.936	0.937	0.941	0.944
IMG2_15	0.894	0.928	0.929	0.934	0.934
IMG2_16	0.881	0.919	0.920	0.929	0.931
IMG2_17	0.873	0.913	0.915	0.923	0.924
IMG2_18	0.853	0.898	0.901	0.913	0.914
IMG2_19	0.848	0.895	0.898	0.909	0.911
IMG3_21	0.972	0.979	0.981	0.980	0.982
IMG3_22	0.964	0.973	0.974	0.975	0.976
IMG3_23	0.959	0.970	0.971	0.972	0.973
IMG3_24	0.953	0.966	0.967	0.968	0.969

Cont.

Table 3.6

IMAGE	Noisy	fpde	fpde+ Proposed	pm22	pm22+ Proposed
IMG3_25	0.945	0.960	0.961	0.963	0.964
IMG3_26	0.936	0.953	0.954	0.956	0.958
IMG3_27	0.927	0.946	0.947	0.950	0.952
IMG3_28	0.920	0.939	0.940	0.944	0.946
IMG3_29	0.914	0.935	0.937	0.940	0.946
IMG4_31	0.889	0.927	0.928	0.937	0.939
IMG4_32	0.871	0.912	0.914	0.924	0.924
IMG4_33	0.849	0.895	0.897	0.909	0.910
IMG4_34	0.833	0.882	0.886	0.897	0.899
IMG4_35	0.812	0.863	0.869	0.878	0.879
IMG4_36	0.791	0.845	0.853	0.860	0.862
IMG4_37	0.771	0.825	0.834	0.838	0.840
IMG4_38	0.750	0.806	0.817	0.818	0.819
IMG4_39	0.735	0.791	0.803	0.802	0.804
IMG5_41	0.729	0.817	0.826	0.868	0.870
IMG5_42	0.690	0.781	0.792	0.836	0.838
IMG5_43	0.668	0.758	0.771	0.814	0.816
IMG5_44	0.629	0.717	0.730	0.771	0.773
IMG5_45	0.609	0.694	0.710	0.743	0.743
IMG5_46	0.579	0.661	0.678	0.706	0.707
IMG5_47	0.562	0.641	0.659	0.682	0.683
IMG5_48	0.526	0.603	0.621	0.640	0.642
IMG5_49	0.519	0.588	0.608	0.620	0.622

Table 3.7
Results of SSI values of various test images using proposed method

IMAGE	Noisy	fpde	fpde+ Proposed	pm22	pm22+ Proposed
IMG1_1	0.643	0.818	0.838	0.923	0.945
IMG1_2	0.608	0.785	0.807	0.904	0.927
IMG1_3	0.579	0.752	0.779	0.883	0.906
IMG1_4	0.554	0.726	0.754	0.863	0.887
IMG1_5	0.528	0.693	0.720	0.839	0.863
IMG1_6	0.503	0.660	0.690	0.807	0.831
IMG1_7	0.479	0.630	0.661	0.782	0.806
IMG1_8	0.465	0.606	0.640	0.763	0.787
IMG1_9	0.448	0.585	0.619	0.742	0.766
IMG2_11	0.813	0.882	0.885	0.871	0.893
IMG2_12	0.779	0.862	0.869	0.858	0.879
IMG2_13	0.754	0.849	0.859	0.854	0.876
IMG2_14	0.721	0.823	0.826	0.841	0.862
IMG2_15	0.698	0.808	0.809	0.832	0.854
IMG2_16	0.671	0.785	0.789	0.820	0.841
IMG2_17	0.650	0.772	0.778	0.816	0.838
IMG2_18	0.619	0.743	0.751	0.798	0.820
IMG2_19	0.601	0.729	0.739	0.787	0.809
IMG3_21	0.827	0.873	0.887	0.874	0.894
IMG3_22	0.796	0.850	0.864	0.857	0.877
IMG3_23	0.777	0.838	0.857	0.848	0.867
IMG3_24	0.751	0.818	0.823	0.838	0.856

Cont.

Table 3.7

IMAGE	Noisy	fpde	fpde+ Proposed	pm22	pm22+ Prposed
IMG3_25	0.730	0.800	0.818	0.826	0.846
IMG3_26	0.697	0.769	0.794	0.794	0.813
IMG3_27	0.682	0.757	0.768	0.788	0.807
IMG3_28	0.658	0.733	0.735	0.758	0.779
IMG3_29	0.645	0.720	0.732	0.746	0.767
IMG4_31	0.557	0.648	0.653	0.656	0.669
IMG4_32	0.521	0.612	0.623	0.627	0.640
IMG4_33	0.482	0.573	0.577	0.595	0.607
IMG4_34	0.449	0.538	0.553	0.562	0.576
IMG4_35	0.419	0.504	0.514	0.529	0.542
IMG4_36	0.389	0.470	0.477	0.495	0.509
IMG4_37	0.363	0.438	0.445	0.461	0.478
IMG4_38	0.344	0.416	0.426	0.437	0.453
IMG4_39	0.318	0.384	0.395	0.403	0.421
IMG5_41	0.433	0.617	0.646	0.772	0.795
IMG5_42	0.392	0.563	0.596	0.723	0.745
IMG5_43	0.361	0.519	0.552	0.676	0.699
IMG5_44	0.330	0.468	0.499	0.606	0.629
IMG5_45	0.303	0.429	0.461	0.558	0.581
IMG5_46	0.277	0.390	0.421	0.497	0.521
IMG5_47	0.260	0.363	0.392	0.458	0.482
IMG5_48	0.245	0.338	0.367	0.420	0.446
IMG5_49	0.230	0.312	0.338	0.376	0.401

(b) Analysis by Visual Evaluation

As explained earlier, edge map of the image plays significant role in the proposed speckle suppression method. Figure 3.5 shows the test images and their edge maps. After storing the edge map of an image, the filtering technique is applied and then the edge map is superimposed to achieve final image. More precisely, the performance of the post processing filtration technique can be visually evaluated from Figure 3.6. This figure explains the importance of edge map by zooming out a small portion of image “IMG1_8.tif” (Figure 3.5c) used for testing.

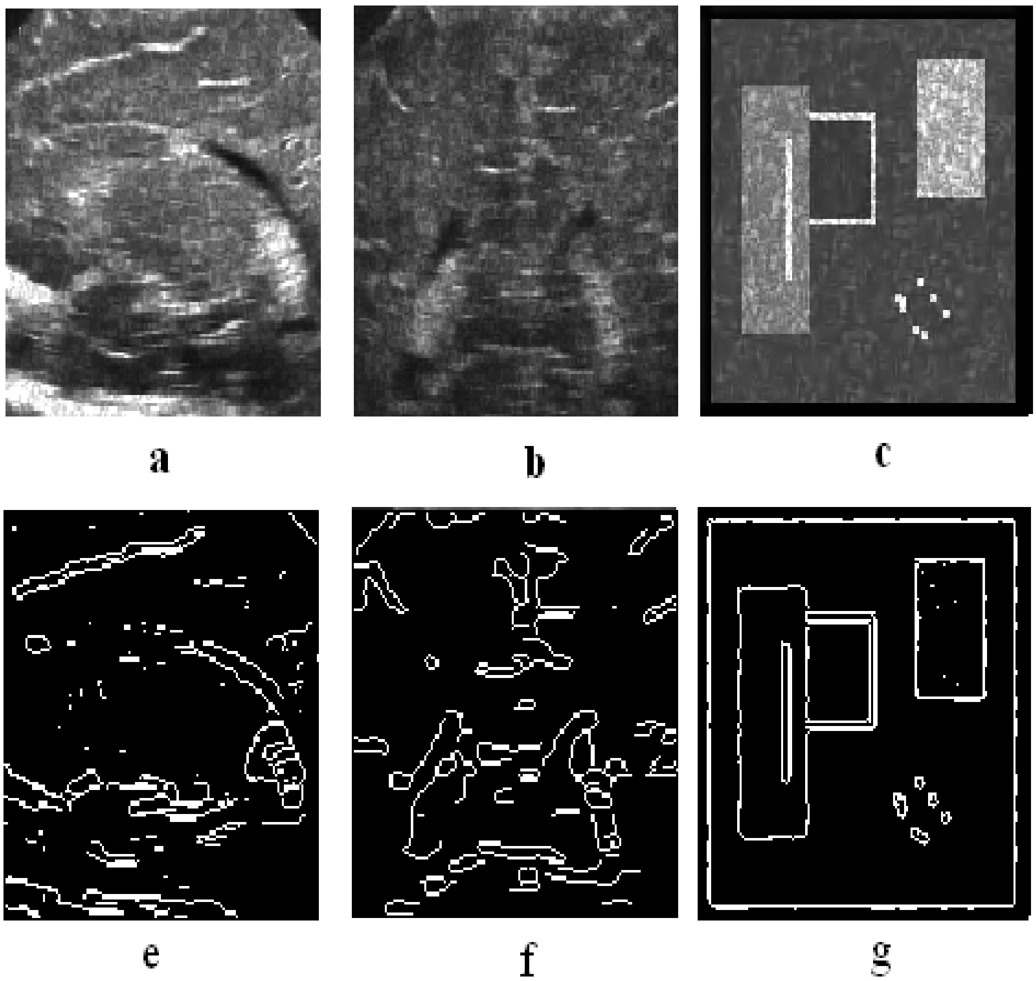

Figure 3.5 Test images (a) IMG3 (b) IMG2 (c) IMG1 and their edge-maps (e) edge map of IMG3 (f) edge map of IMG2 (g) edge map of IMG1

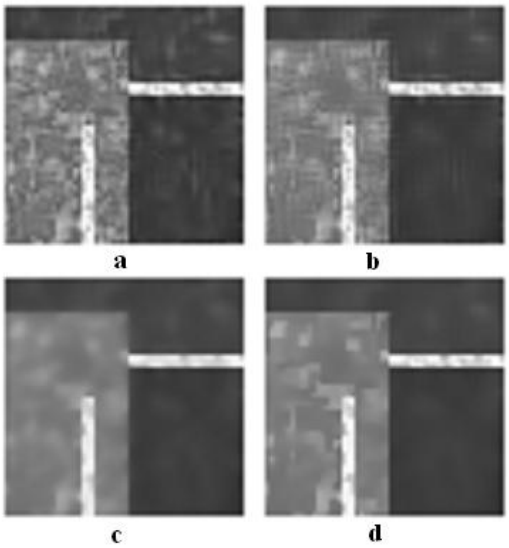

Figure 3.6 Comparison of proposed filter with *fpde* filter

Figure 3.6a is the noisy image on which a standard filter '*fpde'* is used. The output filtered image using '*fpde*' is presented in Figure 3.6b. Figure 3.6c is the result of post-processing filter after '*fpde*' without implementing the edge map. It is visually clear by comparing the Figure 3.6b and 3.6c, that the later image is smoother than the first one. This is due to the fact that the proposed method removes the speckle even very near to the edges. However some edges are also get smoothed during this process. Figure 3.6d is the final image after superimposing the edge map on the Figure 3.6c. It is evident from Figure 3.6d, that the proposed method suppresses the speckle as well as enhances the edges. Results show that in most of the cases the proposed technique enhances the edges and remove speckle simultaneously better than the previous reported filters.

(c) Analysis using Image Profile

To show the improvement in image after using the proposed method, image profile tool is used in different images. Image profile gives an idea about the pixel value along an axis of an image. To get image profile, a reference line is taken on the image and the pixel values are plotted along the line. In Figure 3.7 a reference line is shown to earmark the points across which the profile is plotted in Figure 3.8. There are four image profiles corresponding to Original, Noisy, Image after filtering with a Standard filter (*fpde* in this case) and the image after post processing (*fpde*+proposed) filter. As marked in the Figure 3.7, after proposed filter the false edges are removed (due to weighted mean filtering) and the actual edges are recovered due to Edge map technique. Thus the proposed filter works as low pass filter in homogenous area and as Adaptive filter near the edges.

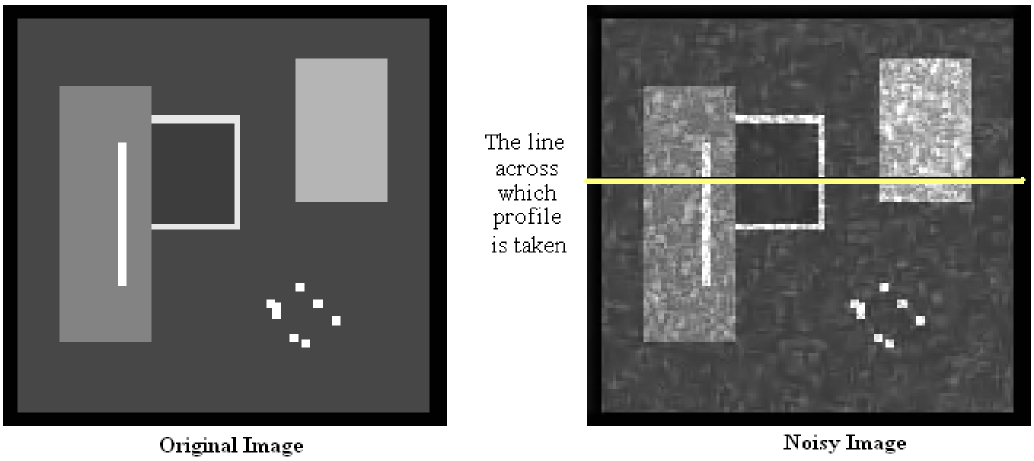

Figure 3.7 Image profile taken across a line from original and noisy image

(d) Visual Evaluation by the Experts on the Real Ultrasound Images

The above said proposed filter is also tested for fifty real ultrasound images like shown in Figure 3.9. Since these images are already affected by speckle noise, and thus their "ground truth" images are not available. So to evaluate the proposed filter on these images, a subjective method is adopted. In this method, a group of three radiologists were asked to rate the efficacy of each filter and for better visualization of desired information in each image. The images shown in the Figure 3.9a to 3.9c have been obtained from the [72] and the images in the Figure 3.9d to 3.9f have been taken from the second database as discussed in chapter2, section 2.7.

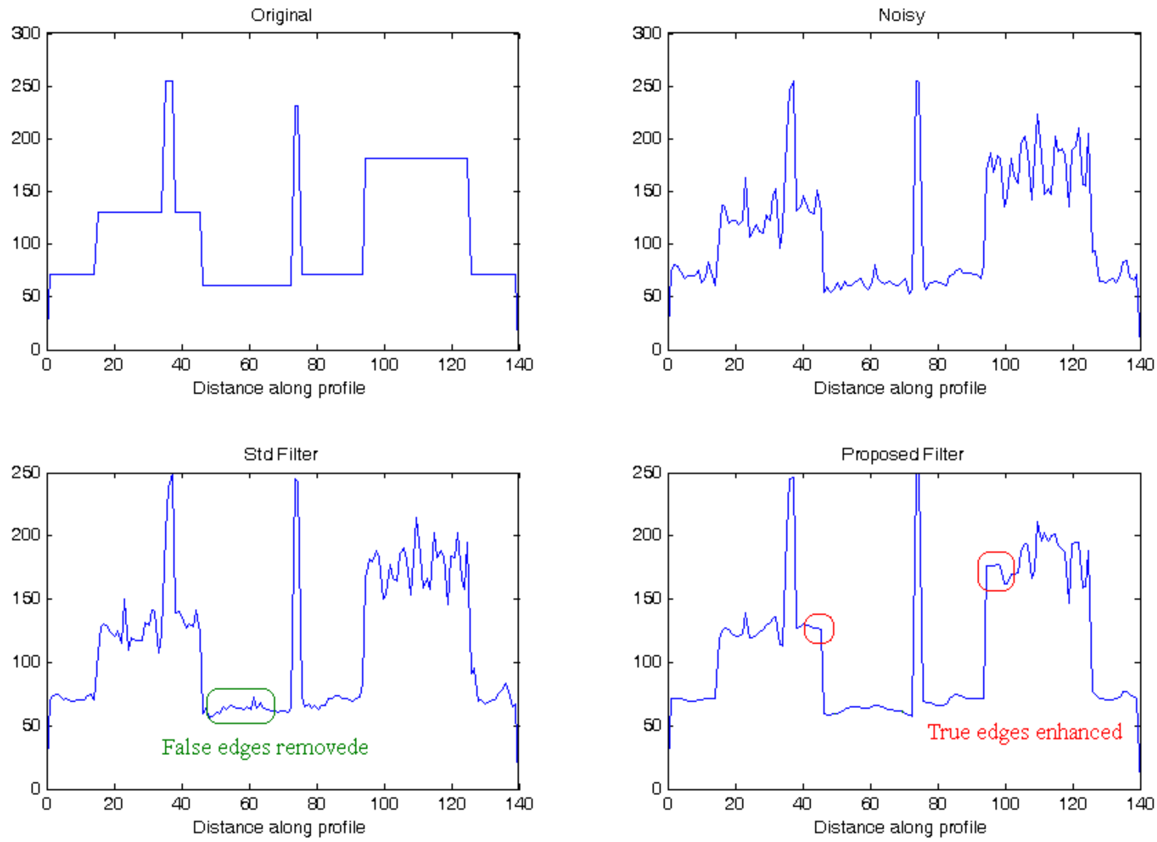

Figure 3.8 Image profile of a) Original image b) Noisy image c) After filtering by fpde filter d) After using the proposed method

In the Figure 3.10, visual comparison has been shown for a real ultrasound image. Figure 3.10a shows original image and Figure 3.10b shows the filtered version of test image UST1 after using '*fpde*' filter. This image is further treated with proposed technique and output is shown in figure 3.10c. On visual comparison of these two images in Figure 3.10b and 3.10c, it could be established that after implementing the proposed technique on '*fpde*' image, the visual quality is enhanced and even edges are also enhanced. Similar observations are made for other images in case of 'pm22' filter in Figure 3.10d and further processed with proposed filter in Figure 3.10e. The Figure 3.10f is the filtered version of Figure 3.9a using only proposed filter. It is observed that fine details are preserved if the proposed filter is used alone on the ultrasound images.

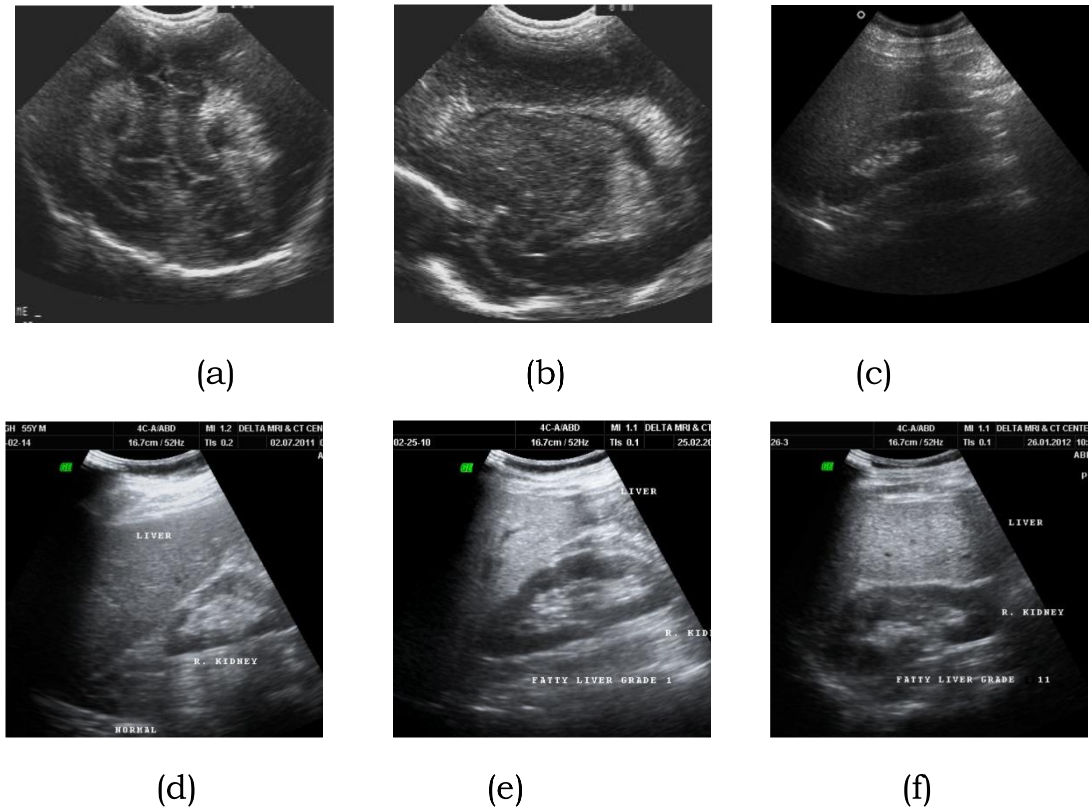

Figure 3.9 Real ultrasound images used for visual comparison (a) UST1 (b) UST2 (c) UST3 (d) UST4 (e) UST5 (f) UST6

All the images were visually evaluated by the radiology experts before and after speckle filters. For each case, the original and despeckled images were presented without labeling at random to the experts. The experts were asked to assign a score in the 1–5 scale corresponding to low and high subjective visual perception criteria. Five is given to an image with the best visual perception. The experts were free to give equal scores to more than one image in each case. In the end, sum of scores given to each image is calculated for all the filters. Further, Mean Opinion Score (MOS) is calculated for each filter and reported in Table 3.8. The MOS out of 5, was provided for each image by the experts after visual examination [54].

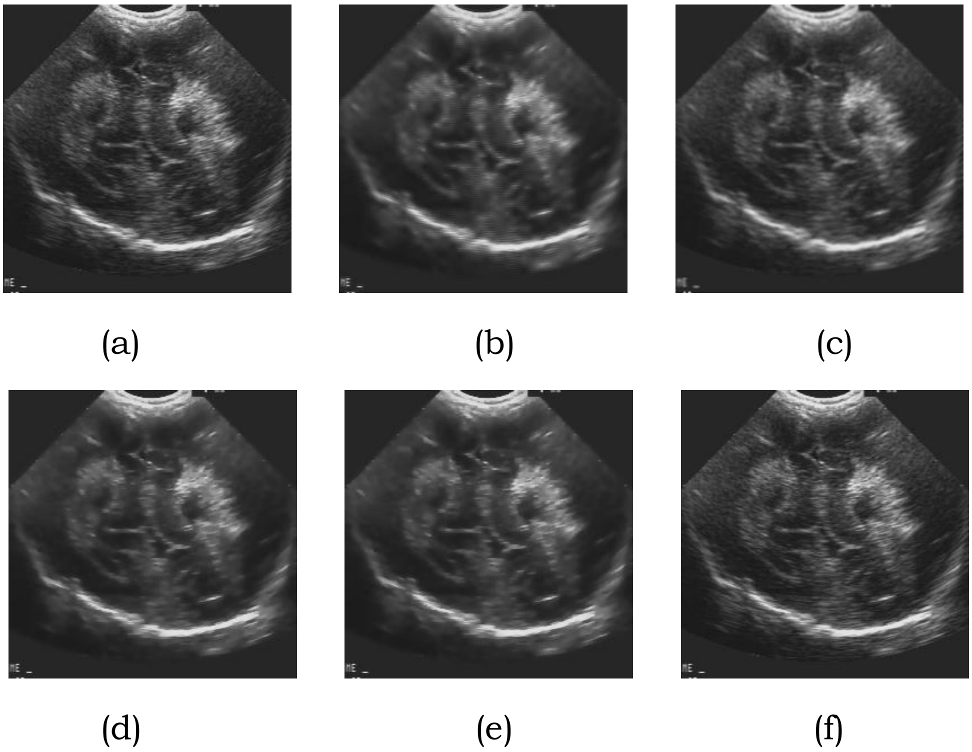

Figure 3.10 Real ultrasound imageUST1, with and without proposed technique.(a) UST1 (b) UST1-fpde (c) UST1 - pm22 (d) UST1-proposed (e) UST1- fpde + proposed (f) UST1 – pm22 proposed

The score is based on the information content in the image and the easiness to the experts in identifying the different regions or anatomical structures in the ultrasound images. Radiologists were asked pay more emphasis on tissue related information available for further analysis while scoring the different images. Although the study has been done for fifty real ultrasound images, however, the Table 3.8 represents the MOS of only five images.

To represent the complete information of the study for MOS, average value of each filter is calculated for fifty images and reported in Table 3.9. Different filters are ranked based on their MOS. Filter with higher MOS has the maximum acceptability to the radiologists and filter with lower MOS has the least acceptability.

Table 3.8
Visual evaluation score for standard filters and after proposed technique for real ultrasound images.

IMAGE	Filter	Expert1	Expert2	Expert3	MOS
UST1	fpde	3	4	3	3.333
	fpde+	4	4	4	4.000
	pm22	2	2	3	2.333
	pm22+	3	2	3	2.667
	proposed	5	4	4	4.333
UST2	fpde	3	3	3	3.000
	fpde+	4	3	4	3.667
	pm22	2	2	3	2.333
	pm22+	3	3	3	3.000
	proposed	4	4	4	4.000
UST3	fpde	3	4	3	3.333
	fpde+	4	4	4	4.000
	pm22	2	2	3	2.333
	pm22+	3	2	3	2.667
	proposed	4	4	4	4.000
UST4	fpde	3	4	3	3.333
	fpde+	4	4	4	4.000
	pm22	4	2	3	3.000
	pm22+	4	3	4	3.667
	proposed	5	4	5	4.667
UST5	fpde	3	3	4	3.333
	fpde+	4	4	4	4.000
	pm22	3	2	3	2.667
	pm22+	4	3	4	3.667
	proposed	5	4	4	4.333

Table 3.9
Average value of MOS for different filters

Filter	fpde	fpde+proposed	pm22	pm22+proposed	Proposed only
MOS	3.464	4.034	2.533	3.134	4.267

It is clear from the Table 3.9, that '*fpde+proposed*' filter (*fpde+*) performs better than '*pm22*' in the real Ultrasound images. However, in contrary to Quality metrics evaluation, the individual proposed filter outperforms all the filters. Anisotropic diffusion based filters have not been accepted by the radiologists due to over smoothing effect in most of the images. This over smoothing can however be controlled by decreasing the number of iterations, but even then it does perform as good as the proposed filter. Perona-Malik's method (*pm22*) not performed as expected, because it produced some blocky effects while smoothing in non homogenous areas. More importantly, the proposed technique enhances the efficiency of each filter after which it is used along with a standard filter, and interestingly radiologists rated it highest when it was used alone. Therefore a conclusion can be drawn that the proposed filter is able to enhance the efficiency of the existing PDE based filters as well as it is able to enhance the ultrasound images. Another observation is that the radiologists/physicians are accustomed to speckle for visual diagnosis of the ultrasound images, and they termed 'blurred image' to any image with smooth appearance (filtered version). The conventional filters do the over smoothing of ultrasound images and thus tissue related significant information may be lost. Further, from the MOS analysis and discussions with the radiologists, it was concluded that for ultrasound images filtered with '*pm22+prposed filter*' are good for automatic segmentation whereas for texture analysis based tissue characterization, only the proposed filter should be used to preprocess the image.

3.5 SUMMARY

In this chapter, a new spatial domain filtering technique is proposed, based on edge map and local statistics. The proposed method when used in combination to any standard speckle filter (like Kuan, Frost, FPDE, Anisotropic diffusion etc.) enhances the efficacy of the respective filter. This method addresses the problem of speckle inhibition near the edges through edge map. This technique utilizes the local statistics in a moving window, to smooth or preserve the central pixel. A combination of 'coefficient of variance' and 'weighted mean' is included for better adaptation of the filter to check the true edges and isolated speckle noise in homogenous area. In the later stage 'Edge map' is used to enhance the edges in the image after filtration. Evaluation of the proposed filter has been done quantitatively using image quality metrics and qualitatively by medical experts also. The results of the study highlight that the proposed technique enhances the efficiency of standard spatial filters for ultrasound images both in terms of speckle suppression and enhancement of edges. The visual analysis followed by the radiologists' mean opinion score indicates that the proposed method is suitable for computer aided analysis of ultrasound images, as it preserves the diagnostically significant information in the image.

CHAPTER-4

TEXTURE FEATURES AND INVESTIGATIONS ON ROI SELECTION

4.1 INTRODUCTION

After speckle reduction from the ultrasound images, texture features were extracted from a Region of Interest (ROI). An ROI is a sub part of the image, which contains the vital information related to the diagnosis. Since an ROI is used as 'representative' of the image, and all further computations and diagnosis depends upon the ROI, therefore, it is very crucial to select an appropriate image area as ROI. Further, the use of an ROI will reduce the computational time to extract the features from sub part rather than from the whole liver image. This chapter investigates the importance of location, shape and size of the ROI for liver tissue characterization.

The impact of ROI has been analyzed through texture features extracted from that ROI, therefore, significance and background of the various texture models is discussed in this chapter, and subsequently the experimental analysis for selection of ROI is presented.

4.2 TEXTURE MODELS

Texture is complex visual pattern composed of entities that have characteristic brightness, colour, slope, size, etc. Thus texture can be regarded as a similarity grouping in an image [74]. Russ has defined the 'texture' as a descriptor of local brightness variation from pixel to pixel in a small neighbourhood in an image [75]. Alternatively, texture can be described as an attribute representing the spatial arrangement of the grey levels of the pixels in a region of a digital image. Texture analysis has played an important role in many areas including medical imaging, remote sensing and industrial inspection, and is mainly used for classification, segmentation, and synthesis [76, 77]. Texture models are usually classified into four classes; *structural, statistical, model-based* and *transform methods.*

4.2.1 Structural Texture Model

Structural texture analysis techniques describe a texture as the composition of well-defined texture elements (primitives) such as regularly spaced parallel lines [78, 79]. To describe the texture, the primitives and the placement rules must be defined. The advantage of the structural approach is that it provides a good symbolic description of the image [80]. However, these methods appear to be limited in practicality since they can only describe regular textures [81].

4.2.2 Statistical Texture Model

Statistical texture analysis techniques describe texture of regions in an image through higher-order moments of their grayscale histograms [82]. The statistical approaches represent the non-deterministic properties that govern the relationships between the grey levels of an image. The textures in grey-level images are discriminated spontaneously only if they differ in second order moments. The most popular second-order statistical features for texture analysis are derived from the Spatial Gray Level co-occurrence Matrix (SGLCM) [83] Similarly the Grey Level Run Length Matrix (GLRLM) utilizes higher-order statistics of the gray level histogram. This approach characterizes coarse textures as having many pixels in a constant gray level run and fine textures as having few pixels in gray level run length [79].

4.2.3 Model based Textures

Model based texture analysis uses an empirical model describe the inter-pixel relationship based on a weighted average of the pixel intensities in its neighborhood. The estimated parameters of the image models are used as textural feature descriptors. Markov Random Fields (MRF) and fractal models are some of its examples. Fractal and stochastic models attempt to interpret an image texture by use of generative image model and stochastic model respectively [84-86]. The fractal model has been shown to be useful for modeling some natural textures.

4.2.4 Transform based Texture Model

Transform methods of texture analysis, such as Fourier model [74] Gabor [87] and Wavelet transforms represent an image in a space whose co-ordinate system has an interpretation that is closely related to the characteristics of a texture (such as frequency) [88, 89]. In other words, they convert the image into a new form using the spatial frequency properties of the pixel intensity variations. Features derived from a set of Gabor filters have been widely used in texture analysis for image segmentation [90]. Wavelet transform methods of feature extraction have been used to characterize texture and to treat the problems of liver classification through texture analysis [32, 91, 92].

4.3 TEXTURE FEATURES FOR FATTY LIVER CHARACTERIZATION

Fatty liver is a condition, when the fat content of the '*hepatocytes*' increases, resulting in variation of the texture of liver surface. The granular structure of the tissue or an area can be studied and analyzed to characterize it. The specific granular pattern of normal liver and fatty liver can be described as texture and thus for tissue characterization, texture analysis may provide vital information that may not be obtained through visual interpretation of ultrasound images. Considering this idea as motivation, many texture models have been studied and analyzed so that a better classification method could be designed using optimal features.

To classify the liver tissue (normal and abnormal) from an ultrasound image, many feature models have been proposed in the last few years [2, 22]. However, the SGLCM by Haralick [18], the Fourier Power Spectrum (FPS) by Landeris [17], and the Texture Energy Measures (TEM) proposed by Laws [19] are the most commonly used texture feature models; those have been applied successfully to real-world textures also. The Statistical Feature Matrix (SFM) texture model is also useful to describe surface textures [22]. Grey Level Difference Statistics (GLDS) is proposed by Weszka and Dyer for terrain classification based on texture analysis [23]. The fractal-based features proposed by Mandelbrot are able to explain the roughness of natural surfaces. Wu and others used all the above four texture models for liver characterization, and proposed a new concept based on the multi-resolution fractal dimensions also called Fractal Features (FF) [24]. Thijssen and his team proved the significance of SGLCM parameters in characterizing the ultrasound images [93]. Different texture models considered for analysis of ultrasound imaging are given in the following section.

4.3.1. SGLCM Features

The SGLCM based features, as proposed by Haralick et al. are the most frequently used texture features [18]. The SGLCM is a matrix, where the number of rows and columns is equal to the number of quantized gray levels, N_g, in the image. Co-occurrence matrices describe how often one gray level will appear in a specified spatial relationship to another gray-level in the image. Spatial relationship is a function of angular relationship $\boldsymbol{\theta}$ and the distance ($\boldsymbol{d}$) between the neighboring pixels (resolution cells). If N_g are the number of quantized gray levels in an image, then for a certain value of $\boldsymbol{d}$ and $\boldsymbol{\theta}$, the co-occurrence matrix is of size $N_g x N_g$. Formally, co-occurrence matrix is defined as [83,94]:

$P(i,j,d,\theta) =$ The number of pixel-pairs lying at pixel distance d and direction θ, in an image, such that first pixel in the pixel-pair has gray-level value i and second pixel has gray level value j.

The most common choices for θ are 0°, 45°, 90° and 135°. Thus,

$$P(i,j,d,0°) = \#\{((k,l),(m,n)) \epsilon\, I \textit{ such that } k-m=0, |l-n|=d, I(k,l)=i, I(m,n)=j\} \tag{4.1}$$

$$P(i,j,d,45°) = \#\{((k,l),(m,n)) \epsilon\, I \textit{ such that } k-m=d, l-n=-d, I(k,l)=i, I(m,n)=j\} \tag{4.2}$$

$$P(i,j,d,90°) = \#\{((k,l),(m,n)) \epsilon\, I \textit{ such that } |k-m|=d, l-n=0, I(k,l)=i, I(m,n)=j\} \tag{4.3}$$

$$P(i,j,d,135°) = \#\{((k,l),(m,n)) \epsilon\, I \textit{ such that } k-m=d, l-n=d, I(k,l)=i, I(m,n)=j\} \tag{4.4}$$

where, # denotes the number of elements in the set.

A set of 13 texture features is used in this study, and these are defined on a single co-occurrence matrix. For a chosen distance d=1 (that is one pixel) and for angles θ = 0°, 45°, 90°, and 135°, four values for each of the texture feature are computed and their average is taken for further analysis. The notations used to calculate these texture features are given as follows:

Notations	*Description*
$P(i,j)$	$Probability\ that\ the\ i\ and\ j\ grey\ level\ combination$ occures $in\ sequence$
$p(i,j)$	$(i,j)th$ entry in a normalized co − occurrence matrix, $=\frac{P(i,j)}{R}$ where, R is a normalizing constant.
$p_x(i)$	$=\sum_{i=1}^{Ng} P(i,j)$, obtained by summing the rows of p(i, j).
N_g	Number of distinct gray levels in the quantized image.
$p_y(j)$	$=\sum_{j=1}^{Ng} P(i,j)$, obtained by summing the columns of p(i, j).
$p_{(x+y)}(k)$	$=\sum_{i=1}^{Ng} \sum_{\substack{j=1 \\ i+j=k}}^{Ng} p(i,j)$, $k = 2, 3, \ldots \ldots, 2N_g$.
$p_{(x-y)}(k)$	$=\sum_{i=1}^{Ng} \sum_{\substack{j=1 \\ \|i-j\|=k}}^{Ng} p(i,j)$, $k = 0,1,2, .. N_g - 1$.

$$\sum_i = \sum_{i=1}^{Ng} \quad and \quad \sum_j = \sum_{j=1}^{Ng}$$

μ_x, μ_y, σ_x and σ_y are the means and standard deviations of p_x and p_y.

The Haralick features calculated in this thesis work are detailed in the following section [18].

1) Angular Second Moment (ASM): It is measure of uniformity or energy of texture. It is computed as summation of squared elements of SGLCM.

$$ASM = \sum_i \sum_j \{p(i,j)\}^2 \tag{4.5}$$

A homogeneous image has a few gray level values so SGLCM contains few but high values of $\mathrm{P}(i, j)$. So, value of ASM will be high.

2) *Contrast (CNT):* It is measure of intensity contrast between pixel and its neighborhood over the entire image and is difference moment of SGLCM.

$$CNT = \sum_{n=0}^{Ng-1} n^2 \left\{ \sum_{i=1}^{Ng} \sum_{j=1}^{Ng} \sum_{|i-j|=n} p(i,j) \right\} \tag{4.6}$$

High contrast value provides clear separation between objects in an image.

3) *Correlation (CRC):* It is measure of how correlated a pixel is to its neighbor over the entire image.

$$CRC = \frac{\sum_i \sum_j (ij)p(i,j) - \mu_x \mu_y}{\sigma_x \sigma_y} \tag{4.7}$$

4) *Inverse Difference Moment (IDM):* It is measure of closeness of distribution of elements in co-occurrence matrix to main diagonal.

$$IDM = \sum_i \sum_j \frac{1}{1 + (i-j)^2} p(i,j) \tag{4.8}$$

This feature has relatively high value when high values of matrix are near the main diagonal. High value indicates homogeneity of image.

5) *Variance (VAR):* It provides measure of deviation from mean value of SGLCM.

$$VAR = \sum_{i=1}^{N_g} (i-j)^2 \, p_{x+y}(i) \tag{4.9}$$

6) *Sum Average (SAVG):* It indicates brightness of image. Sum average is high if image is bright.

$$SVAG = \sum_{i=2}^{2N_g} i p_{x+y}(i) \tag{4.10}$$

7) Entropy (ENT): It is statistical measure of randomness in image. Homogeneous image have high entropy while inhomogeneous image have low entropy.

$$ENT = -\sum_{i}\sum_{j} p(i,j)\log\big(p(i,j)\big) \tag{4.11}$$

8) Sum Entropy (SENT): It measure entropy of vectorP_{x+y}. Its value is lower than entropy.

$$SENT = -\sum_{i=2}^{2N_g} p_{x+y}(i)\log\{p_{x+y}(i)\} \tag{4.12}$$

9) Sum Variance (SVAR): It is measure of deviation of elements of $\mathrm{P}_{x+y}$from sum entropy. It has high value for low contrast image.

$$SVAR = \sum_{i=2}^{2N_g} (i - SENT)^2\, p_{x+y}(i) \tag{4.13}$$

10) Difference Entropy (DENT): It is measure of entropy of vector P_{x-y}. Its weight increases as we move away from main diagonal.

$$DENT = -\sum_{i=0}^{N_g-1} p_{x-y}(i)\ \log\{p_{x-y}(i)\} \tag{4.14}$$

11) Difference Variance (DVAR): It is measure of deviation of elements of P_{x-y} vector from difference entropy. Sum variance and difference variance are opposite to each other.

$$DVAR = \sum_{i=0}^{N_g-1} (i - DENT)^2\, p_{x-y}(i) \tag{4.15}$$

12) Information Measures of Correlation 1 (IMC1): Homogeneous image has low value for information measures of correlation 1.

$$IMC1 = \frac{HXY - HXY1}{\max\{HX, HY\}} \tag{4.16}$$

$where, HX \ and \ HY \ are \ entropies \ of p_x \ and \ p_y \ and$

$$HXY = -\sum_i \sum_j p(i,j) \log\big(p(i,j)\big),$$

$$HXY1 = -\sum_i \sum_j p(i,j) \log\{\mathrm{p_x(i)p_y(j)}\},$$

$$HXY2 = -\sum_i \sum_j p_x(i)p_y(j) \log\{\mathrm{p_x(i)p_y(j)}\}.$$

13) *Information Measures of Correlation 2 (IMC2):* Image with more energy has low value of information measures of correlation 2.

$$IMC2 = (1 - \exp[-2.0(HXY2 - HXY)])^{1/2} \tag{4.17}$$

4.3.2 GLDS Features

The GLDS algorithm uses first-order statistics of local property values based on the absolute differences between pairs of gray levels or of average gray levels to extract the following 5 texture measures: Homogeneity, Contrast, Mean, Energy and Entropy [23]. These features are based on the absolute difference between pairs of gray levels separated at distance $\delta = (\Delta x, \Delta y)$. For a given displacement $\delta = (\Delta x, \Delta y)$, the difference image $f_\delta(x,y)$ is defined as:

$$f_\delta(x,y) = |f(x,y) - f(x+\Delta x, y+\Delta y)| \tag{4.18}$$

and p_δ is the probability density (gray-level histogram) of $f_\delta(x,y)$ for m gray levels. Various texture features extracted from p_δ are:

1) *Homogeneity (HOMG):* It is a measure of similarity in grey level intensities.

$$HOMG = \frac{\sum p_\delta(i)}{1+i} \tag{4.19}$$

2) *Contrast (CNTG):* It is a measure of grey level intensity difference between neighboring pixels.

$$CNTG = \sum i^2 p_\delta(i) \tag{4.20}$$

3) *Mean (MENG):* It is the average value of the grey level intensities within a given area.

$$MENG = \frac{1}{m}\sum i\, p_\delta(i) \tag{4.21}$$

4) Energy (ENGG): It represents amplitude of grey level values.

$$ENGG = \sum p_\delta(i)^2 \tag{4.22}$$

5) *Entropy (ENTG):* It measures the randomness in grey level intensities within the given area.

$$ENTG = -\sum p_\delta(i) \log p_\delta(i) \tag{4.23}$$

4.3.3. FOS Features

In this model, the first order statistics describing the image gray-level distribution (histogram) is used. These features are derived from normalized histogram of image. Assuming pixel values of the image to be random variables that can take discrete values $i = 0,1, \dots N_g - 1$ where, N_g is the number of gray levels, the normalized histogram is defined as:

$$p(i) = \frac{number\ of\ pixels\ with\ intensity\ i}{total\ number\ of\ pixels} \quad where, i = 0, 1, \dots N_g - 1 \tag{4.24}$$

Central moments derived from the histogram are used to characterize texture of the image. The following statistical features are computed on the basis of pixel's gray value in the image: Mean value, Skewness and Kurtosis [95].

1) Mean (MENF or μ): Mean provides the measure of average intensity level of image.

$$\mu = \sum_{i=0}^{N_g-1} ip(i) \tag{4.25}$$

2) *Skewness (SKWF or μ_3):* Skewness is a measure of lack of symmetry in the histogram.

$$\mu_3 = \sigma^{-3} \sum_{i=0}^{N_g-1} (i-\mu)^3 p(i) \tag{4.26}$$

3) *Kurtosis (KRTF or μ_4):* Kurtosis is variability of grey level intensity around the mean value.

$$KRTF = \mu_4 = \sigma^{-4} \sum_{i=0}^{N_g-1} (i-\mu)^4 p(i) - 3 \tag{4.27}$$

The constant value 3 is used in equation 4.27 to normalize μ_4 to 0 for Gaussian shaped histogram.

4.3.4. Laws' TEM Features

Another texture quantification approach that uses convolution with specialized filters is based on Laws masks [19]. These are constructed using three foundational vectors, which correspond to center-weighted Local averaging, Edge detection with symmetric first differencing, and Spot detection with second differencing, in one dimension. These measures are computed by first applying small convolution kernels to a digital image and then performing a nonlinear windowing operation.

$$L5 = [\ 1 \quad 4 \quad 6 \quad 4 \quad 1] \tag{4.28}$$

$$E5 = [-1 \quad -2 \quad 0 \quad 2 \quad 1] \tag{4.29}$$

$$S5 = [-1 \quad 0 \quad 2 \quad 0 \quad -1] \tag{4.30}$$

From these one-dimensional convolution kernels, 9 different two-dimensional kernels are obtained by convolving a vertical 1-d kernel with a horizontal 1-d kernel. A listing of all 5x5 kernel names is given below:

L5L5 E5L5 S5L5

L5E5 E5E5 S5E5

L5S5 E5S5 S5S5

Subsequently, the texture energy measures are computed by applying convolution kernels: The digital image (or regions) of size N rows and M columns is convoluted with each of these 9 kernels. The result is a set of 9 NxM grayscale images. The windowing operation is performed in a local neighborhood as follows:

$$NEW(x,y) = \sum_{i=-7}^{7}\sum_{j=-7}^{7}|OLD(x+i,y+j| \tag{4.31}$$

All convolution kernels except L5L5 are zero-mean. Thus, L5L5T is used as normalizing image. Normalizing any TEM image pixel-by-pixel with the L5L5T image will normalize that feature for contrast. After the normalization L5L5T image is discarded. The similar features in vertical and horizontal directions can be combined to create rotation invariant features. The following 6 TEM features are used in this study: LL Texture Energy from L5*L5 kernel; EE Texture energy from E5*E5 kernel, SS Texture energy from S5*S5 kernel, LE average texture energy from L5*E5 and E5*L5 kernels, ES average texture energy from E5*S5 and S5*E5 kernels, and LS average texture energy from L5*S5 and S5*L5 kernels. When the image is convolved with Laws' masks, metrics that quantify the texture of a region of interest are obtained by computing statistics from the filtered image. These statistics are typically the sum of the absolute or squared pixel values normalized by the number of pixels thus called energy measures.

4.3.5. FPS Features

This texture model contains the information on the texture orientation, grain size, and texture contrast of the image. The Discrete

Fourier Transform (DFT) approach is used here for texture quantification because repetitive global patterns are difficult to describe with spatial techniques but relatively easy to represent with peaks in the spectrum [17]. The Radial sum and the Angular sum of the DFT were computed to describe texture. FPS features are computed from the power spectrum in the frequency domain.

$$|F(u,v)|^2 = F(u,v)F^*(u,v) \tag{4.32}$$

where, $F(u,v)$ is the Fourier transform of the image and $F^*(u,v)$ is the complex conjugate of Fourier transform of the image.

Spectral features are expressed in polar coordinates to yield a function $S(r,\theta)$. For each direction θ, $S(r,\theta)$ can be expressed as $S_\theta(r)$ and similarly for each frequency r, $S(r,\theta)$ can be expressed as $S_r(\theta)$. Analyzing $S_\theta(r)$ for a fixed value of θ gives the behavior of spectrum along a radial direction from the origin and is called wedge analysis whereas analyzing $S_r(\theta)$ for a fixed value of r gives the behavior of spectrum along a circle centered on the origin and is called ring analysis. A global interpretation is obtained by summing over discrete variables:

$$S_\theta = \sum_{\theta=0}^{\pi} S_\theta(r) \tag{4.33}$$

and

$$S_r = \sum_{r=1}^{R_0} S_r(\theta) \tag{4.34}$$

where, R_0 is the radius of circle centered at origin.

In this texture model, two features: S_r and S_θ are calculated and these are measure of the orientation of the texture.

4.3.6. SFM Features

The SFM measures the statistical properties of pixel pairs at several distances within an image, which are used for statistical analysis. Based on the SFM, the texture features like Coarseness, Contrast, Periodicity, and Roughness are computed [24]. In this model a matrix M_{sfm} of size $(L_r + 1)$ x $(2L_c + 1)$ is constructed whose (i, j) element is the d statistical feature of the image, where $d = (j - L_c,\ i)$ is an intersample spacing distance vector for $i = 0,1, \dots \dots .., L_r$ and $j = 0,1, \dots \dots .2L_c$ and L_r and L_c are the constants which determine the maximum inter-sample spacing distance. In this method, two such matrices constructed are the contrast matrix (M_{con}) and the dissimilarity matrix (M_{dss}) whose (i, j) elements are 'change in contrast' and 'change in dissimilarity' respectively.

A δ statistical feature is the statistical feature of an image I with inter-sample spacing distance vector $\delta = (\Delta x, \Delta y)$. $\delta contrast$ and $\delta dissimilarity$ are defined as:

$$\delta contrast\text{: } CON(\delta) \equiv E\{[I(x, y) - I(x + \Delta x, y + \Delta y)]^2\} \qquad (4.35)$$

$$\delta dissimilarity\text{: } DSS(\delta) \equiv E\{|I(x, y) - I(x + \Delta x, y + \Delta y)|\} \qquad (4.36)$$

where, $E\{\cdot\}$ denotes the expectation operation.

The four texture features extracted from image are:

1) *Coarseness (CRCC):* It is a measure of the 'size' of primitives. It represents occurrence of similar grey levels in a given area.

$$CRSS = c/m_{crs} \qquad (4.37)$$

where c is a normalizing factor and $\mathrm{c} = 100$ and m_{crs} is the mean of all elements of the matrix M_{dss}

$$m_{crs} = \sum_{(i,j) \in N_r} DSS(i, j)/n \qquad (4.38)$$

where $\mathrm{N_r}$ is the set of displacement vectors and n is the number of elements in the matrix $\mathrm{M_{dss}}$.

2) *Contrast (CNTS):* It is a measure of difference in the grey level intensities for a specified neighborhood.

$$CNTS = \left[\sum_{(i,j)\in N_r} CON(i,j)/4 \right]^{1/2} \tag{4.39}$$

3) *Periodicity (PER):* The feature is a measure of the repetition of a specific pattern in the image.

$$PER = \frac{\bar{M}_{dss} - M_{dss}}{\bar{M}_{dss}} \tag{4.40}$$

where $\bar{M}_{dss}$ is the mean of all elements of M_{dss} and M_{dss} is the deepest valley in the matrix.

4) *Roughness (RGH):* It measures the dissimilarity between the neighboring pixels

$$RGH = (D_f^{(h)} + D_f^{(v)})/2 \tag{4.41}$$

where $D_f^{(h)}$ and $D_f^{(v)}$ are the estimated fractal dimensions in the horizontal and vertical directions by considering the displacement vector of the forms $(\Delta x, 0)$ and $(0, \Delta y)$ respectively. D_f is obtained from the equation:

$$D_f = 3 - H \tag{4.42}$$

and H can be evaluated from the dissimilarity matrix since the $(i, j + L_c)$ element of the dissimilarity matrix is $E\{|\Delta I|\}$ with $\delta = (j, i)$. H and $E\{|\Delta I|\}$ are related as:

$$E\{|\Delta I|\} = C||\delta||^H \tag{4.43}$$

Thus, first of all H is estimated separately for horizontal and vertical directions from dissimilarity matrix as per equation (4.43) by considering displacements of $(\Delta x, 0)$ and $(0, \Delta y)$ respectively. Then $D_f^{(h)}$ and $D_f^{(v)}$ are evaluated according to equation (4.42) and finally roughness is calculated according to equation (4.41).

In this thesis work SFM features are calculated for $L_r = 4$ and $L_c = 4$.

4.3.7. Fractal Features

The Hurst coefficients ($H(k)$) are computed for different image resolutions, where a smooth texture surface is described by a large value of the parameter $H(k)$, whereas the lower value indicates a rough texture Surface [22].

In this model, hurst coefficient is calculated at two image resolutions: Original image of size NxM; termed as H1and original image scaled by a factor of 1⁄2 and of size N⁄2 x M/2; termed as H2.

For a given image I Hurst coefficient H is estimated from the relationship:

$$E(|\Delta I|) = k(\Delta r)^H \tag{4.44}$$

where, $E(\cdot)$ denotes the expectation operator, $\Delta I \equiv I(x_2, y_2) - I(x_1, y_1)$, $\Delta r \equiv \|(x_2, y_2) - (x_1, y_1)\|$ is the spatial distance and $k = E(|\Delta I|)_{\Delta r=1}$

Hurst coefficients for the two resolutions are evaluated from equation (4.45) as the texture features.

$$\log E(|\Delta I|) = \log k + H \log(\Delta r) \tag{4.45}$$

4.4 ROI SELECTION AND TEXTURE ANALYSIS

Using the previously discussed seven texture models, total 35 features were extracted from each ROI, and these features are used for further analysis.

4.4.1 Previous work

Many researchers in the past have used ROI for texture analysis [25, 96-99]. ROI in the ultrasound image is segmented into maximum possible number of non-overlapping small squared shape regions of fixed size to acquire a large dataset for the further studies. Since the subsequent calculations and analysis significantly depend upon these ROIs, thus the 'size and location' of the ROI is very crucial. Some of the researchers, who have used ROIs from a segmented region for focal liver diseases, termed these regions as Segmented Regions-of-Interest (SROl) [100, 101]. However, usually these regions are known as region of interest only. In case of tissues or organs, texture of an ROI with a specified window size is more useful than the whole image [99]. The classification performance for focal liver lesion could be notably affected by ROI selection approaches and feature extraction methods adopted. Researchers have revealed that "tissue characteristics vary according to the location and size of ROI, which has a considerable impact on the classification performance" [102, 103]. Jeon et al. used multiple ROIs for different texture features to classify the focal liver lesions. ROI selection for liver lesion classification is usually done with respect to size of lesion and an inner rectangular shaped ROI has been used by previous researchers [28, 91, 100, 104]. Therefore, it is important to select an appropriate location and size of the ROI for an efficient algorithm. Moreover, a large image database is possible with multiple ROIs from one image to improve classification rate [104].

4.4.2 ROI Location and Shape

The ROIs have been selected by the experienced radiologists along or near the center of the image to avoid any distorting effects in ultrasonic wave patterns, such as side lobes and grating lobes. The depth of the ROIs has been chosen in such a way that the undesired effects of the reverberations in the shallow parts and the attenuation in the deep parts are negligible [25, 38, 105].

Regarding the shape of the ROI, most of the researchers have used square shape ROIs [10, 25, 38, 92, 96, 97, 104-106]. The main reason for this shape is that, the most of the texture models are based on matrices calculations, which could be easily done for square matrices. Thus, the square shaped ROIs have been selected for the present study.

4.4.3 ROI Size

It has been established by many researchers that ROI size and shape has a significant effect on the ultrasound image analysis [97, 98, 102-104].

However the optimal size of ROI depends upon the methodology used for feature extraction and the final application. Different sizes of ROI have been selected for different applications, like for lesion classification, an ROI size of 10x10 pixels is sufficient and had been successfully used by the researchers [96, 104]. In case of liver cyst and lesions, an ROI of 25x25 pixels has been used [100]. Since the size of ROI varies with application and imaging modality. Thus, it is very important to study the effect of ROI size on the texture analysis for liver tissue characterization in ultrasound images.

Earlier researchers have revealed that ROI should have enough number of pixels to provide a good statistical population because the texture parameters are considered sensitive to size of the sample [96, 106]. To get the reliable result of texture analysis, there must be at least 800 pixels in the ROI [25]. Various ROI sizes have been proposed in the literature for texture analysis of liver tissue. Ahmadian et al. have chosen ROI of 75 x75 pixels in case of diffuse liver disease [92]. A 64x64 pixels ROI from the ultrasonic liver image for further analysis has been selected many times [38, 91, 106]. Many researchers preferred even some smaller sized ROIs such as a 40x40 pixels used by Mancini et al. for liver classification, Kyriacou et al. selected a 32x32 pixels ROI for diffuse liver diseases and Stipple had used 30x30 ROI to study the effect of speckle reduction in liver ultrasound images [73, 97, 105]. Recently, ROIs of the size 25x25 pixels have also been tested, after trail and interaction with radiologists [10, 100]. Some of the researchers have applied even a size of 10x10 pixels for their analysis related to liver [96, 104]. Although these researchers have used multiple ROIs for texture analysis, but the size of 10x10 pixels is too small to able to provide a good statistical population in case of diffuse liver disease. A concise review of all the methods discussed here is presented in the Table 4.1.

Table 4.1

Review of different ROIs in previous methods for Liver classification

Sr. No.	ROI Size (pixels)	Researcher(s) Year	Application	Multiple ROIs	Remarks
1	75x75	Ahmadian et al. 2004 [92]	Liver classification	NO	ROI size is very large, and it may contain blood vessels, bile duct or cysts etc.
2	64x64	Kadah et al. 1996 [25]	Diffused Liver	NO	
		Yoshida et al. 2003 [91]	Focal Liver	NO	
		Zaid et al. 2006 [106]	Diffused Liver	NO	
		Li et al. 2008 [29]	Diffused Liver	YES	
		Minhas et al. 2012 [38]	Diffused Liver	NO	
3	40x40	Mancini et al. 2009 [105]	Focal Liver	YES	Moderate size with easily avoidable blood vessels, bile duct or cyst
4	32x32	Kyriacou et al. 1997 [97]	Diffused and Focal Liver	YES	
5	30x30	Stippel et al. 2002 [73]	Liver Ultrasound	NO	
6	25x25	Mittal et al. 2011 [100]	Focal Liver	YES	
7	10x10	Sujana et al. 1996 [96]	Liver	YES	ROI size is so small that a statistical analysis is not reliable in case of diffuse liver disease.
		Poonguzhali et al. 2007 [104]	Diffused and Focal Liver	NO	

4.5 RESULTS AND DISCUSSIONS

Since there are many ROI sizes available in the literature for texture analysis of liver, therefore, an experimental study is performed to find the optimal ROI size for the present study. For this purpose, different sized

ROIs have been extracted from each image as shown in Figure 4.1. All the ROIs are selected near the centre line as directed by the radiologists. Different sized ROIs are selected in such a way that their central pixel is same, as shown in Figure 4.1. This has been done for a reliable comparison among different ROIs.

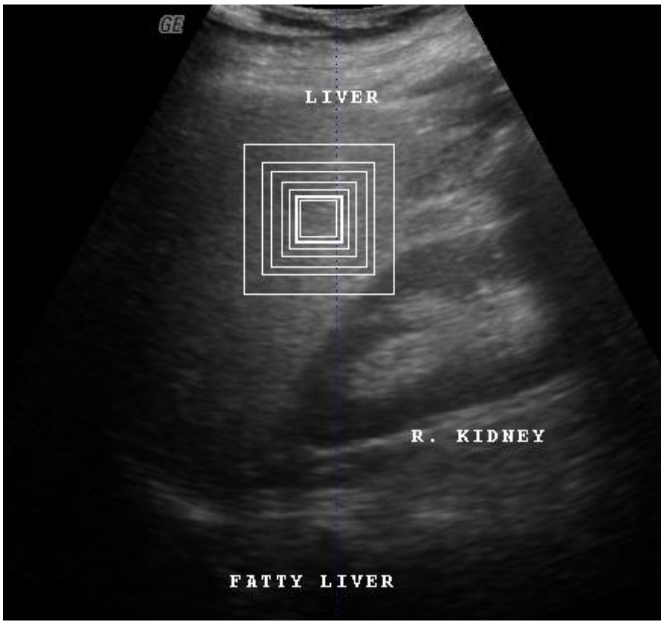

Figure 4.1 ROIs of Different Sizes for Analysis.

4.5.1 Pearson's Correlation Coefficient

Different size ROIs from an image, have been extracted, as shown in Figure 4.2. Comparison of all these different sized ROIs has been made using Pearson's Correlation Coefficient (PCC) to study and analyze the similarity of information content between these ROIs. Table 4.2 shows comparison of SGLCM features extracted from different sized ROIs from 100x100 pixels to 10x10 pixels ROI for a given image.

PCC has also been computed between the ROIs, and the results shown in Table 4.3 indicate that there is significant difference in correlation coefficient of extreme sizes like 100x100 pixels and 10x10 pixels with all other sizes. But the middle sizes like 64x64 pixels to 30x30 pixels have very similar information.

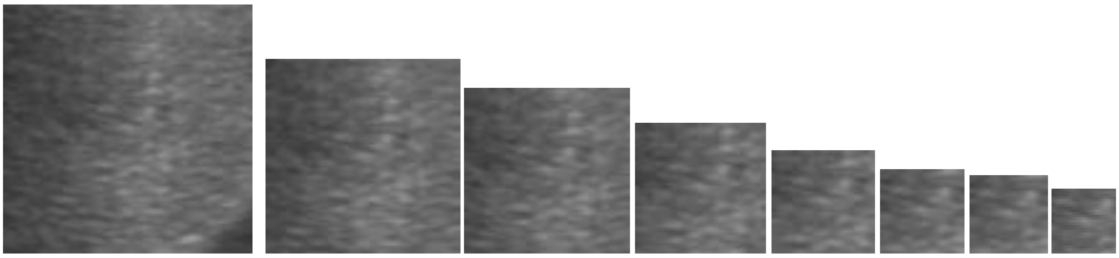

(a) (b) (c) (d) (e) (f) (g) (h)

Figure 4.2 Sample of individual ROIs of different sizes used for the analysis, (a)100x100 pixels (b) 75x75 pixels (c) 64x64 pixels (d) 50x50 pixels (e) 40x40 pixels (f) 30x30 pixels (g) 25x25 pixels (h) 10x10 pixels.

Table 4.2

Values of SGLCM features for different ROIs in one image UST16

Sr. No.	Feature	ROI Sizes							
		100x100 Pixels	75x75 Pixels	64x64 Pixels	50x50 Pixels	40x40 Pixels	30x30 Pixels	25x25 Pixels	10x10 Pixels
1	ASM	0.451	0.462	0.477	0.479	0.486	0.525	0.522	0.492
2	CNT	0.059	0.059	0.070	0.088	0.099	0.098	0.103	0.106
3	CRC	0.910	0.891	0.867	0.831	0.804	0.783	0.766	0.772
4	VAR	13.188	13.614	13.953	14.380	14.622	14.767	14.625	14.485
5	IDM	1.275	0.970	0.965	0.956	0.950	0.951	0.948	0.936
6	SAVG	7.224	7.349	7.447	7.565	7.630	7.679	7.647	7.612
7	SVAR	46.453	49.137	50.424	51.828	52.668	53.646	53.186	54.873
8	ENT	0.420	0.430	0.434	0.457	0.465	0.438	0.436	0.429
9	SENT	0.414	0.413	0.414	0.432	0.436	0.410	0.407	0.402
10	DVAR	0.050	0.057	0.066	0.082	0.091	0.090	0.094	0.092
11	DENT	0.087	0.098	0.110	0.130	0.141	0.139	0.144	0.149
12	IMC1	-3.323	-3.287	-3.231	-3.155	-3.115	-3.107	-3.036	-3.022
13	IMC2	0.946	0.941	0.936	0.934	0.930	0.917	0.913	0.902

Table 4.3
Pearson' Correlation Coefficient between different ROI sizes in one image

ROI size (pixels)	100x100	75x75	64x64	50x50	40x40	30x30	25x25	10x10
100x100	1	0.90	0.97	0.84	0.80	0.75	0.71	0.67
75x75		1	0.99	0.98	0.96	0.95	0.93	0.75
64x64			1	0.99	0.99	0.99	0.95	0.78
50x50				1	0.99	0.99	0.99	0.80
40x40					1	0.99	0.99	0.85
30x30						1	0.99	0.89
25x25							1	0.93
10x10								1

Since in most of the previous works the 64x64 pixels ROI size has been used thus it is taken as reference for the analysis [25, 38, 91]. To find the minimum sized ROI (available in literature review), having similar information as in the 64x64 sized ROI, small sized ROIs have been compared. To show that the 30x30 pixel sized ROI has almost similar information as contained by 64x64 pixels ROI, Pearson's Correlation Coefficient (PCC) is used. As shown in Table 4.4, different texture features are compared for 64x64 and 30x30 pixels ROIs for normal liver ultrasound images. Although, the PCC has been found between these two ROIs for each image in dataset, but only three of them have been shown here in Table 4.4. Similar comparison for three randomly picked fatty liver images has been presented in Table 4.5. The analysis of results shows that, the PCC is very high between the features of 64x64 and 30x30 pixels size ROIs. This indicates that the information contained in 64x64 pixels size ROI is similar to that of 30x30 pixels size ROI.

Table 4.4

Comparison of different texture features from 64x64 and 30x30 pixels ROIs for Normal liver

Sr. No.	Images / Features	UST_N1		UST_N2		UST_N3	
		64x64	**30x30**	**64x64**	**30x30**	**64x64**	**30x30**
1	ASM	0.415	0.389	0.425	0.429	0.443	0.505
2	CNT	0.107	0.127	0.084	0.083	0.077	0.083
3	CRC	0.783	0.746	0.850	0.833	0.862	0.804
4	VAR	6.035	6.417	11.506	12.721	7.389	7.411
5	IDM	0.947	0.936	0.958	0.959	0.961	0.959
6	SAVG	4.855	5.014	6.742	7.101	5.371	5.407
7	SVAR	20.606	21.905	40.761	45.840	25.392	26.191
8	ENT	0.445	0.420	0.463	0.422	0.459	0.389
9	SENT	0.413	0.428	0.439	0.398	0.436	0.364
10	DVAR	0.097	0.112	0.079	0.078	0.073	0.078
11	DENT	0.147	0.165	0.125	0.124	0.118	0.124
12	IMC1	-3.105	-3.060	-3.165	-3.189	-3.235	-3.132
13	IMC2	0.918	0.917	0.939	0.923	0.941	0.903
14	IER	2.415	2.399	2.473	2.436	2.397	2.375
15	RGH	9.734	9.805	14.825	13.176	10.590	9.740
16	CNTS	11.622	11.446	8.005	8.796	10.355	10.870
17	S_r	2745.420	5333.813	4149.975	7779.840	3212.908	6054.970
18	S_θ	252.800	583.513	292.604	683.919	292.995	566.746
19	H1	0.376	0.388	0.360	0.363	0.384	0.402
20	H2	0.161	0.213	0.125	0.219	0.222	0.244
21	ENGG	0.032	0.026	0.025	0.020	0.028	0.024
22	ENTG	3.627	3.819	3.827	4.088	3.739	3.908
23	SKWF	0.352	0.166	0.364	-0.030	-0.147	-0.165
24	MENF	85.580	82.998	129.399	121.037	100.223	94.154
25	KRTF	2.734	2.880	2.858	3.123	2.688	2.710
	PCC	**0.99**		**0.99**		**0.98**	

Table 4.5

Comparison of different texture features from 64x64 and 30x30 pixels ROIs for Fatty liver

Sr. No.	Images / Features	UST_F1		UST_F2		UST_F3	
		64x64	30x30	64x64	30x30	64x64	30x30
1	ASM	0.755	0.789	0.883	0.937	0.537	0.857
2	CNT	0.080	0.088	0.029	0.016	0.085	0.034
3	CRC	0.833	0.796	0.684	0.668	0.799	0.694
4	VAR	19.241	18.696	16.109	15.821	17.705	16.326
5	IDM	0.960	0.956	0.985	0.992	0.958	0.983
6	SAVG	8.760	8.628	8.048	7.984	8.409	8.101
7	SVAR	70.944	68.972	62.799	62.545	65.197	63.439
8	ENT	0.297	0.224	0.142	0.085	0.406	0.158
9	SENT	0.289	0.228	0.133	0.080	0.381	0.148
10	DVAR	0.075	0.082	0.029	0.016	0.079	0.034
11	DENT	0.121	0.129	0.057	0.036	0.126	0.065
12	IMC1	-3.184	-3.137	-3.075	-2.925	-3.122	-3.035
13	IMC2	0.920	0.904	0.660	0.542	0.910	0.685
14	IER	0.654	0.704	0.655	0.626	0.665	0.631
15	RGH	2.480	2.460	2.442	2.467	2.456	2.486
16	CNTS	8.848	9.594	5.811	5.754	5.749	5.589
17	S_r	3951.1112	7934.871	2211.023	4444.446	2853.193	5735.009
18	S_θ	235.539	626.294	235.932	870.907	268.517	1047.233
19	H1	0.330	0.336	0.351	0.348	0.360	0.344
20	H2	0.185	0.189	0.274	0.249	0.231	0.243
21	ENGG	0.041	0.027	0.042	0.023	0.037	0.018
22	ENTG	3.545	3.776	3.406	3.968	3.502	4.136
23	SKWF	0.268	0.010	0.126	0.445	-0.241	-0.051
24	MENF	123.379	123.839	68.976	69.222	89.053	89.464
25	KRTF	2.811	2.847	2.422	2.544	2.257	2.024
	PCC	**0.99**		**0.99**		**0.99**	

4.5.2 Box-plots

Another way of comparing the information content between the two ROI sizes is the box-plot. The box-plot is able to display the class separation ability of a particular dataset. In this study, different features have chosen for box plots. Figure 4.3a shows the similarity of information content in 64x64 and 30x30 pixel sizes for ASM feature of SGLCM texture model for normal and fatty liver.

The class separation ability of the ASM feature from 64x64 pixels size (first two columns in plot) is preserved in 30x30 pixels (last two columns in plot) size also. This shows that if the result from 64x64 ROI infers that ASM of fatty liver dataset is significantly different than that of normal liver then the same result is being given by the 30x30 ROI dataset. Horizontal axis represents the class of liver and size of ROI; Nor-64 and Nor-30 means that box plot is for normal liver image having 64x64 pixels and 30x30 pixels ROI respectively. Similarly Fat-64 and Fat-30 represent 64x64 pixels and 30x30 pixels ROI from fatty livers.

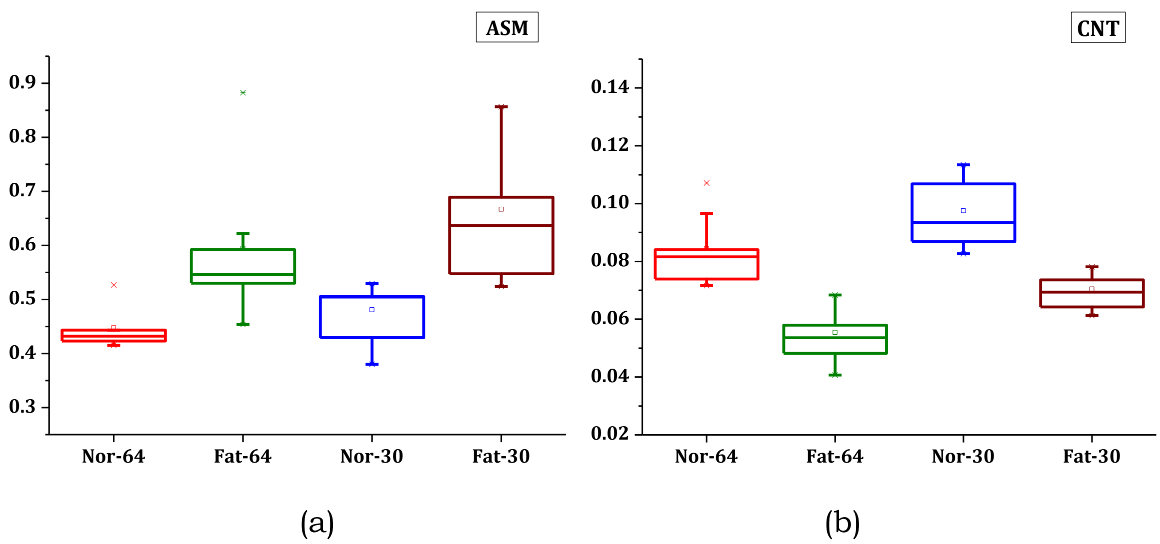

Figure 4.3 Box-plot for ASM and CNT features in Normal and Fatty liver from 64x64 ROI and 30x30 ROI

Similar observation are made from the box plots for contrast (CNT), as shown in Figure 4.3b, that is the class separation ability is preserved. Box plots for Homogeneity (HOMG) and Energy (ENGG) from GLDS texture model are also shown here in Figures 4.4a and Figure 4.4b. In these cases, features are not able to differentiate between normal and fatty liver in 64x64 ROI as well as in 30x30 ROI. Thus it can be concluded that the ability of a feature to differentiate the class of liver (normal or fatty) is preserved in 30x30 ROI.

Hence it could be concluded that ROI of size 30x30 pixels and near the centre line of the image is optimal one for liver tissue analysis and characterization.

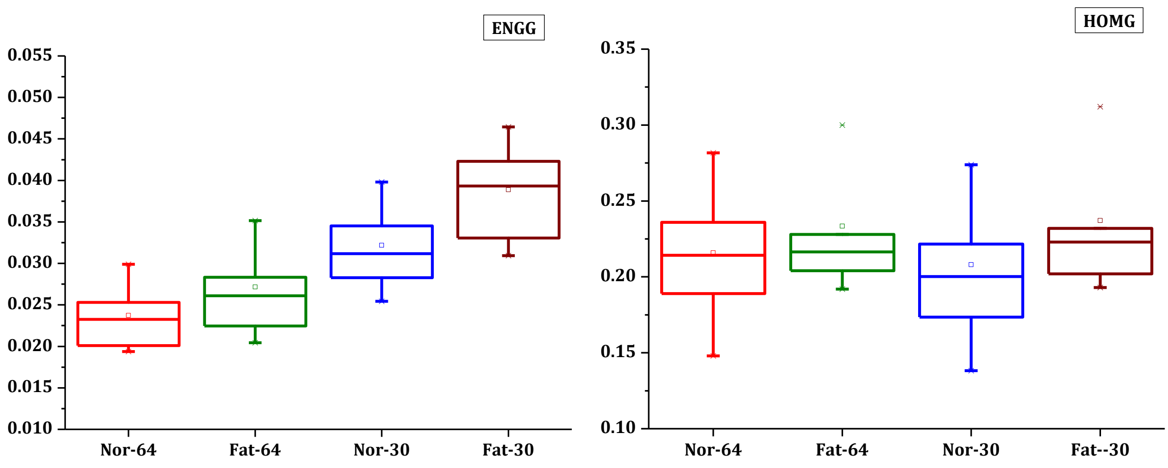

(a) (b)

Figure 4.4 Box-plot for 'ENGG' and 'HOMG' feature in Normal and Fatty liver from 64x64 ROI and 30x30 ROI

4.6 SUMMARY

In computer aided diagnostic system, when the ROIs are used to extract the features then accuracy of the system significantly depends upon the characteristics of ROI. Since liver is very large tissue, therefore, experiments were conducted to find the appropriate 'shape, size and location' of ROI. Different texture models are used to extract features from these ROIs to have reliable analysis for appropriate size of the ROI. Each texture feature carries specific information about the tissue and the ability of retaining that information in different sizes is observed. Thus, significance and background of the various texture models is discussed in the first part of this chapter, and subsequently the experimental analysis for selection of ROI is presented.

It has been observed that 100x100 pixels and 75x75 pixels ROIs are not suitable for liver classification methods because they are big in size and usually contain blood vessels or bile duct. However ROIs of 10x10 pixels and 25x25 pixels are too small to have sufficient information to get a reliable statistical analysis from them. These small sized ROIs may be useful in case of cyst or small size tumor in liver but not suitable for the present study. Finally the most popularly used ROIs of 64x64 pixels and 30x30 pixels ROIs have been analyzed using Pearson's correlation coefficient and box plot, and it has been found that the information content in 30x30 pixels ROIs is very much similar to the 64x64 pixels ROIs. Thus a 30x30 pixels ROI is useful for the present study.

After the analytical study and discussions with radiologists, it has been observed that a square shaped ROI having size of 30x30 pixels is optimal, and it should be taken along (or near) the centre line of the image. As suggested by the radiologists, multiple ROIs are selected from liver image near the centre. These multiple ROIs lead to a reliable statistics for texture analysis, because large dataset is available. Moreover, smaller size multiple ROIs take lesser computational time than a single bigger ROI. The average value of each feature is computed from these multiple ROIs from an image to perform further analysis.

CHAPTER-5

INFORMATION FUSION BASED METHOD FOR LIVER CLASSIFICATION

5.1 INTRODUCTION

Visual criteria for differentiating the fatty liver and normal liver are generally subjective and diagnosis mainly depends on the capability of the radiologist to examine the variation in textural characteristics in the image, and then comparing them with pathological findings. Some examples of such features are homogeneity and echogenicity (brightness). However, the description of echogenicity by visual examination of images has been widely debated among experienced radiologists, especially in marginal cases. Diagnostic accuracy through visual interpretation is currently estimated to be around 72% [2]. The limited accuracy of visual interpretation further augments the need to use an objective method based on quantitative texture analysis for the liver classification. To design an effective and accurate classification method, selection of the optimal features is the most important task. In this chapter, a method is presented to select the most discriminative features and subsequently, a novel quantitative method is proposed for liver classification by using these optimal features.

5.2 LITERATURE REVIEW

Computer aided classification methods are being used since 1972 when Mountford and Wells classified normal and abnormal liver using A-mode ultrasounds [107, 108] Later on Yajima et al. in 1983 performed a research for liver classification using different classifiers on ultrasound images through texture features [109]. He revealed that liver classification using computer aided methods have more than 90%

accurate. Since then many researchers have used B-mode ultrasound images for liver tissue classification. Nicolas at al. used texture of ultrasound image to discriminate between the liver and the spleen of a healthy human [110]. Wu and others used all the above four texture models for liver characterization, and proposed a new concept based on the multi-resolution fractal dimensions also called Fractal Features (FF). They proposed the application of multi-resolution fractal analysis of hepatoma, cirrhosis and the healthy liver with fair accuracy [22]. A Neural Network based classification technique for diffuse liver disease was proposed by Gebbinck et al. [111]. Kadah *et al.* explored various classification methods to differentiate diffused liver diseases [25]. They reported that the classification technique significantly affected the final diagnosis. Mojsilovic et al. introduced a separable wavelet transform method for detecting early cirrhosis. [112]. Badavi *et al.* reported liver classification using texture analysis through fuzzy logic [26], while Mukherji *et al.* reported a neural-network based classifier [113], whereas Riberio and Sanches suggested a Bayesian classifier [30]. Fractal analysis was explored with the k-means classification method for liver by Balasubramaniam [28]. Lee *et al.* used ANN on fractal geometry for liver classification [114]. An SVM based classification method for fatty liver and normal liver was proposed by Li and his team [29]. Recently, 'grey relational analysis' has been proposed to grade the fatty liver [23]. Most of the above said classification methods have used one or two texture models at time and none of the researchers have studied the features collectively to select the optimal ones. Therefore, in this work, an attempt has been made to present a new classification method using fusion of the best features from different domains. To achieve this goal, information related to the surface of liver has been extracted using different texture models like structural, statistical, frequency and fractal. Subsequently, the best features have been selected to combine them in such a way that, a single quantitative metric could be computed to classify the liver.

5.3 FEATURE SELECTION

Feature selection is the process to reduce the feature dimensionality to an optimal number for maximum performance. As explained in the previous chapter, seven texture models are used to extract features from each ROI. The importance of these texture features in liver surface characterization has been recently established by Singh *et al.* [36]. All the texture features that have been explained in the previous chapter were extracted from training set ultrasound images, whose pathological results are already known and radiologists have also labeled them. The complete methodology used for feature selection is represented in Figure 5.1, and each step is explained in the following sections.

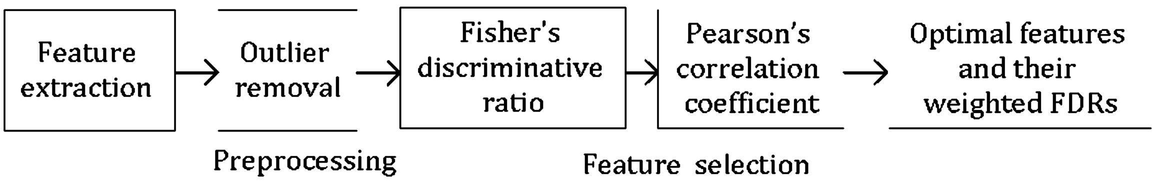

Figure 5.1 Block diagram of feature selection methodology

5.3.1 Outlier Removal

After the feature extraction from multiple ROIs, outlier values are removed from the feature data set. Outliers are the isolated values which lie beyond the 1.5 times the inter quartile range (Whisker box plot). Whisker box plots have been used for all features to identify the outliers in the feature dataset. Figure 5.2 represents the Whisker Box plots for features, *Difference of Entropy* (DENT), *Contrast* (CNT), *Angular Second Moment* (ASM) and *Hurs't' coefficient* (H1). The '+' symbols shown in this figure, are the outlier values. If these extraordinary extreme values are considered in statistical analysis, then result may significantly change and hence they are removed before any further analysis. As it is clear from the Figure 5.2a, DENT and CNT features have a prominent separation for fatty and normal liver values. Same features of different classes are differentiated by letter F and N (DENT_F represents the *difference of entropy* of fatty livers and DENT_N represents that of normal liver). Similarly box plots are given for ASM and H1 features as Figure shown in 5.2b, however their class separation ability is less as their box plots are overlapping. Whisker Box plots were made for each of the feature for two classes, but only four of them are shown in Figure 5.2.

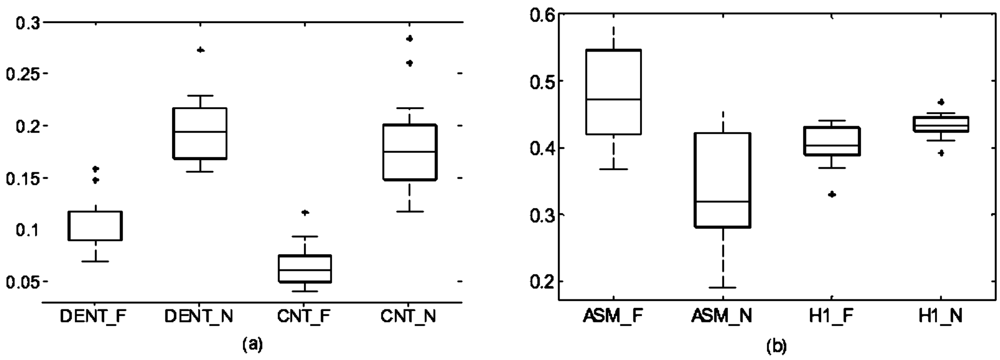

Figure 5.2 Whisker box plots of features to remove outliers (shown by + symbol) (a) Features *'difference of entropy'* and *'contrast'* for fatty (DENT_F and CNT_F) and normal (DENT_N and CNT_N) (b) ASM and H1 features for fatty (ASM_F and H1_F) and normal (ASM_N and H1_N)

5.3.2 Feature Reduction

To select the best features, Fisher's Discriminative Ratio (FDR) and Pearson's Correlation Coefficient (PCC) are used. In the first step, highly discriminative feature are selected using FDR [15]. Higher value of the FDR means that the feature has more power to discriminate between the two classes. Each feature has a FDR value and FDR of 'n' th feature can be computed as:

$$FDR_n = \left| \frac{(\mu_{an} - \mu_{bn})}{\sqrt{(\sigma_{an}^2 + \sigma_{bn}^2)}} \right| \qquad \forall n \in [1, 35] \tag{5.1}$$

where, μ_{a1} and σ_{a1} are the mean and the standard deviation of a given feature F1 (for n=1) in fatty liver (class 'a') and μ_{b1} and σ_{b1} are the mean and the standard deviation of same feature (F1) in normal liver (class 'b'). FDR is a measure of the ability of a feature to separate between two classes. If a feature has low values of standard deviation and more difference in their mean of normal and fatty liver data, that feature has high FDR i.e. high discriminative power. FDR of all 35 features has been reported in Table 5.1. From different texture models, features having FDR more than 1 are selected. For texture models which do not have any feature with FDR greater than 1, then features having highest FDR such that the FDR is more than 0.5 is selected from those texture models. In this way, 12 features (as shown in Table 5.2) from a set of 35 features are selected after FDR analysis, which will be further subjected to PCC analysis for feature reduction.

5.3.3 Pearson's Correlation Coefficient

Out of the selected 12 features shown in Table 5.2, it is further possible to eliminate redundant features. Redundant features can be found using PCC (represented by 'r') between the two variables X and Y using the equation 5.2.

$$r(X,Y)=\frac{\sum_{i=1}^{n}(X_i-\bar{X})(Y_i-\bar{Y})}{\sqrt{\sum_{i=1}^{n}(X_i-\bar{X})^2 \ \sum_{i=1}^{n}(Y_i-\bar{Y}}} \tag{5.2}$$

In this step, it is found that some features are highly correlated (r >0.90), signifying that they are redundant and thus one of them with the lower FDR is dropped from the final list of discriminative features. Table 5.2 represents the correlation coefficients between various features. This process will further reduce the feature set to seven non – correlated discriminative features.

Table 5.1

FDR values for different features

Sr. No.	Texture Model	Texture feature	Fatty Liver		Normal Liver		FDR
			Mean	Std. Dev	Mean	Std. Dev	
1	SGLCM	ASM	0.474	0.067	0.337	0.075	1.367
		CNT	0.061	0.014	0.164	0.034	2.824
		CRC	0.889	0.054	0.822	0.069	0.758
		VAR	6.302	1.409	7.007	2.367	0.256
		IDM	0.969	0.007	0.919	0.016	2.838
		SAVG	4.899	0.545	5.067	0.833	0.169
		SVAR	21.454	4.983	22.391	7.664	0.103
		ENT	0.445	0.071	0.653	0.112	1.567
		SENT	0.427	0.072	0.603	0.104	1.390
		DVAR	0.059	0.012	0.138	0.022	3.149
		DENT	0.099	0.016	0.193	0.024	3.278
		IMC1	-3.283	0.092	-3.109	0.076	1.463
		IMC2	0.940	0.027	0.963	0.019	0.693
2	GLDS	HOMG	0.259	0.051	0.260	0.032	0.015
		CNTG	32.423	5.564	35.832	9.561	0.308
		MENG	4.098	0.817	4.224	0.526	0.130
		ENGG	0.111	0.021	0.113	0.016	0.061
		ENTG	2.466	0.179	2.474	0.132	0.034
3	FOS	SKWF	0.631	0.684	1.078	0.666	0.468
		MENF	51.820	12.370	46.264	10.664	0.340
		KRTF	4.441	2.842	4.943	2.287	0.138
4	FPS	S_r	7726.729	3146.975	8311.420	3611.374	0.122
		S_θ	1862.234	1047.642	2863.847	338.131	0.910
5	SFM	PER	0.702	0.030	0.716	0.029	0.329
		RGH	2.368	0.049	2.327	0.025	0.738
		CNTS	8.143	1.542	8.399	1.142	0.133
		CRSS	14.341	3.129	13.440	1.943	0.245
6	TEM	LL	59192.880	19510.850	71853.890	7912.226	0.601
		EE	775.337	129.212	835.044	129.190	0.327
		SS	114.878	19.775	112.711	19.335	0.078
		LE	4530.755	898.508	5265.773	704.327	0.644
		ES	301.203	50.645	308.980	47.250	0.112
		LS	1650.622	295.999	1749.016	223.034	0.266
7	FF	H1	0.407	0.022	0.434	0.012	1.056
		H2	0.276	0.039	0.299	0.026	0.504

Table 5.2

Correlation coefficient between different features

	DENT	CNT	ASM	H1	S_θ	RGH	LE	IDM	DVAR	ENT	IMC1	SENT
DENT	1.00	0.67	-0.58	0.04	0.14	0.37	0.25	-0.68	**0.99**	**0.98**	0.61	**0.99**
CNT		1.00	0.48	0.02	0.44	0.37	0.65	**-1.00**	0.59	-0.23	**0.90**	-0.29
ASM			1.00	0.47	0.23	0.07	-0.03	-0.48	0.48	-0.77	0.78	-0.79
H1				1.00	0.19	0.03	0.25	-0.12	0.01	0.04	-0. 24	0.43
S_θ					1.00	0.33	0.40	0.41	0.35	0.02	0.12	0.41
RGH						1.00	0.27	0.31	0.05	0.35	0.21	0.02
LE							1.00	0.24	0.79	0.82	0.03	0.89
IDM								1.00	0.59	0.23	0.35	0.29
DVAR									1.00	-0.23	0.89	**0.98**
ENT										1.00	-0.63	**0.99**
IMC1											1.00	-0.67
SENT												1.00

Thus seven best features with the highest FDR are selected and are tabulated in the Table 5.3. In the last column of this table, normalized FDR weightage of all parameters is reported. Normalization has been done to make the total sum of all weighted FDRs equal to unity.

After selecting the best features, they are merged to form the proposed classifier on the basis of feature's value and its discriminative power, followed by liver image classification.

Table 5.3

Best features with highest discriminative power and their normalized FDR weightage

S. No.	**Feature**	**Texture Model**	**Value of 'FDR'**	**Normalized Weighted FDR (WF)**
1	DENT	SGLCM	3.278	0.303
2	CNT	SGLCM	2.824	0.261
3	ASM	SGLCM	1.366	0.126
4	H1	FF	1.056	0.098
5	S_θ	FPS	0.909	0.084
6	RGH	SFM	0.737	0.068
7	LE	Laws' TEM	0.643	0.060
Total				1.000

5.4 PROPOSED CLASSIFIER

The proposed classifier is based on the concept of information fusion, according to which, if information from different domains is combined, the result may be more accurate and informative [116]. The proposed method utilizes discriminative power of a feature and its normalized weight to be fused into a single quantitative metric. This classifier uses only seven features selected on the basis of FDR, i.e., their power to distinguish between the two classes. Since each feature has different FDR, its weight must be considered in the classification method. Therefore in the proposed classifier, the value of each feature is weighted with its FDR. Recently a basic model of this classifier with initial results was presented by Singh *et al.* [36]. They proposed some texture features based on their relevance to the visual criterion adapted by the radiologists to classify the liver. However, in the proposed method, a systematic approach is used for feature selection, and then merging the information into a single value. If feature F_1 has a value X_1 for a test image, the proposed method uses the weight of its FDR and the normalized weight to be included in the final value. The normalized weight is actually the closeness of the feature value to the mean of that feature in the given class. If 'X_1' is very near to the mean μ_{a1} then its normalized weight is high and if X_1 is away from the mean then its normalized weight is less, as depicted in Figure 5.3. The normalized weight of feature F_1 in class '*a*' can be computed by using the equation 5.3.

$$Z_{a1} = \left(1 - \frac{|\mu_{a1} - X_1|}{\sigma_{a1}}\right) \qquad (5.3)$$

Where X_1 is sampled value, μ_{a1} is the mean and σ_{a1} is the standard deviation of feature F_1 in class '*a*'.

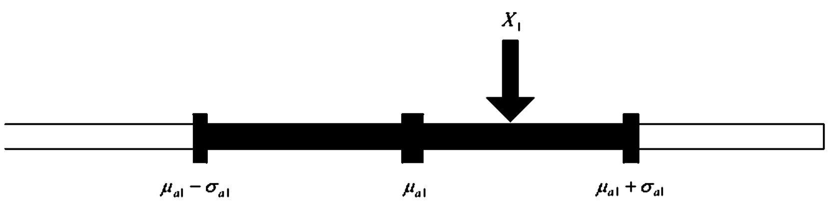

Figure 5.3 The normalized weight of a feature's sampled value X_1

Normalized weight (or modified z-score) of each feature is computed to see, how much a feature's value lies near the mean of a class. Using the equation 5.3, modified z-score of each feature is calculated for both classes and this value will be maximum (1.00) when the feature's value is equal to the mean value of that feature in the given class (X_1=μ_{a1}). As X_1 falls outside the range of $\mu_1 \pm \sigma_1$ (mean ± standard deviation), the Z_{a1}

become 'negative' and thus decreases the overall score of that particular class.

Let Z_{a1} be the modified z-score of feature F_1 and its FDR weightage is WF_1. Then, the value of weighted z-score WZ_{a1} of feature F_1 for the class '*a*' can be calculated as:

$$WZ_{a1} = WF_1 \times Z_{a1} \tag{5.4}$$

and the total weighted z-score WZ_A for seven features for the class '*a*' can be calculated as:

$$WZ_A = \sum_{n=1}^{7} WZ_{an} \tag{5.5}$$

The aggregate operator adds the effect of each feature's present value and its FDR weightage in the final reading. Similarly, the total value of the weighted z-score for the class '*b*' can be found by equation 5.6.

$$WZ_B = \sum_{n=1}^{7} WZ_{bn} \tag{5.6}$$

Finally, the single quantitative metric, called *discriminative index* (D_I) is

$$D_I = WZ_A - WZ_B \tag{5.7}$$

WZ_A and WZ_B are the values that contain information from different aspects of liver surface. The difference between these two values is represented by D_I, that gives the quantitative measure of steatosis in the liver. On the basis of analysis of results from training set, a threshold value of D_I can be found that can be decisive for the classification. The working of the proposed method can be summarized by the block diagram shown in Figure 5.4. If WZ_A is more than WZ_B then the test image is of fatty liver and otherwise normal liver. More difference in WZ_A and WZ_B indicates higher confidence level of the result. In the proposed method, not only the modified z-score of a feature is used but weighted FDR is also included in calculation as each feature has its own discriminative power.

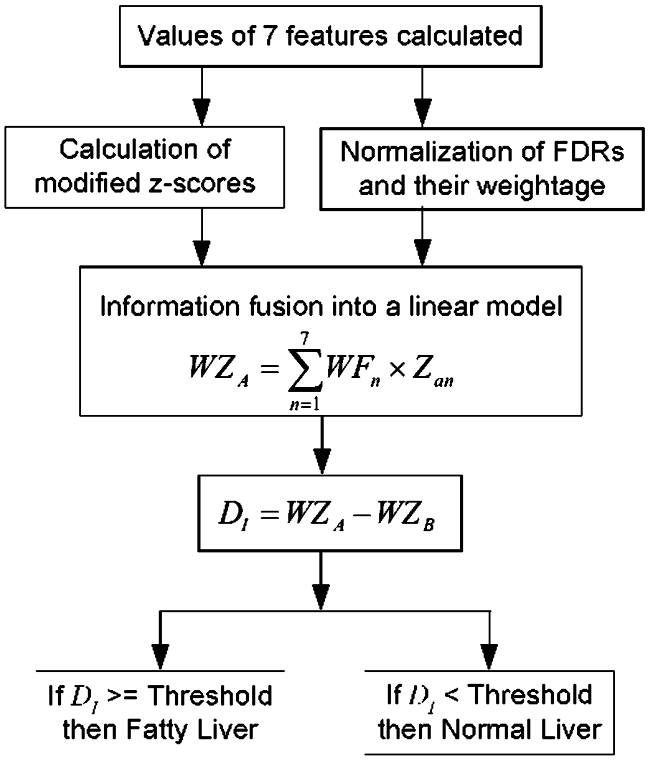

Figure 5.4 Proposed classification method

The proposed method contains only addition and multiplication operations, so it is mathematically simple, and therefore it does not need any specialized hardware or processor for realization. Thus the proposed method can be directly implemented on real time systems like ultrasound machines with available instrumentation.

5.5 RESULTS AND DISCUSSION

After selection of the best seven features, which can discriminate the fatty liver from normal liver, they are used to design the proposed method. The training set is used to get the best features, and their normalized weighted FDRs. A 5-fold cross validation is done for 5 times to find the optimal value of threshold for classification. In this approach, randomly five sets are made from 100 images, and four are picked for training and one is used for evaluation. This process is repeated five times, so that an optimal threshold value for D_I is found. Figure 5.5 shows the best threshold value of D_I is 1.35 for the available training dataset. Moreover, at this D_I value, the proposed method classifies all the fatty livers as 'fatty' and only four normal liver images are interpreted as 'fatty' liver. Since none of the fatty liver is misclassified (sensitivity is 100%) and the accuracy is also the highest at this threshold, therefore, this threshold is selected for classification.

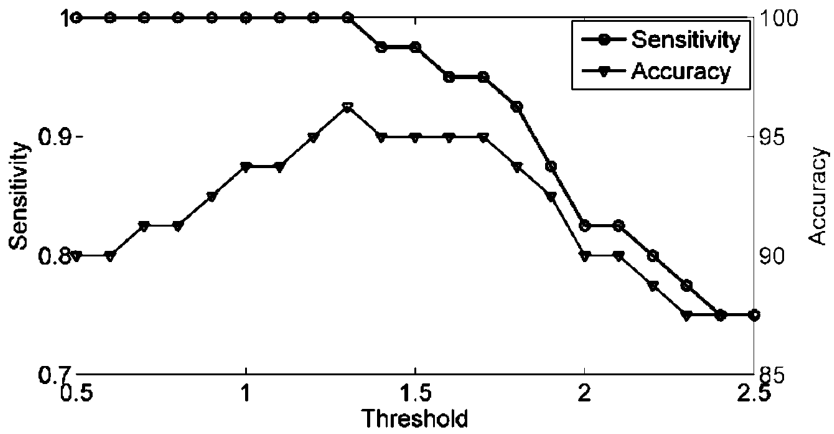

Figure 5.5 Accuracy and Sensitivity vs. Threshold values

To evaluate the performance of the proposed method, a separate dataset of 80 images is used. This dataset contains 40 fatty and 40 normal liver images, which were not the part of training set. As explained in Figure 5.4, the proposed classifier extracts only 7 features presented in the Table 5.4 and their modified z-score values are computed using equation 5.3. A test image is taken from the 'testing set' and the selected seven features are computed from the ROI of this image, and shown in the fourth column of the Table 5.4 (DENT is X1 = 0.098 and CNT X2 has its value = 0.061 and so on). The normalized weighted FDR is denoted by WF1 for the first parameter, and goes up to WF7 for seventh parameter in the third column. In the fifth column value of Za1 is calculated using equation 5.3. The sixth column of Table 5.4 is WZa1 to WZa7 using equation 5.4 and the column sum is WZA, calculated using equation 5.5.

In this typical example WZ_A = 0.821 and WZ_B = -1.782. Thus by equation 5.7, the final value of *discriminative index* D_I = 0.821-(-1.782) = 2.603. This numerical value of D_I is the final metric to classify liver, by comparing it with the threshold value. If D_I is greater than or equal to the threshold, then liver is fatty otherwise it is normal liver.

Table 5.4

Calculation of a test image as an example, where n = 1 to 7

S. No. (n)	Feature	Normalized Weightage of FDR (WF_n)	X_n (Sampled Value from test image)	Z_{an} (Eq. 5.3)	WZ_{an} (Eq. 5.4)	Z_{bn} (Eq. 5.3)	WZ_{bn} (Eq. 5.4)
1	DENT	0.303	0.098	0.910	0.276	-2.990	-0.906
2	CNT	0.261	0.061	0.978	0.255	-2.060	-0.539
3	ASM	0.126	0.490	0.197	0.096	-1.040	-0.131
4	H1	0.098	0.410	0.210	0.086	-0.950	-0.093
5	S_θ	0.084	2326.420	2.011	0.046	-0.580	-0.049
6	RGH	0.068	2.390	0.015	0.036	-1.530	-0.104
7	LE	0.060	5030.320	5.287	0.026	0.660	0.040
Total		1.000			WZ_A= 0.821		WZ_B = -1.782

5.5.1 Performance comparison

Usually, to evaluate a diagnostic method (test), the sensitivity and specificity analysis is used [117]. To emphasize the significance of feature fusion, the classifier is compared with individual texture models and with well-known classifiers using accuracy through the *sensitivity and specificity* test. Subsequently, the results have been also verified by the expert radiologists for each test image and then TP, TN, FP and FN are found and the *confusion matrix* is shown in Table 5.5.

Table 5.5

The Confusion matrix for the proposed method

		Predicted class	
		Positive	Negative
Actual class	Positive	40 (TP)	0 (FN)
	Negative	4 (FP)	36 (TN)

In medical diagnosis, misclassifying a benign tissue as a malignant tissue may not be a problematic. But if a malignant tissue is misclassified as benign tissue, that could be very crucial and should be avoided. As apparent from the Table 5.5, the proposed method does not give any '*False negative'* (FN) that is, there is no instance when 'fatty liver' is misclassified as 'normal', therefore the proposed method has a good acceptability as a diagnostic tool for radiologists.

The performance of the proposed method is compared with other well-known classifiers, and presented in Table 5.6. All the classifiers have been used for highest sensitivity. Performance evaluation is done on the basis of the 'classification accuracy' and 'average time consumed for classification'.

Table 5.6

Classification accuracy of different classifiers

Sr. No.	Classifier	Accuracy
1	Fuzzy Neural Network	82.5%
2	SVM (RBF kernel) [29]	90.0%
3	Back propagation NN [114]	91.2%
4	Fuzzy kNN [114]	93.7%
5	Proposed	95.0%

As shown in the Table 5.6, the proposed method has better accuracy than other classifiers. Moreover, the proposed method is based on a linear equation consisting of multiplications and additions only, therefore its computational complexity is low and it takes less time for classification. To further validate the results on optimal features, sequential forward search method has been used with the proposed method. In this study all the 35 features have been used with the proposed information fusion based method and sequentially one feature is removed in each iteration and classification accuracy is computed. The feature is removed such that the accuracy is highest. It has been found that the maximum accuracy is achieved when the seven selected features were used with the proposed information fusion based classification method.

5.6 SUMMARY

In this chapter, a liver classification method is proposed using fusion of features from different domains. The present study illustrates the following two points. First, the best texture features are identified for liver classification. Second, using the concept of information fusion, a new classification method is proposed, which is a linear combination of features, weighted with their class separation ability. Finally, a new index 'D_I' is proposed which can assist the radiologists to classify the liver. The main advantage of the proposed method is that, in spite of its inherent simplicity, the accuracy is 95% at 100% sensitivity, which is better or at least comparable with existing classifiers. The proposed method may further be extended is for sub-classification of fatty liver as 'low', 'moderate' and 'severe'. The proposed method can also be explored for other general classification problems, if annotated dataset is available.

CHAPTER-6

SVM BASED LIVER TISSUE CHARACTERIZATION

6.1 INTRODUCTION

Fatty liver is a state of liver, when the fat content of the '*hepatocytes*' increases more than 5% of the total '*hepatocytes*'. This fat accumulation is distributed throughout the liver and thus it is also called diffuse liver disease. The extent of fat accumulated in the liver is more important than presence of fat in the liver because it helps the physician to decide the treatment plan. However if the level of fattiness is more than the permissible limits, it may cause some chronic or fatal ailments like fibrosis and subsequently cirrhosis. Therefore it is very important to classify the level or grade of the fatty liver after diagnosis. In this chapter, a computer aided liver characterization method is presented, which is able to characterize the fatty liver as '*mild fatty*', '*moderate fatty*' and '*severe fatty*' from the ultrasound images.

6.1.1 Physiological Background of Fatty Liver Grading

Fatty liver is diagnosed by the radiologists from the increased echogenicity and unclear diaphragm boundary [118]. It is further classified into three different grades or categories: Grade 1 or mild fatty (5% to 33% of hepatocytes affected), Grade 2 or moderate fatty (33% to 66% of hepatocytes affected) and Grade 3 or severe fatty (more than 66% of hepatocytes affected) [119, 120]. Usually the radiologists compare the liver brightness with that of right kidney. The ratio of grey level intensity of liver and kidney is known as 'Hepato-renal' index [31, 121]. Early detection of moderate fatty or severe fatty may lead to better treatment for the patient. Subjective evaluation of diffuse liver, based on echo intensity (echogenicity) and spatial pattern of echoes (texture) is inaccurate [122]. The visual examination of ultrasound images to characterize the diffuse liver has limited accuracy [2]. Moreover, liver enzymes are insensitive and are not reliable to be used as an alternative to biopsy for confirm diagnosis of fatty liver, therefore a non-invasive complimentary diagnosis tool is need of the hour.

Tissue characterization of fatty liver (liver grading for physicians) has been done to help the physician for treatment planning and further investigations. Visual grading of fatty liver by radiologists/physicians has been done on the basis of liver surface texture (brightness and grey level variation), echo penetration and visibility of diaphragm with respect to liver. The most common observations used by the radiologists / physicians/researchers to characterize the fatty liver are listed in Table 6.1 [123].

Table 6.1

Fatty liver grading with respect to texture and diaphragm visibility

Features	Grade	Definition
Liver echo-texture	Normal	Normal: echo level of the liver parenchyma is homogeneous and no difference in contrast between liver parenchyma and kidney parenchyma.
	1	Mild fatty change: slightly increase in echo pattern of the liver
	2	Moderate fatty change: intermediate between score 1 and 3
	3	Severe fatty change: gross discrepancy of the increased hepatic to renal cortical echogenicity
Echo penetration and visibility of diaphragm	Normal	Normal: liver structure is clearly defined from the surface to the diaphragm. The outline of the diaphragm is clearly visualized
	1	Mild fatty change: mild attenuation of sound beam through the liver
	2	Moderate fatty change: intermediate between score 1 and 3
	3	Severe fatty change: marked attenuation of sound beam through the liver. The diaphragm is not visualized

Since the extent of fat accumulation increases from grade 1 to grade 2 and then grade 3, thus the echogenicity also increases in the same way from grade 1 to grade 3. However, the grade 3 fatty liver has poor or no visualization of the diaphragm, the intra-hepatic vessels, and posterior portion of the right lobe along with significant increased echogenicity. [49, 50]. The quantitative analysis of diaphragm visibility is a cumbersome task and not very accurate, therefore, echogenicity and the liver echo-texture methods are used in computer aided systems to characterize the liver tissue [105, 121]. Moreover some significant changes in liver surface also occurs in grade 2 and grade 3 fatty liver, and these changes have been evaluated through texture analysis [25]. In the present study these same methods are used to characterize the liver steatosis.

6.2 PREVIOUS WORK IN LIVER TISSUE CHARACTERIZATION

6.2.1 Ultrasound Tissue Characterization

The ultrasound quantitative tissue characterization is an image processing technique, which reveals the hidden patterns to extract more information about tissue function and pathology than it is being observed through visual analysis [93]. Initial research in the area of tissue characterization to detect cirrhosis in the liver, had been done by Wells and Mountford [107, 108]. In a significant research by Chivers and Hill, a scientific technique is used to retrieve the quantitative data from the tissue using scattering [125]. Since then, this branch of medical ultrasound has undergone considerable development. A lot of methods for Ultrasound Tissue Characterization (UTC) have been proposed and they are broadly classified into three categories, as shown in Figure 6.1 [126]. These characterization techniques are (i) Radio Frequency (RF) analysis using spectral analysis of RF signals, (ii) Elastography of the tissue and (iii) Texture analysis of ultrasound images. The first category is based on RF signals that are received from the beam former before they fetched to display system.

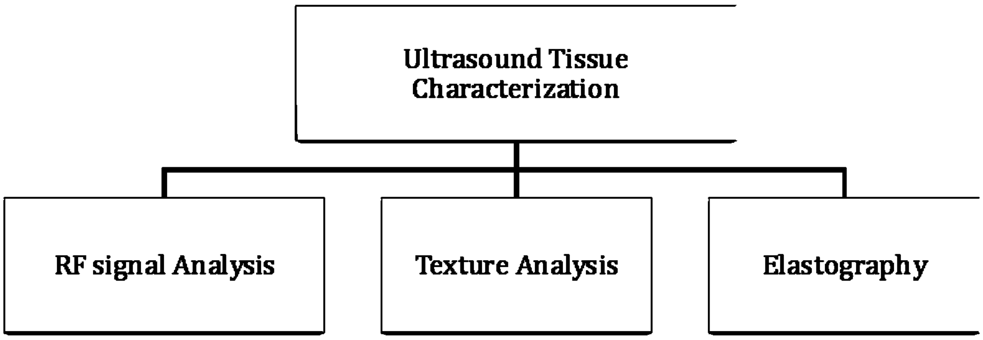

Figure 6.1 Ultrasound tissue characterization methods [126]

The second category is tissue characterization through *elastography.* In this imaging process brightness of the image depends upon the stiffness of tissue. An ultrasound probe emits vibrations that cause a shear wave in the liver, which corresponds to liver stiffness [127]. In another study, Fukuzawa et al. measured liver elastography in patients with biopsy proven Non Alcoholic Steato-Hepatitis (NASH) and demonstrated that liver elasticity is able to predict the fibrosis [128]. However, this method has a limited sensitivity and specificity, as shown by the Lewis. According to him, the modality was able to differentiate various stages of liver fibrosis with sensitivity of 86% and specificity of 85% [127]. Although RF signal based liver tissue characterization is used by number of researchers [20, 129, 130], but most of the researchers have used the third type of tissue characterization technique for liver; the texture analysis [25, 32, 33, 36, 38, 96, 131]. The main reason for this choice is that, when steatosis occurs, the liver surface changes significantly changed. This variation in the surface of liver makes the texture analysis a suitable tool to analyze this organ. Moreover, the texture analysis is directly related to the visual features in the ultrasound image, and radiologists are comfortable to correlate the texture features with the visual information. The texture analysis is very useful to characterize the liver because of its size and the quasi-periodic scattering structures found throughout the healthy tissue [131]. It has been established that, texture analysis based liver classification and liver tissue characterization methods outperform other techniques [32, 33, 36, 38]. Therefore, in this thesis, only texture based features have been used for tissue characterization of fatty liver into further three grades.

6.2.2 Methods for Liver Tissue characterization

With the popularity of Computer Aided Diagnosis in medical imaging, a lot of computerized classification methods have been used for fatty liver characterization. These methods include k-Nearest Neighbor (kNN), Artificial Neural Network (ANN), Fuzzy logic, Neuro-Fuzzy System (NFS), Support Vector Machines (SVM), Naive - Bayesian and many other state of the art classifiers for tissue characterization. Yajima et al. tested performance of various classifiers for liver tissue characterization [109].

Several researchers diagnosed diffuse liver diseases based on ultrasound images assisted by computerized tissue classification. Ogawa et al. introduced an ANN based technique for classifying diffuse liver disease such as chronic active hepatitis and liver cirrhosis [132]. They extracted FPS and SGLCM features from each ROI and then mean of the five ROIs had been used for further analysis. Wu and Chen proposed a multi-resolution fractal feature based on wavelet decomposition for detecting three sets of ultrasonic liver images: normal, hepatoma and cirrhosis [22, 133]. Kadah et al. confirmed the importance of the choice of classification techniques on the correct classification rate for normal, fatty and cirrhotic liver [25]. They used most discriminating features for classification and compare both statistical and neural classifiers. Soder et al. have conducted a study "Computer assisted ultrasound analysis of liver echogenicity in obese and normal weight children" [134]. In this study they proposed a hepato-renal index to quantify the echogenicity. In their method they computed the mean grey level of ROI from liver and ROI from the right kidney. Subsequently they calculated the difference between these two mean grey levels and termed it as "hepato-renal index". They reported that this index is a quantitative tool to differentiate between normal and fatty liver. Webb et al. proposed a hepato-renal index on the basis of the ratio between the echogenicity of the liver and that of the right kidney cortex using histogram echo intensity [31]. This method was able to identify the presence of less than 5% fat accumulation in the liver. They also proved that the quantitative assessment of 'echogenicity' is correlated ($r=0.82$, $p<0.001$) with histologic evaluation. Acharya *et al.* proposed a computer aided system (Symtosis) in which they utilized a novel combination of significant features to classify normal and fatty liver with 95% accuracy [32]. Recently, Singh et al. proposed a method to classify the liver by combining optimal features from Texture, Frequency and Fractal domains through information fusion having accuracy of 95% with 100% sensitivity [36].

A consolidated review of existing methods for liver tissue characterization has been presented in the Table 6.2.

Table 6.2

Consolidated review of existing liver classifiers

Sr. No.	Authors (Year)	Feature	Classification Method(s)	Results / Remarks
1	Yajima (1983)	Contrast	kNN, Fuzzy-kNN, SVM	Fatty – Normal
2	Layer (1991)	RF Attenuation	Neural Network	Fatty – Normal
3	Wu Chen (1992)	Wavelet, Fractal	LDA	Normal, Hepatoma, Cirrhosis
4	Kadah (1996)	Texture	ANN, kNN and Fuzzy NN	Fatty – Normal
5	Ogawa (1998)	Texture (SGLCM, FPS)	ANN	Normal, Cirrhosis, Chronic Hepatitis
6	Yeh (2003)	Texture, Non separable Wavelet	SVM	Grading of fibrosis
7	Wang (2004)	Texture	SOM, ANN	Fatty – Normal
8	Jeong (2005)	Wavelet and Texture features	PCA-SVM	Fatty – Normal
9	CAO (2005)	Texture (SGLCM, Fractal)	FDR, SVM	Normal- Fibrosis
10	Mukherjee (2007)	Texture features	Self organizing Map (SOM)	Fatty – Normal
11	Li (2008)	SGLCM	SVM	Fatty – Normal
12	Webb (2009)	Texture (Brightness)	Ratio of mean grey level liver and kidney	Fatty liver grading
13	Soder (2009)	Texture (Brightness)	Ratio of mean grey level liver and kidney	Fatty – Normal
14	Mancini (2009)	Texture (Contrast)	Hepato-Renal ratio	Fatty – Normal
15	Semra (2011)	Mean grey level	Grey relational classifier	Fatty liver Grading
16	Ribero (2012)	Texture, RF and wavelet based features	Bayes, kNN and SVM	Fatty – Normal
17	Acharya (2012)	Texture models and Wavelet	Data Mining	Fatty – Normal
18	Wu (2012)	SGLCM, Fractal, wavelet	1. GA based feature selection 2. kNN, Fuzzy kNN SVM	Fatty – Normal
19	Minhas (2012)	Wavelet	SVM	Fatty – Normal
20	Singh(2013)	Texture Features	Information Fusion	Fatty – Normal
21	Wang (2013)	Texture (Contrast)	Hepato-Renal ratio	Fatty liver grading

Most of the previous methods are fairly accurate but they could only classify the liver in normal or fatty. However, Semra et al. proposed a method for fatty liver grading using '*grey relational analysis*' and considered the right kidney as reference for the analysis [33]. Their method works well for liver characterization, however the accuracy to characterize the Grade 2 cases is limited. Thus, there is a need of quantitative and more accurate CAD method to assist the radiologists for liver tissue characterization. A method to further characterize the fatty liver into three different grades has been proposed in this thesis.

6.3 SVM BASED FATTY LIVER CHARACTERIZATION USING AMALGAMATED FEATURES (PROPOSED METHOD 2)

6.3.1 Hepato-Renal Index

The idea of liver–kidney contrast ratio was introduced by Yajima et al., and they have shown that the accuracy of this method is more than 90% to classify the normal and fatty liver [109]. The idea of taking the ratio of features from liver and kidney, later on used by Webb et al., and termed it '*hepato-renal'* index. They compared the mean grey level of an ROI from liver (Hepato) with the mean grey level of an ROI from kidney (renal cortex). Interestingly, the radiologists also do the same thing by visual comparison for fatty liver characterization, with assumption that kidney of the patient is normal. Although, this technique of liver-kidney ratio, has been presented earlier by several other researchers [137-140] but the term 'hepato-renal' index has proposed by Webb et al [31]. Recently Wang et al. studied the 'hepato-renal' ratio of *contrast* feature for diagnosis of steatosis and revealed that the method has high accuracy for moderate (Grade 2) to severe fatty (Grade 3) cases [141]. Recently it has been established that texture models like Spatial Grey Level Co-occurrence Matrix (SGLCM), Statistical Feature Matrix (SFM), Law's Texture Energy Measure (TEM) and Fractals Fractal features (FF) are very useful in classification of fatty liver [36]. However, features from SGLCM and SFM texture models are very sensitive to the grey level in the image. While acquiring the ultrasound image, usually the radiologist varies the TGC settings for better visual analysis. This variation in machine settings causes change in average gray level among different ultrasound images. Therefore the classification methods which are using 'grey level' based texture features, are prone to such errors. To overcome this drawback, ratio of features from liver and kidney is taken for these grey level based features. In this study, the idea of 'hepato-renal' index is further augmented with ratio of more features (CNT, RGH, ASM, and DENT). In addition to these features, only liver ROI values of four non grey-level based features (H1, S_{θ}, LE and DM4) are also used with SVM classifier.

6.3.2 Feature Extraction

In this study, images were acquired by experienced radiologists, in such a way that in each image, both liver and right kidney is visible. All images are acquired as per the protocol explained in chapter 2. Total 240 images were acquired (80 Normal, 80 Fatty grade-1, 40 Fatty grade-2 and 40 images of Fatty grade-3) and then annotated by the radiologists. The image database is divided into two groups; one for training consisting of 120 and other 120 images for testing. Further detail of these images is presented in Table 6.3. Since ratio of liver features and kidney features have to be studied, therefore, each image was acquired in such a way that both liver and right kidney is available in each image as shown in Figure 6.2. An experimental study has been done (presented in chapter 4) to select optimal size, shape and the location of the ROI. For reliable results, three ROIs of 30x30 pixels are selected from liver and one ROI of 20x20 pixels size is selected from kidney as shown in Figure 6.2.

Table 6.3

Detail of dataset images used for the study

Dataset	**Normal liver**	**Fatty liver images**			**Total**
		Grade 1	Grade 2	Grade 3	
Training set images	40	40	20	20	120
Testing set images	40	40	20	20	120
Total	80	80	40	40	240

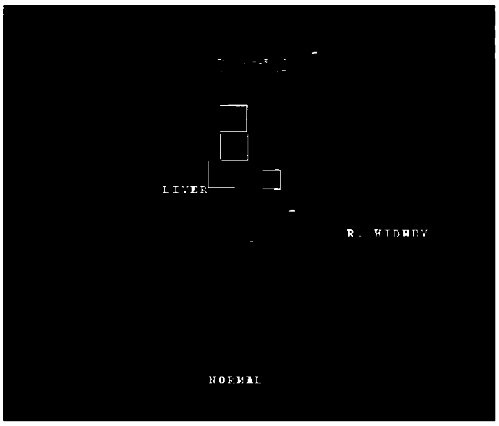

(a)

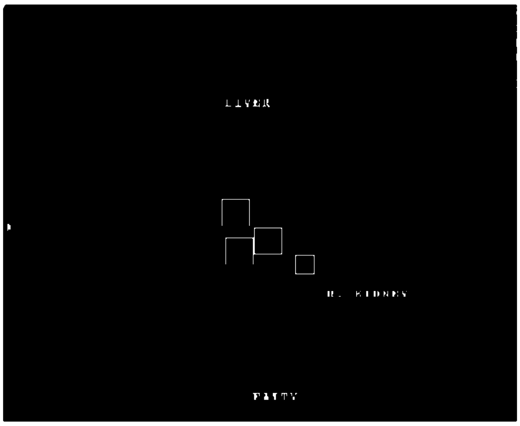

(b)

(c)

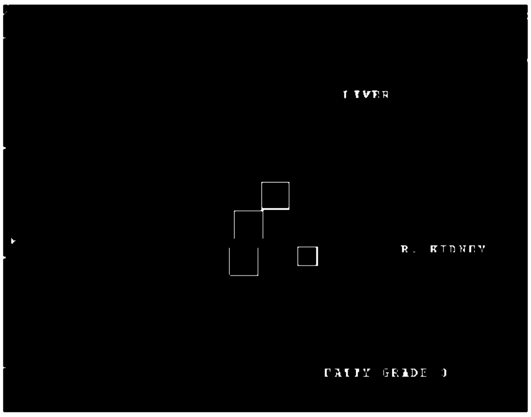

(d)

Figure 6.2. Feature extraction from liver and kidney using ROI near the centre line from an annotated image (a) Normal liver image (b) Fatty grade 1 (c) Fatty grade 2 (d) Fatty grade 3

It has been established that for liver tissue characterization from ultrasound images, texture analysis is the most useful method [133, 142]. Singh et al. proposed 7 most useful texture features from SGLCM, Fractals features, FPS, SFM and Law's TEM for liver classification into normal and fatty liver [36]. Recently, Acharya et al. has proposed a new features for liver tissue characterization; Short Run-length Emphasis (SRE) taken from Grey Level Run-length Matrices (GLRM) and 'DM4' from Discrete Wavelet Transform (DWT) [32]. To make a better characterization method, these latest features are also studied and the list of total features used in this study is presented in the Table 6.4.

Table 6.4

List of selected features for fatty liver characterization

Sr. No.	**Feature(s)**	**Texture Model**
1	DENT	SGLCM
2	CNT	
3	ASM	
4	SRE	GLRM
5	RGF	SFM
6	S_θ	FPS
7	H1	FF
8	LE	TEM
9	DM4	DWT

6.3.3. Proposed Method

Most of the previous methods based on hepato-renal ratio used for liver tissue characterization, considered contrast or mean grey level. In the present study, all the optimal features are analyzed to characterize the liver tissue using hepato-renal ratio and it has been found that if grey level based features are used in hepato-renal ratio, then the final accuracy of fatty liver characterization increases. Novelty of this method is that, grey level based features of liver are compared with same features of the kidney in the same image and thus, quality of the image does not affect the final classification. This makes the proposed method independent of machine settings. Stepwise approach for the proposed methodology is shown in Figure 6.3

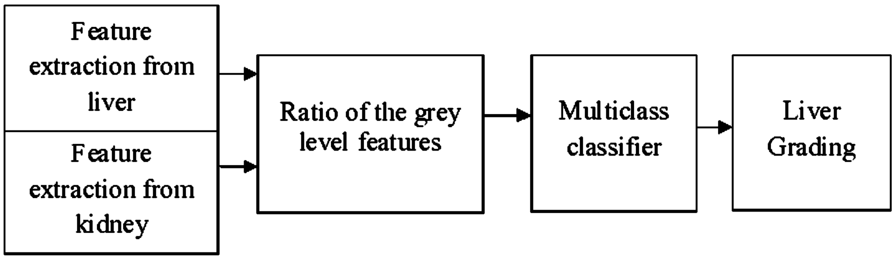

Figure 6.3. Block diagram of the methodology used

In the first step, all previously discussed nine features were extracted from each ROI from liver and kidney. The average value of each feature from three ROIs of liver is computed and the ratio is calculated with same feature taken from the ROI of right kidney. In this way, the texture of right kidney is taken as reference for grey level based texture features. Analysis of all the features has been done to examine their discriminative power considering them hepato-renal in ratio as well as without ratio. Box plots are used to analyze the ability of a feature to characterize the different grades of the liver. Only those features are selected in hepato-renal ratio, whose class separation ability has improved after the ratio otherwise value from the liver ROIs is considered without ratio. After selecting the appropriate features for hepato renal ratio, different classifiers are used for liver tissue characterization using the above said nine features. Six well known classifiers were used to characterize the liver and each classifier is tuned to have the highest sensitivity. The results are presented in the next section.

6.4 RESULTS AND DISCUSSION

6.4.1 Box Plot Analysis

All the nine features were used in three groups. First, when nine aforesaid features are used with liver values only, and second, when all features are used having ratio with their corresponding kidney values and third, when ratio of selected features is used. The impact of taking the ratio of grey level based features has been shown in figures 6.4 to 6.7. Figure 6.4 shows that discriminative power of CNT feature for the liver characterization using the hepato-renal ratio is better than without ratio (values only from the liver ROIs has been taken). In Figure 6.4 a box plots of normal and fatty liver (G1, G2, G3) are quite separable however, the discrimination between the grades of fatty liver is not very good, especially the grade 1 and grade 2 are overlapping. However when the ratio of liver and kidney is taken for CNT then the class separation for each category becomes clearer and thus the accuracy increases to characterize the liver as depicted from the Figure 6.4b. Similar observations have been made for the feature RGH, ASM, DENT and SRE, whose ratio increases the ability of class separation. Although the box plots have been made for all the features but only four of them are presented due to similar observations.

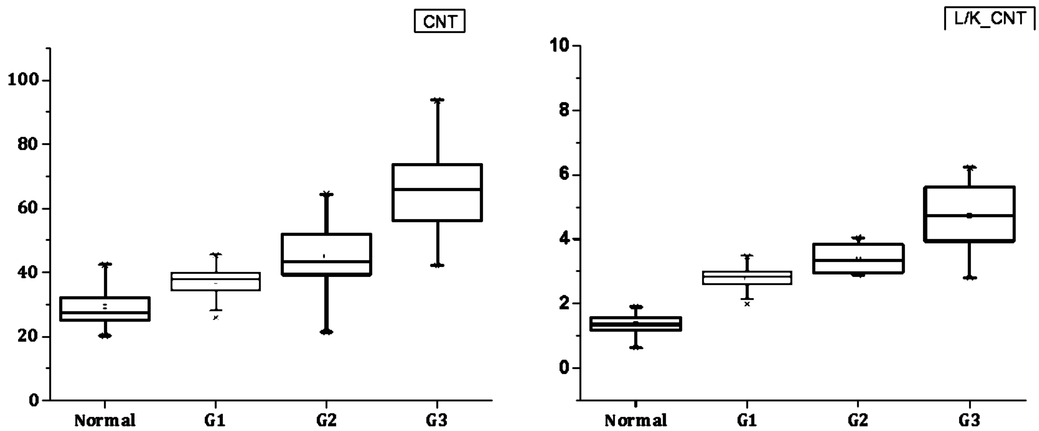

(a) (b)

Figure 6.4 Box plot of CNT feature. (a) CNT of liver only (b) after taking the ratio of liver CNT with kidney CNT.

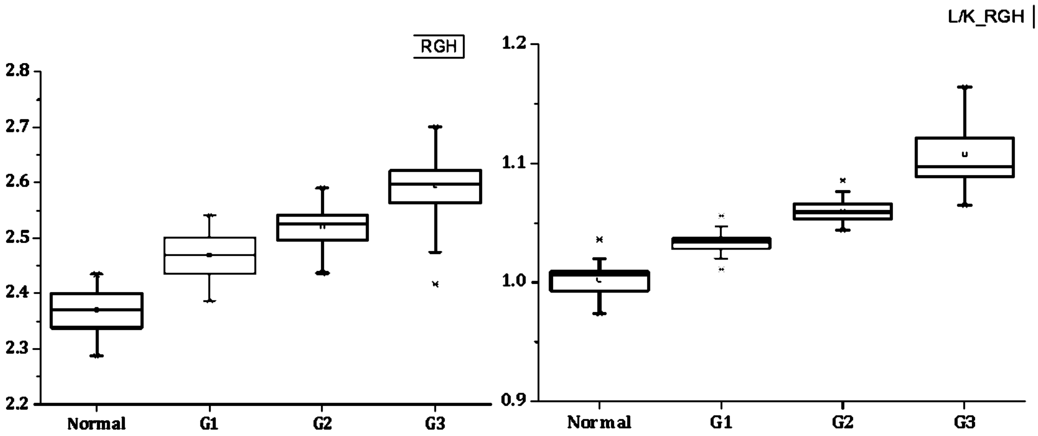

Figure 6.5 Box plot of RGH feature. (a) RGH of liver only (b) after taking the ratio of liver RGH with kidney RGH.

However in case of other features like H1, S_θ, DM4 and for Law's TEM feature 'LE' the trend is reverse, that is when hepato-renal ratio is used as a single feature, their ability to characterize the fatty liver reduces. As shown in Figure 6.6a and 6.7b, the class separation ability of these feature decreases when ratio of these features is used and the box plots starts overlapping. In fact they perform well without taking the liver kidney ratio. The possible reason that only these five features have better performance when considered as hepato-renal ratio is that, these five features are based on grey level of the neighboring pixels.

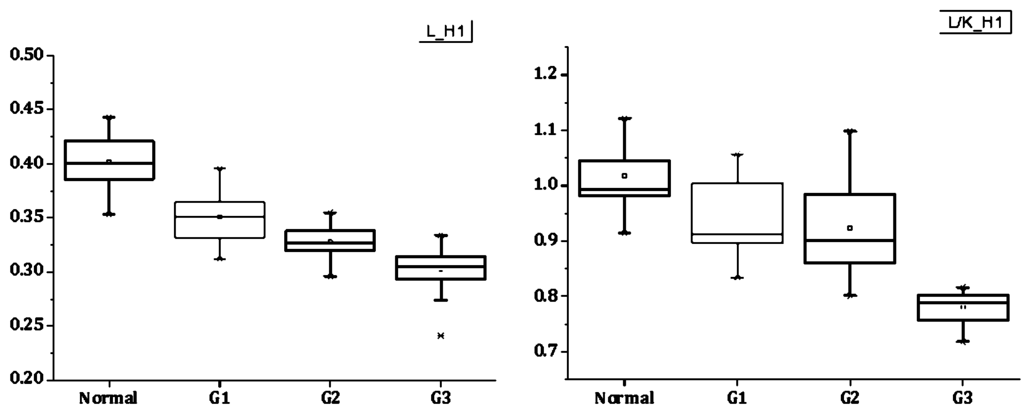

Figure 6.6 Box plot of H1 feature. (a) H1 of liver only (b) after taking the ratio of liver H1 with kidney H1.

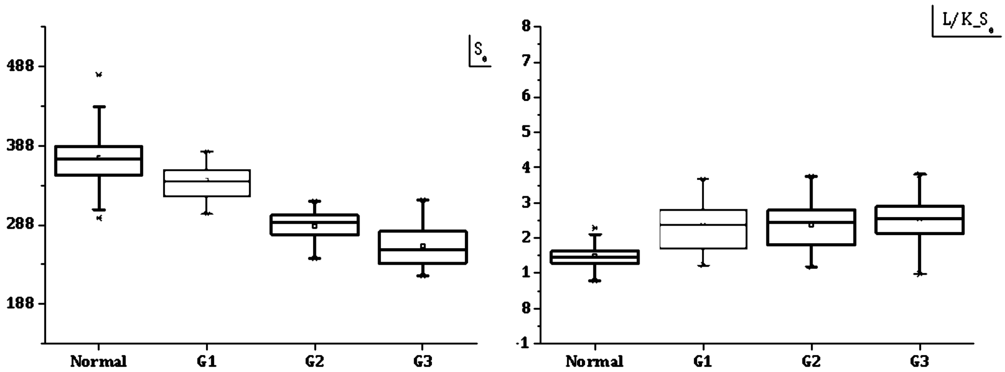

Figure 6.7 Box plot of S_θ feature. (a) S_θ of liver only (b) after taking the ratio of liver S_θ with kidney S_θ.

With the change in machine settings, the average grey level of the image changes and therefore, values of these features also varied which ultimately affects the classification accuracy of the classifier based on these features. However in case of frequency based features like H1 , S_θ , DM4 and for Law's TEM feature 'LE' this criteria is not true, because these features are not sensitive to the grey level but to the orientation, granularity and structure similarity. When classifiers were analyzed by using the ratio of all nine features, then the results were not encouraging. The reason may be that, the features which are independent of grey level in an image, but sensitive to liver texture, the discrimination power of such features is decreased when their ratio with kidney is used. Therefore the ratio of only those features has been used, which are grey level dependent. To consolidate the results, Table 6.5 is presented, which shows that whether the features are used in hepato-renal ratio or without ratio directly from the liver ROIs.

Table 6.5

Features used with and without hepato-renal ratio

Features with hepato-renal ratio (liver and kidney)	DENT, ASM, CNT, SRE and RGH
Features from liver only	H1, DM4, LE and S_θ

6.4.2 Analysis of Classifiers

All the nine features listed in the Table 6.4, have been used with different classifiers. In this study six classifiers were used for evaluation of the selected features for fatty liver grading. These classifiers are most commonly used by the previous researchers for the liver tissue characterization. The classifiers are Naïve Bayesian, 'k' nearest neighbor (kNN), Artificial Neural Network (ANN), Information Fusion based [36], and Support Vector Machine (SVM). Results in terms of confusion matrix of each classifier are presented in from the Tables 6.7 to 6.11. The best results for each classifier have been shown, keeping the sensitivity of the classifier at maximum value.

All the classifiers are evaluated using multiclass confusion matrix shown in Table 6.6. Actual classes are represented row-wise from top to bottom and the predicted class by the classifier is presented column wise from left to right. The term $C_{N\text{-}N}$ signifies the number of correctly classified normal liver images. The term $M_{N\text{-}G1}$ signifies the number of miss-classified images as grade 1, which actually were from normal liver. Similarly other notation are used which are self explanatory. Class accuracy is the percentage of correctly classified image out of the total images for a given class. Finally the overall accuracy is computed for the classifier, which indicated the percentage of total correctly classified images out of all the images tested with that classifier.

Table 6.6

Multiclass confusion matrix to evaluate the classifier

		Predicted Class					
		Normal	**G1**	**G2**	**G3**	**Class Acc**	**Overall Acc**
Actual Class	**Normal**	C_{N-N}	M_{N-G1}	M_{N-G2}	M_{N-G3}		
	G1	M_{G1-N}	C_{G1-G1}	M_{G1-G2}	M_{G1-G3}		
	G2	M_{G2-N}	M_{G2-G1}	C_{G2-G2}	M_{G2-G3}		
	G3	M_{G3-N}	M_{G3-G1}	M_{G3-G2}	C_{G3-G3}		

(a) Naive Bayesian Classifier

All the selected features are passed on to the Naive Bayesian classifier, and the results are presented in the Table 6.7. The results indicate that the classifier is able to correctly classify 37 normal images out of 40 images. Similarly results for other classes are also shown. The significant observation for this classifier is that, 3 cases of G1 are reported as G3 and 1 case of G3 is misinterpreted as G1. The later condition is not acceptable to the radiologist, that is a severe fatty liver should not be characterized as a mild grade fatty liver, as this will lead to missing a fatal disease. Moreover, the overall accuracy of this classifier is only 85.8% that is 103 out of 120 images have been correctly classified.

Table 6.7

Confusion Matrix of Naïve Bayesian Classifier

		Predicted Class					
		Normal	**G1**	**G2**	**G3**	**Class Acc(%)**	**overall Acc(%)**
Actual Class	**Normal**	37	3	0	0	92.5	85.8
	G1	0	32	5	3	80.0	
	G2	0	1	16	3	80.0	
	G3	0	0	2	18	90.0	

(b) The kNN Classifier

The next classifier tested is k- Nearest Neighbor (kNN) classifier. Different values of 'k' were used but the 'k=3' has the best results and Table 6.8 for the same has been shown here. The performance of kNN classifier was better as compared to the Naïve Bayesian classifier, as it has correctly classified all normal images. Moreover the grade 2 images were not misclassified as grade 1 or normal, which is acceptable to the radiologists , however the class wise accuracy for grade 2 is only 80%. This classifier has the overall accuracy of 92.6%.

Table 6.8

Confusion Matrix of kNN Classifier

	Predicted Class						
		Normal	**G1**	**G2**	**G3**	**Class Acc (%)**	**Overall Acc (%)**
Actual Class	**Normal**	40	0	0	0	100	92.6
	G1	0	37	2	1	92.5	
	G2	0	0	16	4	80	
	G3	0	0	2	18	90	

(c) The Neural Network Classifier

The state of the art neural network based classifier is also analyzed with same set of nine features. Back propagation method was used and the optimal parameter settings were used to get the highest sensitivity. The confusion matrix has been shown in the Table 6.9. This classifier is even better than Naïve Bayesian and kNN classifier. The Nueral Network classifier has class wise accuracy of 100%, 95%, 90% and 95% for normal, grade 1, grade 2, and grade 3 respectively and the overall accuracy is 95.8%.

Table 6.9

Confusion Matrix of Neural Network Classifier

	Predicted Class					
		Normal	**G1**	**G2**	**G3**	**Class Acc (%)**	**Overall Acc (%)**
Actual Class	**Normal**	40	0	0	0	100	95.8
	G1	0	38	1	1	95	
	G2	0	0	18	2	90	
	G3	0	0	1	19	95	

(d) The Information Fusion based Classifier

Information Fusion based classifier (proposed method 1) was used and the threshold value of the discriminative index D_I is selected to keep the maximum sensitivity of the classifier. This fact is clear from the Table 6.10, as none of the fatty liver is misclassified as normal. Moreover, the overall accuracy of the classifier is 96.7%, which is best as compared to Naïve Bayesian, kNN and NN classifiers. Individual class prediction rate for grade 1 is also best among these classifiers. For grade 2 and grade 3, the classification accuracy was found to be same as that of NN but higher than Naïve Bayesian and kNN .

Table 6.10

Confusion Matrix of Information Fusion Classifier

	Predicted Class						
		Normal	**G1**	**G2**	**G3**	**Class Acc (%)**	**Overall Acc (%)**
Actual Class	**Normal**	40	0	0	0	100.0	96.7
	G1	0	39	1	0	97.5	
	G2	0	0	18	2	90.0	
	G3	0	0	1	19	95.0	

(e) Proposed SVM Classifier

The proposed method utilized the SVM classifier with 'polynomial' kernel, as for the Radial Biased Function (RBF) kernel results were not encouraging. In case of the polynomial kernel, third order polynomial has been used and the coefficients are adjusted to get the maximum sensitivity. As depicted from the results given in the Table 6.11, the proposed method has 100% accuracy of classifying normal and fatty liver. The proposed method has 100% sensitivity for grade 1 and grade 3 also. In case of grade 2, only two images have been misclassified as grade 3. However this is acceptable, because the patients having fatty liver grade 2 and grade 3 are advised for further investigations and such type of misclassification is detected at later stage. However, if grade 3 is misclassified as grade 1, then it could be critical because the patient could not get the required treatment, which leads to more deterioration in the condition.

Table 6.11

Confusion Matrix of Proposed SVM Classifier

		Predicted Class					
		Normal	**G1**	**G2**	**G3**	**Class Acc (%)**	**Overall Acc (%)**
Actual Class	**Normal**	40	0	0	0	100	98.3
	G1	0	40	0	0	100	
	G2	0	0	18	2	90	
	G3	0	0	0	20	100	

To compare different classifiers in terms of the overall accuracy, results of each classifier have been shown in the Table 6.12. All the classifiers have been tested with and without ratio of features. As evident from the last two columns of Table 6.12, overall grading accuracy of each classification method is better when liver to kidney ratio based features are used. Therefore the performance of each classifier is enhanced when ratio of grey-level based features is used. Moreover the best performance is shown by the SVM based classifier which has the accuracy of 98.3% with 100% sensitivity for three classes.

Table 6.12

Classification accuracy of different classifiers on 120 Test images

Sr. No.	**Classification method**	**Fatty liver grading Accuracy (%)**	
		Features from liver only	Proposed
1	Naive - Bayesian	80.8	85.8
2	kNN	90.0	92.5
3	Neural Network	86.6	95.8
4	Info-Fusion based	95.0	96.7
5	SVM (Proposed)	95.0	98.3

6.5 SUMMARY

All the previous 'hepato-renal' index based methods were very effective, but they were limited to classify the liver in normal or fatty only. The present study proposes a method to further characterize the fatty liver into different grades. Semra et al. (2011) proposed a method for fatty liver grading using 'grey relational analysis' and considered the right kidney as reference for 'grey relational analysis' [33]. But their accuracy is limited, especially in Grade 2 cases. However the proposed technique further augmented their idea in a novel way by combining the most significant features. Moreover by computing the ratio of grey level features (SGLCM, GLRM, SFM) and the use of SVM classifier, accuracy of liver grading is increased and the method become insensitive to machine settings also.

Novelty of this method is that, not only five grey level based features of liver are compared with same features of the kidney in the same image (to make the proposed method independent of machine settings) but four other features are also added in the SVM based classification method to increase the accuracy of tissue characterization.

The results show that if ratio of gray level based features like Contrast (CNT), Angular Second Moment (ASM), Difference of entropy (DENT), Short Run-length Emphasis (SRE) and Roughness (RGH) of liver to that of kidney are combined with four other features like Angular sum (S_θ), Hurst's coefficient (H1), Mean value of 4th mother wavelet (DM4) and LE extracted from liver, then fatty liver grading is better and more reliable. The reliability is due to the fact that the liver texture has its own reference surface texture (kidney) in the same image and therefore the method is insensitive to machine settings. The optimal set of features is used with multi-class SVM classifier for characterization of fatty liver. This method has 98.3% overall accuracy to characterize the fatty liver into its sub classes, which is found to be better than the other recent methods [31, 33, 36, 38, 50, 134].

CHAPTER-7

CONCLUSION AND SCOPE FOR THE FUTURE WORK

7.1 CONCLUSIONS

The overall objective of medical imaging is to acquire useful information about the physiological processes or organs of the body. Tissue characterization is an important process in medical imaging, because it helps the physicians to decide the treatment of a patient. Subjective evaluation of ultrasound images for liver tissue characterization is observer dependent and less accurate. In this thesis work, Computer Aided Diagnostic methods are proposed for ultrasound imaging to assist the radiologist in differentiating normal liver and fatty liver, and then further grading of the fatty liver. The present thesis work has five subparts; (i) ultrasound image enhancement (ii) feature extraction from ROI (iii) selection of optimal features (iv) liver classification method using optimal features and (v) SVM based liver characterization using hepato-renal ratio of features. To accomplish these tasks, two databases have been used. One database has been used to evaluate the proposed method for ultrasound image enhancement and it has been downloaded from the Pizurica's home page. The other database has been created by the authors to design and evaluate the liver characterization methods. This database has been created with the help of PGIMER Chandigarh and Delta Diagnostic Centre Patiala. Following are the major conclusions of the work carried out in this thesis.

7.1.1 Image Enhancement

1) Ultrasound images have inherent speckle noise, which makes the computer aided analysis and processing more difficult. Thus, in the first part, a speckle suppression technique is proposed to perform

the speckle suppression even very near to the edges using edge map and local statistics. This technique utilizes the local statistics in a moving window, to smooth or preserve the central pixel. A combination of 'coefficient of variance' (COV) and 'weighted mean' is included for better adaptation of the filter to check the true edges and isolated speckle noise in homogenous area. Subsequently, 'Edge map' is used to enhance the edges in the image after filtration. Evaluation of the proposed filter has been done quantitatively using image quality metrics and qualitatively through visual examination by medical experts also.

2) Quantitative analysis has been done on synthetic images and quality metrics such as Signal to Noise Ratio (SNR), Signal to Mean Square Error Ratio (S_MSE), Structural Similarity Index (SSI), Edge Preserving Index (EPI) and Correlation Coefficient (COC) have been used. The results of the study emphasize that the proposed technique enhances the efficiency of standard spatial filters for ultrasound images both in terms of speckle suppression and enhancement of edges.

3) The qualitative analysis has been done on the real ultrasound images by the panel of experienced radiologists through Mean Opinion Score (MOS). The experts were asked to assign a score in the 1–5 scale corresponding to low and high subjective visual perception criteria. Five is given to an image with the best visual perception. The fourth order partial differential equation (*fpde*) based filter has 3.46 and anisotropic diffusion based filter has 2.53, whereas the proposed method has the highest value of MOS as 4.26 out of 5. The results indicate that the proposed method is suitable for computer aided analysis of ultrasound images, as it preserves the diagnostically important information in the image.

7.1.2 Feature Extraction using ROI

1) The refined ultrasound images are further used to extract the features from Region of Interest (ROI). In Computer Aided Diagnostic system, when the ROIs are used to extract the features then accuracy of the system significantly depends upon the characteristics of ROI. Since liver is very large tissue, therefore, experiments were conducted to find the appropriate 'shape, size and location' of ROI. Different texture models have been used to extract features from these ROIs to have reliable analysis for appropriate size of the ROI. Each texture feature carries specific information about the tissue and the ability of retaining that information in different sizes is observed. Therefore an experimental analysis for selection of ROI is presented. Different sizes of 100x100 pixels, 75x75 pixels, 64x64 pixels, 50x50 pixels 40x40 pixels, 30x30 pixels, 25x25 pixels and 10x10 pixels have been considered.
2) It has been observed that 100x100 pixels and 75x75 pixels ROIs are not suitable for liver classification methods because they are big in size and usually contain blood vessels or bile duct. However ROIs of 10x10 pixels and 25x25 pixels are too small to have sufficient information to get a reliable statistical analysis from them. These small sized ROIs may be useful in case of cyst or small size tumor in liver but not suitable for the present study.
3) Finally the most popularly used ROIs of 64x64 pixels and 30x30 pixels ROIs have been analyzed using correlation coefficient and box plots. It has been found that the correlation coefficient is very high (0.99) among the data in these two sizes and the ability of class separation of each feature is similar in these two sizes. Therefore, the information content in 30x30 pixels ROIs is very

much similar to the 64x64 pixels ROIs. After the analytical study and discussions with radiologists, it has been examined that a square shaped ROI having size of 30x30 pixels is optimal, and it should be taken along (or near) the centre line of the image.

4) As suggested by the radiologists, multiple ROIs are selected from liver image near the centre. These multiple ROIs present the overall variation of the liver and leads to a reliable statistics for texture analysis, because large dataset is available. Moreover, smaller size multiple ROIs take lesser computational time than a single bigger ROI. The average value of each feature is computed from these multiple ROIs from an image to perform further analysis. The experimental study, which has been done to find optimal size of ROI for liver tissue characterization, is the first such study in this area till date.

7.1.3 Feature Selection

1) Once the texture features have been extracted from ROIs, then the next step is to select the most appropriate features for liver characterization and this process is called '*feature selection'*. To perform this task, Fisher's Discriminative Ratio (FDR), Box-Plot analysis and Pearson's correlation coefficient (PCC) are used. After the analysis on 35 features taken from different texture models, it has been found that the 7 most discriminative (highest FDR and maximum separation in Box plots) and independent (low PCC) features could be used for liver classification. These selected features are DENT, ASM, CNT, RGH, H1, S_θ and LE.

7.1.4 Information Fusion based Liver Classification (Proposed Method 1)

1) Feature selection is followed by the liver classification into 'normal' and 'fatty' liver. A novel classification method, based on

information fusion is proposed in this thesis, which gives a discriminative index (D_I) to classify the normal and fatty liver. This index considers the FDR of the feature as a multiplication factor to the value of the feature while calculation. In this way the highest FDR feature has the maximum impact on the value of D_I. The threshold value of D_I is selected in such a way that it has 100% sensitivity. In medical diagnosis, 100% sensitivity means that every diseased tissue/organ is correctly classified and it is highly desirable. The proposed information fusion based liver classification method has been compared with different classifiers like Fuzzy-kNN, Back propagation NN, SVM and Fuzzy neural networks. The Fuzzy kNN has 93.7%, Back propagation NN 91.2% accuracy and other methods have even less than this value, however the classification accuracy of the proposed method is 95% at 100% sensitivity. Thus the efficacy of the proposed method is better than the existing ones.

2) Although, this information fusion based classification method is proposed for medical diagnosis of liver, however the concept is universal and applicable to any other binary classification problem.

7.1.5 SVM based Liver Tissue Characterization (Proposed Method 2)

1) It is very important for a physician to know the level of fat accumulated in the liver to decide about the treatment of the patient. Therefore, fatty liver is further characterized into three grades; grade 1 or *mild* fatty liver, grade 2 or *moderate* fatty liver and grade 3 or *severe* fatty liver. The proposed method 2 is intended to perform this characterization.

2) Recently, some new texture features have been proposed for liver tissue characterization. These features have also been considered and again optimal features have been found. This makes the total

nine features for liver characterization which include seven earlier features and two new features; 'Short Run-length Emphasis measure' (SRE) and mean value of 4^{th} level wavelet using DWT (DM4).

3) In the information fusion based method, it has been observed that the features like DENT, ASM, RGH and CNT are dependent on the grey level of the image. Whenever the machine settings are changed, the mean grey level of the image also changes, which may vary the values of above said features. To address this issue, hepato-renal (Liver – kidney) ratio of these features has been used. Each of these grey level features has been computed from liver as well as kidney of the same image, and then their ratio is considered. This step automatically takes care of the effect of variation in the grey level due to machine settings, and the makes the method more accurate.

4) Previous researchers have used hepato-renal ratio of CNT feature only, but in the proposed, all grey level based features (DENT, ASM, RGH, SRE and CNT) have been considered for hepato-renal ratio. The remaining four features (H1, S_θ, DM4 and LE) have been used without ratio, considering their liver values only. This amalgamation of features has been tested on 120 with different state of the art classifiers like Naïve Bayesian, kNN, ANN, Information Fusion (proposed method 1) and SVM. The results indicate that when hepato-renal ratio of five grey level based features is used the classification accuracy of all the classifiers has increased.

5) The Naïve Bayesian has the overall liver tissue characterization accuracy of 85.8%, kNN has 92.5%, ANN has 95.8%, Information Fusion has 96.7% and SVM has 98.3%. The results demonstrate

that if ratio of CNT, ASM, DENT, SRE and RGH features of liver and kidney are combined with four other features extracted from liver only, then fatty liver grading is better and more reliable. The reliability is due to the fact that the liver texture has its own reference surface (kidney) is there in the same image and therefore the method is insensitive to machine settings. The proposed set of features in aforesaid combination performs best with multi-class SVM classifier for characterization of fatty liver. This method has 100% accuracy to characterize into its sub classes; normal liver (40/40), fatty liver grade 1 (40/40) and grade 3 (20/20), and 90% accuracy for grade 2 (18/20), making the overall accuracy of 98.3% (118/120), which is found to be better than all other recent methods. Novelty of this method is that, amalgamation of five hepato-renal features and four liver features makes the proposed method independent of machine settings and increases the accuracy of tissue characterization.

In conclusion, the present work is likely to contribute significantly to the area of medical image analysis. The methods developed will in particular be useful for liver tissue characterization.

7.2 SCOPE FOR FUTURE WORK

Suggested below are a few directions and challenges in which further work in the area of processing and analysis of ultrasound images can be taken up.

1. Presently, the ROI selection is manual, which requires significant experience and domain knowledge. In future, a system can be proposed to automatically select the ROI from an ultrasound image.
2. Although the machine dependence for liver characterization has been taken care of in hepato-renal method, but the information

fusion based method has a discriminative index D_I, whose threshold value is still machine dependent. In future this issue can be addressed to propose a more versatile D_I.

3. A combination of RF signal features and Texture features may results in better classification accuracy.
4. It may be a good idea to develop an expert system that may assist radiologist in taking decisions.

References

[1] S.P. Singh, S. Nayak, M. Swain, N. Rout, R.N. Mallik, O. Agrawal, C. Meher and M. Rao, "Prevalence of nonalcoholic fatty liver disease in coastal eastern India: a preliminary ultrasonographic survey", *Tropical Gastroenterology*, vol. 25 no. 2, pp. 76-79, 2004.

[2] E.L. Chen, P.C. Chung, C.L. Chen, H.M. Tsai and C.I. Chang, "An automatic diagnosis system for CT Liver image classification", *IEEE Transaction on Biomedical Engineering*, vol. 45 no. 6, pp. 783-794, 2002.

[3] J.S. Lee, "Refined filtering of image noise using local statistics," *Computer Graphics and Image Processing*, vol. 15, pp. 380-389, 1981.

[4] L. Busse, T.R. Crimmins and J.R. Fienup, "A model based approach to improve the performance of the geometric filtering speckle reduction algorithm," in *Proceedings of IEEE Ultrasonics Symposium*, pp. 1353-1356, 1995.

[5] D.T. Kuan, A.A. Sawchuk, T.C. Strand and P. Chavel , "Adaptive restoration of images with speckle," *IEEE Transactions on Acoustic Speech and Signal Processing*, vol. 35 no. 3, pp. 373-383, 1987.

[6] R. Perona and J. Malik , "Scale-space and edge detection using anisotropic diffusion", *IEEE Transactions on Pattern Analysis and Machine Intelligence*, vol. 12 no. 7, pp. 629-639, 1990.

[7] S. Jin, Y. Wang, and J. Hiller, "An adaptive non-linear diffusion algorithm for filtering medical images", *IEEE Transactions on Information Technology and Biomedicine, v*ol. 4 no. 4, pp. 298-305, 2000.

[8] Y. Yu and S.T. Acton, "Speckle reducing anisotropic diffusion", *IEEE Transactions on Image Processing*, vol. 11 no.11, pp. 1260-1270, 2002.

[9] Y.L. You and M. Kaveh, "Fourth Order Partial Differential Equations for Noise Removal", *IEEE Transactions on Image Processing*, vol. 9 no. 10, pp. 1723-1730, 2000.

[10] D. Mittal, V. Kumar, S.C. Saxena, N. Khandelwal, N. Kalra, "Enhancement of the ultrasound images by modified anisotropic diffusion method", *Medical and Biological Engineering and Computing*, vol. 48 no. 12, pp. 1281-1291, 2010.

[11] A. Achim, A. Bezerianos and P. Tsakalides, "Novel Bayesian multiscale method for speckle removal in medical ultrasound images," *IEEE Transactions on Medical Imaging,* vol. 20 no. 8, pp. 772-783, 2001.

[12] O. Michailovich and D.Adam, "Robust estimation of ultrasound pulses using outlier-resistant de-noising", *IEEE Transactions on Medical Imaging*, vol. 22 no. 3, pp. 368-381, 2003.

[13] S. Gupta, R.C. Chauhan and S.C. Sexana, "Homomorphic wavelet thresholding technique for denoising medical ultrasound images", *Journal of Medical Engineering & Technology*, vol. 29 no. 5, pp. 208-214, 2005.

[14] S. Gupta, L. Kaur, R.C. Chauhan and S.C. Saxena, "A versatile technique for visual enhancement of medical ultrasound images", *Digital Signal Processing*, vol. 17 no. 3, pp. 542-560, 2007.

[15] R.G. Dantas and E.T. Costa, " Ultrasound speckle reduction using modified Gabor filter", *IEEE Transactions on Ultrasonics, Ferroelectrics and Frequency Control*, vol. 54 no. 3, pp. 530-538, 2007.

[16] R. Wagner, S. Smith, J. Sandric and H. Lopez," Statistics of speckle in Ultrasound B-scans*", IEEE Transactions on Sonics and Ultrasonics*, vol. 30 no. 3, pp. 156-163, 1987.

[17] G.G. Lendaris and G.L. Stanley, "Diffraction pattern sampling for automatic pattern recognition", in *Proceedings of the IEEE*, vol. 58 no. 2, pp. 198-216, 1970.

[18] R.M. Haralick, K. Shanmugan and I.H. Dinstein, "Texture features for image classification", *IEEE Transaction on System, Man and Cybernetics,* vol. 3 no. 6, pp. 610-621, 1973.

[19] K.I. Laws, “Texture energy measures”, in *Proceedings of the Image Understanding Workshop*, pp. 47-51, 1979.

[20] J.M. Thijssen, “Ultrasonic speckle formation, analysis and processing applied to tissue characterization”, *Pattern Recognition Letters*, vol. 24 no. 4, pp. 659-675, 2003.

[21] R. Lu and Y. Shen, “Automatic Ultrasound image segmentation by Active contour model based on texture”, in *Proceedings of the first IEEE International Conference on Innovative Computing, Information and Control* (ICICIC ‘06), vol. 2, pp. 689-692, 2006.

[22] C.M. Wu, Y.C. Chen, and K.S. Hsieh, “Texture features for classification of ultrasonic liver images”, *IEEE Transactions on Medical Imaging*, vol. 11 no. 2, pp. 141-152, 1992.

[23] J.S. Weszka, C.R. Dyer and A. Rosenfield, “A Comparative Study of Texture Measures for Terrain Classification”, *IEEE Transactions on*

Systems, Man. & Cybernetics, vol. 6 no. 4, pp. 269-285, 1976.

[24] C.M. Wu and Y.C. Chen, "Statistical Feature Matrix for Texture Analysis", CVGIP: *Graphical Models and Image Processing*, vol. 54 no. 5, pp. 407-419, 1992.

[25] Y.M. Kadah, A.A. Farag, J.M. Zurada, A.M. Badawi, and A.M. Youssef, "Classification algorithms for quantitative tissue characterization of diffuse liver disease from ultrasound images", *IEEE Transactions on Medical Imaging*, vol. 15 no. 4, pp. 466-78, 1996.

[26] A.M. Badawi, A.S. Derbala, and A.M. Youssef, "Fuzzy logic algorithm for quantitative tissue characterization of diffuse liver diseases from ultrasound images", *International Journal of Medical Informatics*, vol. 55 no. 2, pp. 135 – 147, 1999.

[27] W.L. Lee, K.S. Hsieh and Y.C. Chen, "A study of Ultrasound Liver Image classification with Artificial Neural Networks based on fractal geometry and multiresolution analysis", *Biomedical Engineering: Applications, Basis and Communications*, vol. 16, pp. 59 – 67, 2004.

[28] D. Balasubramanian, S. Poonguzhali and G. Ravindran, "Automatic Classification of Focal Lesions in Ultrasound Liver Images using Principal Component Analysis and Neural Networks", in *Proceedings of 29th Annual International Conference of the IEEE EMBS,* Lyon, France, pp. 2134 – 2137, 2007.

[29] G. Li, Y. Luo, W. Deng, X. Xu, A. Liu and E. Song, "Computer Aided Diagnosis of Fatty Liver Ultrasonic Images Based on Support Vector Machine", in *Proceedings of 30th Annual International IEEE EMBS Conference*, Vancouver, Canada, pp. 4768-4771, 2008.

[30] R. Ribeiro and J. Sanches, "Fatty liver characterization and classification by ultrasound." in *Pattern Recognition and Image Analysis*, Springer Berlin Heidelberg, LNCS vol. 5524, pp. 354-361, 2009.

[31] M. Webb, H. Yeshula, S. Zelber, E. Santo, E. Brazowski, Z. Halpern and R. Oren, "Diagnostic value of a computerized heptorenal index for sonographic quantification of liver Steatosis", *American Journal of Roentgenology*, vol. 192 no. 4, pp. 909 – 914, 2009.

[32] U.R. Acharya, S. Vinitha, R. Ribeiro, G. Krishnamurthi, R.T. Marinho, J. Sanches and J.S. Suri, "Data mining framework for fatty liver disease classification in ultrasound: A hybrid feature extraction paradigm", *Medical Physics*, vol. 39, pp. 4255-4264, 2012.

[33] I. Semra, A. Coskun and T. Ikizceli, "Quantitative grading using Grey relational analysis on ultrasonographic images of a fatty liver", *Journal of Medical Systems*, vol. 36 no. 4, pp. 2521-2528, 2012.

[34] S. Strauss, E. Gavish, P. Gottlieb, L. Katsnelson, "Interobserver and intraobserver variability in the sonographic assessment of fatty liver" *American Journal of Roentgenology,* vol. 189 no. 6, pp. W320-W323, 2007.

[35] A. Pizurica {http://telin.ugent.be/~sanja/}

[36] M. Singh, S. Singh, S. Gupta, "An information fusion based method for liver classification using texture analysis of ultrasound images", *Information Fusion*, vol. 19, pp 91-96, 2014.

[37] Y.Y. Li, X.M. Wang, Y.X. Zhang and G.C Ou, "Ultrasonic elastography in clinical quantitative assessment of fatty liver" *World Journal of Gastroenterology*, vol. 16 no. 37, pp. 4733 – 4737, 2010.

[38] F.U. Minhas, D. Sabih and M. Hussain, "Automated Classification of Liver Disorders using Ultrasound Imageos", *Journal of Medical Systems*, vol. 36 no. 5, pp. 3163 – 3172, 2012.

[39] T. Szabo, "Diagnostic Ultrasound Imaging: Inside Out", Elsevier Academic Press, Boston 2004.

[40] H. Lutz, E. Buscarini, "WHO manual of diagnostic ultrasound volume 1" Second Edition, World Health Organization, Geneva, Switzerland, 2011.

[41] M. Ali, D. Magee and U. Dasgupta, "Signal Processing Overview of Ultrasound Systems for Medical Imaging", Texas Instrument, SPRAB12, 2008.

[42] C.R. Hill, J.C. Bamber and G.R. ter Haar, "Physical Principles of Medical Ultrasonics", 2nd edition, John Wiley & Sons Inc. USA, 2004

[43] R.L. Goldberg, S.W. Smith, J.G. Mottley, K.W. Ferrara, "Ultrasound: The Biomedical Engineering Handbook" 2nd edition, (Editors: Joseph D. Bronzino, Boca Raton), CRC Press USA, 2000.

[44] J.P. McGahan and B. B. Goldberg (Editors), "Diagnostic Ultrasound", 2nd edition, CRC Press USA, 2008.

[45] M.E. Anderson, M.S. McKeag, and G.E. Trahe, "The impact of sound speed errors on medical ultrasound imaging", *Journal of the Acoustical Society of America* , vol. 107 no. 6, pp. 3540-3548, 2000.

[46] Web MD {http://www.webmd.com/digestive-disorders/picture-of-the-

liver}

[47] P.W. Ralls, M.B. Johnson, G. Kanel, D.M. Dobalian, P.M. Colletti, W.D. Boswell, D.R. Radin and J.M. Halls, "FM sonography in diffuse liver disease: prospective assessment and blinded analysis", *Radiology,* vol. 161 no. 2, pp. 451-454, 1986.

[48] C.S. Marn, R.L. Bree, T.M. Silver, "Ultrasonography of liver: Technique and focal and diffuse disease", *Radiologic Clinics of North America*, vol. 29 no. 6, pp. 1151-1170, 1991.

[49] J.C. Scatarige, W.W. Scott, P.J. Donovan, S.S. Siegelman, R.C. Sanders, "Fatty infiltration of the liver: ultrasonographic and computed tomographic correlation", *Journal of Ultrasound in Medicine*, vol. 3 no. 1, pp. 9-14, 1984.

[50] A.E.A. Joseph, S.H. Saverymuttu, S. Al-Sam, M.G. Cook, J.D. Maxwell , "Comparison of liver histology with ultrasonography in assessing diffuse parenchymal liver disease", *Clinical Radiology*, vol. 43 no. 1, pp. 26-31, 1991.

[51] K.J. Taylor, C.A. Riely, L. Hammers, S. Flax, G. Weltin, G. Garcia-Tsao, H.O. Conn, R. Kuc and K.W. Barwick, "Quantitative ultrasound attenuation in normal liver and in patients with diffuse liver disease: importance of fat", *Radiology*, vol. 160, no. 1, pp. 65-71, 1986.

[52] A. Pizurica, W. Philips, I. Lemahieu and M. Acheroy, "A Versatile Wavelet Domain Noise Filtration Technique for Medical Imaging", *IEEE Transactions on Medical Imaging*, vol. 22 no. 3, pp. 323-331, 2003.

[53] T.A. Tuthill, R.B. Baggs and K.J. Parker, "Liver Glycogen and Water Storage: Effect on Ultrasound Attenuation", *Ultrasound in Medicine and Biology*, vol. 15 no. 7, pp. 621-627, 1989.

[54] Z. Wang, A.C. Bovik, H.R. Sheikh, E.P. Simoncelli, "Image Quality Assessment: From Error Visibility to Structural Similarity", *IEEE Transactions on Image Processing*, Vol. 13 no.4, pp. 600-612, 2004.

[55] L. Gagnon and A. Jouan, "Speckle Filtering of SAR images-A Comparative study between Complex-Wavelet-based and Standard Filters", *SPIE conference on WASIP-V*, San Diego, vol. 3169, pp. 80-91, 1997.

[56] C.E. Metz, "Basic principles of ROC analysis" in *Seminars in nuclear medicine*, vol. 8 no. 4, pp. 283-298, 1978.

[57] T. Fawcett, "An introduction to ROC analysis", *Pattern Recognition Letters*, vol. 27 no. 8, pp. 861–874, 2006.

[58] J.W. Goodman, "Some fundamental properties of speckle", *Journal of the*

Optical Society of America, vol. 66, no. 11, pp. 1145-1150, 1976.

[59] S. Gupta, L. Kaur, R.C. Chauhan and S.C. Saxena, "Wavelet-based statistical approach for speckle reduction in medical ultrasound images" *Medical and Biological Engineering and Computing*, vol. 42 no. 2, pp. 189-192, 2004.

[60] C.P. Loizou, C.S. Pattichis, C.I. Christodoulou, R.S.H. Istepanian, M. Pantziaris and A. Nicolaides, "Comparative evaluation of despeckle filtering in ultrasound imaging of the carotid artery", *IEEE Transactions on Ultrasonics, Ferroelectrics, and Frequency Control*, vol. 52 no. 10, pp. 1653-1669, 2005.

[61] J. S. Lee, "Digital image enhancement and noise filtering by using local statistics", *IEEE Transactions on Pattern Analysis Machine Intelligence*, vol. PAMI-2 no. 2, pp. 165-168, 1980.

[62] V.S. Frost , J.A. Stiles, K. S. Shanmugan, and J.C. Holtzman, "A model for radar images and its application for adaptive digital filtering of multiplicative noise", *IEEE Transactions Pattern Analysis and Machine Intelligence*, vol. 4 no. 2, pp. 157-165, 1982.

[63] J. Weickert, B.M. Romeny and M.A. Viergever, "Efficient and reliable schemes for nonlinear diffusion filtering", *IEEE Transactions Image Processing*, vol. 7 no. 3, pp. 398-410, 1998.

[64] M. J. Black, G. Sapiro, D. Marimont and D. Heeger, "Robust anisotropic diffusion", *IEEE Transactions on Image Processing*, vol. 7 no. 3, pp. 421-432, 1998.

[65] S. Zhong and V. Cherkassky, “Image denoising using wavelet thresholding and model selection”, in *Proceedings IEEE International Conference on Image Processing*, vol. 3, pp. 1-4, 2000.

[66] X. Zong, A. Laine, and E. Geiser, “Speckle reduction and contrast enhancement of echocardiograms via multiscale nonlinear processing”, *IEEE Transactions on Medical Imaging*, vol. 17 no. 4, pp. 532-540, 1998.

[67] X. Hao, S. Gao, and X. Gao , “A novel multiscale nonlinear thresholding method for ultrasonic speckle suppressing”, *IEEE Transactions on Medical Imaging*, vol. 18 no. 9, pp. 787–794, 1999.

[68] D. L. Donoho, “Denoising by soft thresholding”, *IEEE Transactions on Information Theory*, vol. 41 no. 3, pp. 613-627, 1995.

[69] A.M. Wink and J.B.T. Roerdink, “Denoising functional MR images: A comparison of wavelet denoising and Gaussian smoothing”, *IEEE Transactions on Medical Imaging*, vol. 23 no. 3, pp. 374-387, 2004.

[70] J.S. Jin, Y. Wang, and J. Hiller, "An adaptive non-linear diffusion

algorithm for filtering medical images," *IEEE Transactions on Information Technology in Biomedicine*, vol. 4 no. 4, pp. 298-305, 2000.

[71] P. Koveski { http://www.csse.uwa.edu.au/~pk/research/matlabfns}

[72] G. Stippel { http://gjenna.com/ }

[73] G. Stippel, W. Philips and I. Lemahieu, "A new denoising technique for ultrasound images using morphological properties of speckle combined with tissue classifying parameters", in *Proceedings of SPIE Medical Imaging Conference*, vol. 4687, pp. 324–333, 2002.

[74] A. Rosenfeld and J. Weszka, "Picture Recognition" in Digital Pattern Recognition, K. Fu (Ed.), Springer-Verlag, Berlin, 1980.

[75] J.C. Russ, The Image Processing Handbook, 3rd edition, CRC Press, USA, 1999.

[76] S. Livens, Image Analysis for Material Characterization, PhD thesis, University of Antwerp, Antwerp, Belgium, 1998.

[77] T. Randen, Filter and Filter Bank Design for Image Texture Recognition, PhD thesis, NTNU, Stavanger, Norway, 1997.

[78] M. Levine, "Vision in Man and Machine", McGraw-Hill, USA, 1985.

[79] M.H. Bharati, J.J. Liu and J.F. MacGregor, "Image texture analysis: methods and comparisons", *Chemometrics and intelligent laboratory systems,* vol. 72 no. 1, pp. 57-71, 2004.

[80] A. Materka, M. Strzelecki, "Texture Analysis Methods - A Review", Technical University of Lodz, Institute of Electronics, COST B11 report, Brussels, 1998.

[81] R.C. Gonzalez, R.E. Woods, "Digital Image Processing", 3rd edition, Prentice Hall, USA, 2007.

[82] F. Tomita and S. Tsuji," Computer Analysis of Visual Textures", Kluwer Academic Publishing, USA, 1990.

[83] R.M. Haralick, "Statistical and structural approaches to texture", in *Proceedings of the IEEE,* vol. 67 no. 5, pp. 786-804, 1979.

[84] G.R. Cross and A.K. Jain, "Markov Random Field Texture Models", *IEEE Transactions on Pattern Analysis and Machine Intelligence*, vol. PAMI-5 no. 1, pp. 25-39, 1983.

[85] A.P. Pentland, "Fractal-Based Description of Natural Scenes", *IEEE Transactions on Pattern Analysis and Machine Intelligence*, vol. PAMI-6 no. 6, pp. 661-674, 1984.

[86] R. Chellappa and S. Chatterjee, "Classification of Textures Using

Gaussian Markov Random Fields", *IEEE Transactions on Acoustic, Speech and Signal Processing*, vol. 33 no. 4, pp. 959-963, 1985.

[87] J.G. Daugman, "Uncertainty relation for resolution in space, spatial frequency and orientation optimized by two-dimensional visual cortical filters", *Journal of the Optical Society of America*, vol. 2 no. 7, pp. 1160-1169, 1985.

[88] S.G. Mallat, "A theory for multiresolution signal decomposition: the wavelet representation", *IEEE Transactions on Pattern Analysis and Machine Intelligence*, vol. 11 no. 7, pp. 674-693, 1989.

[89] Z.F. Lu, J.A. Zagzebski and F.T. Lee, "Ultrasound backscatter and attenuation in human liver with diffuse disease", *Ultrasound in Medicine & Biology*, vol. 25 no. 7, pp. 1047-1054, 1999.

[90] A. Bovik, M. Clark, W. Geisler, "Multichannel texture analysis using localized spatial filters", *IEEE Transactions on Pattern Analysis and Machine Intelligence*, vol.12 no. 1, pp. 55-73, 1990.

[91] H. Yoshida, D.D. Casalino, B. Keserci, A. Coskun, O. Ozturk, A. Savranlar, "Wavelet-packet-based texture analysis for differentiation between benign and malignant liver tumors in ultrasound images", *Physics in Medicine and Biology*, vol. 48 no. 22, pp. 3735-3753, 2003.

[92] A. Ahmadian, A. Mostafa, M.D. Abolhassani and N.R. Alam, "A method for texture classification of ultrasonic liver images based on Gabor wavelet", *IEEE Proceedings 7th International Conference on Signal Processing*, vol. 2, pp. 971-974, 2004.

[93] J.M. Thijssen, F.M.J. Valckx, "Characterization of Echo-graphic image texture by Co-occurrence matrix parameters", *Ultrasound in Medicine & Biology*, vol. 23 no. 4, pp. 559-571, 1997.

[94] X. Yang, S. Tridandapani, J.J. Beitler, D.S. Yu, E.J. Yoshida, W. J. Curran and T. Liu, "Ultrasound GLCM texture analysis of radiation-induced parotid-gland injury in head-and-neck cancer radiotherapy: An in vivo study of late toxicity", *Medical Physics*, vol. 39 no. 9, pp. 5732-39, 2012.

[95] E.M. Ferdeghini, B. Pinamonti,E. Picano , F. Lattanzi, R. Bussani, G. Slavich, F. Camerini, L. Landini and A. L'Abbate, "Quantitative texture analysis in echocardiography: application to the diagnosis of myocarditis", *Journal of Clinical Ultrasound*, vol. 10 no. 5, pp. 263-270, 1991.

[96] H. Sujana, S. Swarnamani and S. Suresh, “Application of artificial neural networks for the classification of liver lesions by image texture parameters”, *Ultrasound in Medicine & Biology*, vol. 22 no. 9, pp. 1177- 1181, 1996.

[97] E. Kyriacou, S. Pavlopoulos, G. Konnis, D. Koutsouris, P. Zounipoulis and I. Theotokas, "Computer assisted characterization of diffused liver disease using image texture analysis techniques on B-scan images”, *IEEE Nuclear Science Symposium*, pp. 1479-1483, vol. 2, 1997.

[98] J. Damilakis, K. Perisinakis, E. Vagios, D. Tsinikas and N. Gourtsoyiannis, "Effect of region of interest location on ultrasound measurements of the calcaneus", *Calcified Tissue International*, vol. 63, no. 4, pp. 300-305,1998.

[99] M. Tuceryan and A.K. Jain, "Texture Analysis" from The Handbook of Pattern Recognition and Computer Vision, 2nd edition, (Editors C.H. Chen, L.F. Pau and P.S.P Wang), World Scientific Publishing Co., pp 207-248, USA, 1998.

[100] D. Miittal, V. Kumar, S.C. Saxena, N. Khandelwal and N. Kalra, “Neural network based focal liver lesion diagnosis using ultrasound images”, *Computerized Medical Imaging and Graphics*, vol. 35 no. 4, pp. 315-323, 2011.

[101] J. Virmani, V. Kumar, N. Kalra and N. Khandelwal "SVM-Based Characterization of Liver Ultrasound Images Using Wavelet Packet Texture Descriptors", *Journal of Digital Imaging*, vol. 26 no. 3, pp. 530-543, 2013.

[102] H. Li, M.L.Giger, Z. Huo, O.L. Olopade, L. Lan, B.L. Weber and I. Bonta, “Computerized analysis of mammographic patterns for assessing breast cancer risk: Effect of ROI size and location”, *Medical Physics,* vol. 31 no. 3, pp. 549-555, 2004.

[103] J.H. Jeon, J. Y. Choi, S. Lee and Y. M. Ro, "Multiple ROI selection based focal liver lesion classification in ultrasound images", *Expert Systems with Applications*, vol. 40 no. 2, pp. 450-457, 2013.

[104] S. Poonguzhali, D. Balasubramanian, and G. Ravindran, "Optimal feature selection and automatic classification of abnormal masses in ultrasound liver images", in *Proceedings of the International Conference on Signal Processing, Communications and Networking*, pp. 503-506, 2007.

[105] M. Mancini, A. Prinster, G. Annuzzi, R. Liuzzi, R. Giacco, C. Medagli,M.

Cremone, G. Clemente, S. Maurea, G. Riccardi, A.A. Rivellese and M. Salvatore, "Sonographic hepatic-renal ratio as indicator of hepatic steatosis: comparison with (1)H magnetic resonance spectroscopy", *Metabolism: clinical and experimental*, vol. 58 no. 12, pp. 1724-1730, 2009.

[106] S.A. Azaid, M.W. Fakhr and A.F.A. Mohamed, "Automatic diagnosis of liver diseases form ultrasound images", in *Proceedings of the International Conference on Computer Engineering and Systems*, pp. 313-319, 2006.

[107] R.A. Mountford, and P.N.T. Wells, “Ultrasonic liver scanning: A-scan in Normal and Cirrhosis”, *Physics in Medicine and Biology*, vol. 17 no. 2, pp. 261-269, 1972.

[108] P.N.T. Wells, “Ultrasound imaging”, *Physics in Medicine and Biology*, vol. 51 no. 13, pp. R83–R98, 2006.

[109] Y. Yajima, K. Ohta, T. Narui, R. Abe, H. Suzuki and M. Ohtsuki, “Ultrasonographical diagnosis of fatty liver: Significance of Liver-Kidney contrast”, *Tohoku Journal of Experimental Medicine*, vol. 139 no. 1, pp. 43-50, 1983.

[110] D. Nicholas, D.K. Nassiri, P. Garbutt, C.R. Hill "Tissue characterization from ultrasound B-scan data", *Ultrasound in Medicine & Biology, Elsevier*, vol. 12 no. 2, pp. 135-143, 1986.

[111] M.S.K. Gebbinck, J.T.M. Verhoeven, J.M. Thijssen and T.E. Schouten, “Application of Nueral Networks for the Classification of Diffuse Liver Disease by Quantitative Echography”, *Ultrasonic Imaging*, vol. 15, pp. 205-217, 1993.

[112] A. Mojsilovic, M. Popovic, S. Markovic “Characterization of visually similar diffuse diseases from B-scan liver images using nonseparable wavelet transform", *IEEE Transactions on Medical Imaging*, vol. 17 no. 4, pp. 541-549, 1998.

[113] S. Mukherjee, A. Chakravorty, K. Ghosh, M. Roy, A. Adhikari, and S. Mazumdar, “Corroborating the Subjective Classification of Ultrasound Images of Normal and Fatty Human Livers by the Radiologist through Texture Analysis and SOM”, *in Proceedings of International conference on Advanced Computing and Communications*, pp. 197 – 202, 2007.

[114] W.L. Lee and K.S. Hsieh, “Computer Assisted Characterization for Ultrasonic Liver Tissue by Fusion of Classifiers”, *in Proceedings of ICICIC-07*, pp. 100-103, 2007.

[115] S. Theodoridis and K. Koutroumbas, Pattern Recognition, 4th edition, Academic Press, USA, 2008.

[116] B.V. Dasarathy, “Information fusion in the realm of medical applications – A bibliographic glimpse at its growing appeal”, *Information Fusion*, vol. 13 no.1, pp. 1-9, 2012.

[117] A.G. Lalkhen, A. McCluskey, “Clinical tests: sensitivity and specificity”, *Continuing Education Anesthesia, Critical Care & Pain,* vol. 8 no. 6, pp. 221-223, 2008.

[118] O.W. Hamer, D.A. Aguirre, G. Casola, J.E. Lavine, M. Woenckhaus, C.B. Sirlin, “Fatty liver: imaging patterns and pitfalls”, *Radiographics*, vol. 26 no. 6, pp.1637-1653, 2006.

[119] N. Mennesson, J. Dumortier, V. Hervieu, L. Milot, O. Guillaud, J.Y. Scoazec and F. Pilleul, “Liver Steatosis Quantification Using Magnetic Resonance Imaging: A Prospective Comparative Study With Liver Biopsy”, *Journal of Computer Assisted Tomography*, vol. 33 no.5, pp. 672-677, 2009.

[120] D.A. Sass, P. Chang and K.B. Chopra, “Nonalcoholic Fatty Liver Disease: A Clinical Review”, *Digestive Diseases and Sciences*, vol. 50 no. 1, pp. 171-180, 2005.

[121] M.F. Xia, H.M. Yan, W.Y. He, X. Li, C. L. Li, X.Z. Yao, R.K. Li, M.S. Zeng and X. Gao, “Standardized Ultrasound Hepatic/Renal Ratio and Hepatic attenuation Rate to Quantify Liver fat Content: an Improvement Method”, *Obesity*, vol. 20 no. 2, pp. 444-452, 2012.

[122] B.S. Garra, M.F. Insana, T. H. Shawker and M.A. Russell, "Quantitative estimation of liver attenuation and echogenicity: normal state versus diffuse liver disease." *Radiology,* vol. 162 no. 1, pp. 61-67, 1987.

[123] D.F.Y. Chan, A. M. Li, W.C. Chu, M.H.M. Chan, E.M.C. Wong, E.K.H. Liu, I.H.S. Chan, J. Yin, C.W.K. Lam, T.F. Fok and E.A.S. Nelson, “Hepatic steatosis in obese Chinese children”, *International Journal of Obesity*, vol. 28, pp. 1257–1263, 2004.

[124] C.C. Mottin, M. Moretto, A.V. Padoin, A.M. Swarowsky, M.G. Toneto, and G. Repetto, “The role of ultrasound in the diagnosis of hepatic steatosis in morbidly obese patients”, *Obesity Surgery,* vol. 14 no. 5, pp. 635-637, 2004.

[125] R.C. Chivers and C.R. Hill , “Ultrasonic attenuation in Human Tissue”, *Ultrasound in Medicine & Biology,* vol. 2 no.1, pp. 25-29, 1975.

[126] J.M. Thijssen, A. Starke, G. Weijers, A. Haudum, K. Herzog, P. Wohlsein, J. Rehage, and C.L. De Korte "Computer-aided B-mode ultrasound diagnosis of hepatic steatosis: a feasibility study", *IEEE Transactions on Ultrasonics, Ferroelectrics and Frequency Control* vol. 55 no. 6, pp. 1343-1354, 2008.

[127] J.R. Lewis and S.R. Mohanty, "Nonalcoholic fatty liver disease: a review and update", *Digestive Diseases and Sciences*, vol. 55 no. 3, pp. 560-578, 2010.

[128] M. Fukushima, K. Ogawa, T. Kubota and N. Hisa, "Quantitative tissue characterization of diffuse liver diseases from ultrasound images by neural network", *IEEE Symposium*, 1997.

[129] D. Gaitini, Y. Baruch, E. Ghersin, E. Veitsman, H. Kerner, B. Shalem, G. Yaniv, C. Sarfaty and Haim Azhari, "Feasibility study of ultrasonic fatty liver biopsy: texture vs. attenuation and backscatter" *Ultrasound in Medicine & Biology*, vol. 30 no. 10, pp. 1321-1327, 2004.

[130] J.R. Quan, X.Q. Xie, J.L. Lin, Y. Chen, W.W. Ling, Q. Lu, Y. T. Fan and Y. Luo, "Ultrasound tissue characterization of hepatic fat in rats using radiofrequency signal analysis", *Journal of Sichuan University,* vol. 43 no. 1, pp. 54-60, 2012.

[131] K.D. Donohue, I. Huang, T. Burks, F. Forsberg and C.W. Piccoli, "Tissue Classification with Generalized Spectrum Parameters", *Ultrasound in Medicine & Biology*, vol. 27 no. 11, pp. 1505-1514, 2001.

[132] K. Ogawa, M. Fukushima, K. Kubota and N. Hisa, "Computer-aided diagnostic system for diffuse liver diseases with ultrasonography by neural networks", *IEEE Transactions on Nuclear Science*, vol. 45 no. 6, pp. 3069-3074, 1998.

[133] C.C. Wu, W.L. Lee, Y.C, Chen, C.H. Lai, K.S. Hsieh, "Ultrasonic liver tissue characterization by feature fusion", *Expert Systems with Applications*, vol. 39, pp. 9389-9397, 2012.

[134] R.B. Soder, M. Baldisserotto, V.D. Silva, "Computer-Assisted Ultrasound Analysis of Liver Echogenicity in Obese and Normal-Weight Children", *American Journal of Radiology*, vol. 192, pp. W201 - 205, 2009.

[135] W.C. Yeh, Y.M. Jeng, C.H. Li, P.H. Lee and Li P.C., "Liver steatosis classification using high-frequency ultrasound", *Ultrasound in Medicine & Biology*, vol.31 no.5, pp. 599-605, 2005.

[136] G.T. Cao, P.F. Shi and B. Hu, "Liver fibrosis identification based on

ultrasound images captured under varied imaging protocols*", Journal of Zhejiang University SCIENCE*, vol. 6B no. 11, pp. 1107-1114, 2005.

[137] B.C. Yung, S. Sostre, "Kidney-to-liver ratio: A simple scintigraphic parameter for routine individual renal function assessment in children", *Clinical Nuclear Medicine*, vol.19 no. 3, pp. 228-32, 1994.

[138] M.A. Samad, H. Hayashibara, Y. Utsunomiya and K. Shiraki, "A Study on Echogenic Changes of the Kidney-Spleen and Liver-Spleen Contrasts with Age in Infants and Children", *Yonago Actamedica,* vol. 40, pp. 31-42, 1997.

[139] C. Nicolau, R. Vilana, V. Catala, L. Bianchi, R. Gilabert, A. Garcia, C. Bru, "Importance of evaluating all vascular phases on contrast-enhanced sonography in the differentiation of benign from malignant focal liver lesions", *American Journal of Roentgenology*, vol. 186, pp. 158-167, 2006.

[140] G. Layer, I. Zuna, A. Lorenz, H. Zerban,"Computerized ultrasound B-scan texture analysis of experimental diffuse parenchymal liver disease: Correlation with histopathology and tissue composition" *Journal of Clinical Ultrasound*, vol.19 no. 4, pp. 193-201, 1991.

[141] J.H. Wang, C.H. Hung, F.Y. Kuo, H.L. Eng, C.H. Chen, C.M. Lee, S.N. Lu and T.H. Hu, "Ultrasonographic Quantification of Hepatic–Renal Echogenicity Difference in Hepatic Steatosis Diagnosis", *Digestive Diseases and Sciences*, vol. 58 no. 10, pp. 2993-3000, 2013.

[142] M. Singh, S. Singh and S. Gupta, A new quantitative metric for liver classification from ultrasound images, *International Journal of Computer and Electrical Engineering*, vol. 4 no. 4, pp. 605 – 607, 2012.

List of Research Publications

1. M. Singh, S. Singh and S. Gupta, "An information fusion based method for liver classification using texture analysis of ultrasound images", *Information Fusion*, vol. 19, pp 91-96, 2014.
2. M. Singh, S. Singh and S. Gupta, "Comparative Analysis of Spatial filters for Speckle Reduction in Ultrasound Images', *World Congress on Computer Science and Information Engineering CSIE-09,* vol. 6, pp. 228-232, 2009.
3. M. Singh, S. Singh and S. Gupta, "A new quantitative metric for liver classification from ultrasound images", *International Journal of Computer and Electrical Engineering*, vol. 4 no. 4, pp. 605 – 607, 2012.
4. M. Singh, S. Singh and S. Gupta, "An Adaptive speckle suppression filter based on local statistics and edge-map for ultrasound images", *Advanced Science Letters*, vol. 19 no. 8, pp. 2375-2379, 2013.
5. M. Singh, S. Singh and S. Gupta, "Investigations on ROI selection from ultrasound images for liver classification". (Accepted in CCECE 2014 IEEE conference, Toronto, CANADA).
6. M. Singh, S. Singh and S. Gupta, "Role of speckle suppression filter on texture based liver classification". (**Communicated**).
7. M. Singh, S. Singh and S. Gupta, "SVM based fatty liver grading using hepato-renal ratio of texture features". (**Communicated**).